MECHANICAL AND TRIBOLOGICAL CHARACTERIZATION OF CLADDING ON LOW CARBON STEEL FABRICATED BY GMAW USING COLD METAL TRANSFER (CMT)

Thesis Submitted

In Partial Fulfilment of the Requirements for the

Degree of

DOCTOR OF PHILOSOPHY

in

Mechanical Engineering

by

Varsha Mishra

(2K19/Ph.D./ME/05)

Under the supervision of

Dr. N. Yuvaraj
Department of Mechanical Engineering
DTU

Prof. Vipin
Department of Mechanical Engineering
DTU

Department of Mechanical Engineering
DELHI TECHNOLOGICAL UNIVERSITY
(Formerly Delhi College of Engineering)
Main Bawana Road, Shahabad Daulatpur, Delhi - 110042, India
2024

CANDIDATE'S DECLARATION

I, Varsha Mishra, do hereby certify that the work which is being presented in this thesis, entitled "**Mechanical and tribological characterization of cladding on low carbon steel fabricated by GMAW using Cold Metal Transfer (CMT)**" in the partial fulfilment of the requirement for the award of degree of Doctor of Philosophy, submitted in the Department of Mechanical Engineering, Delhi Technological University, is an authentic record of my own work carried out during a period from August 2019 to June 2024, under the supervision of **DR. N. YUVARAJ** and **PROF. VIPIN**, Department of Mechanical Engineering, Delhi Technological University, Delhi. The matter presented in this thesis has not been submitted by me for the award of any other degree of this or any other University/Institute.

(VARSHA MISHRA)
Roll No: 2K19/Ph.D./ME/05

This is to certify that the student has incorporated all the corrections suggested by the examiners in the thesis and the statement made by the candidate is correct to the best of our knowledge.

Signature of Supervisor (s) **Signature of External Examiner**

CERTIFICATE

Certified that **Mrs. Varsha Mishra (2k19/Ph.D./ME/05)** has carried out their research work presented in this thesis entitled "**Mechanical and tribological characterization of cladding on low carbon steel fabricated by GMAW using Cold Metal Transfer (CMT)**" for the award of **Doctor of Philosophy** in Mechanical Engineering from Delhi Technological University, Delhi-110042, under our supervision. The thesis embodies results of original work, and the contents of the thesis do not form the basis for the award of any other degree to the candidate or to anybody else from this or any other University/Institutions.

DR. N. YUVARAJ
Department of Mechanical Engineering
Delhi Technological University, Delhi.

PROF. VIPIN
Department of Mechanical Engineering
Delhi Technological University, Delhi.

Date:

ACKNOWLEDGEMENT

I am greatly indebted to my supervisor, Dr. N. Yuvaraj and Prof. Vipin, Department of Mechanical Engineering, Delhi Technological University, Delhi, for their invaluable guidance, constant inspiration, numerous suggestions, and continued support throughout this research work. I am profoundly grateful to him with reverence for helping me with the necessary information and equipment & materials as well.

With great humbleness, I sincerely thank Prof. S.K. Garg, and Prof. B.B Arora Professor, and Head for his insightful comments and constant encouragement. SRC Committee members and faculty members of the Department of Mechanical Engineering, Delhi Technological University, for their suggestions and support throughout the research work.

I would also like to thank with much appreciation the people whose help and support were a great asset; the technical staff at DTU, namely, Mr. Net Ram, Mr. Lalan Kumar Sinha, Mr. Girish Anand, and Mr. Sanjay Gupta, who provided great help for conducting the experiments and material characterization; Mr. Sandeep for their help in conducting the XRD studies, Mr. Tek Chand for his help in revealing the microstructures, Mr. Rajiv Bohra for his help and assistance in doing the tribology tests.

Finally, I dedicate my work to my parents and my daughter. My sincere gratitude to my father Dr. Ashok Chaubey, my mother Mrs. Anita Chaubey, my mother-in-law Mrs. Shubhawati Mishra, my husband Mr. Vidhu Shekhar Mishra, my brother Mr. Vivek Chaubey and my loving daughter Shanvi Mishra, for their blessings and sacrifices which greatly helped me in carrying out this research work.

VARSHA MISHRA

ABSTRACT

Weld cladding has emerged as an innovative technique for enhancing the surface properties of carbon steel, with widespread applications across multiple industries, including chemical processing, marine, mining, agriculture, and power generation. The low carbon steel has become an in-demand material in different industrial applications due to its versatility and cost-effectiveness. Despite its unparalleled advantages, it cannot be utilized in wear-resistant applications without surface altercation, which can be achieved by cladding stainless steel over low-carbon steel. Low-carbon steels can be clad with stainless steel to enhance their mechanical wear properties.

Studies were carried out to investigate the impact of process parameters on weld bead geometry and dilution% during cold metal transfer (CMT) cladding of super duplex stainless steel 2507 over low carbon steel. Response Surface Methodology (RSM) with a Central Composite Design matrix was used to optimize the process parameters (welding current, welding speed, and nozzle to work-piece distance (NTD)). The adequacy of the model was checked using an ANOVA analysis. The ideal input parameters were 200 A of welding current, 4.64 mm/s of welding speed, and 14 mm of NTD. The welding speed is the most dominant parameter, followed by the welding current and NTD. The cladding samples were prepared using the optimal parameters. The CMT-clad layer's microstructure, microhardness, and wear properties were also evaluated. The results indicate a dense crack-free and non-porous clad surface was obtained under optimal conditions.

The tribological performance of the Austenite stainless steel clad over low carbon steel plate samples prepared at different CMT welding speeds (3, 4, 5, and 6 mm/sec) was studied. A ball-on-disc reciprocating tribometer was used to examine the wear characteristics of the cladding surface by varying the normal loads (30N, 40N & 50N) and frequencies (5Hz, 10Hz & 15Hz). The wear resistance of the cladding surface is enhanced by 30-40% compared to a base material. Results show that the wear rate varies with applied load and frequency due to the metastability of austenitic stainless steel during plastic deformation; the austenite changes into martensite. The cladding and worn-out surfaces were examined through optical and field emission scanning electron microscopy (FESEM) to study the wear mechanisms.

The comparison of the Cold Metal Transfer (CMT) welding and pulse MIG welding processes to study the weld-clad bead of 308L stainless steel over low-carbon steel was also carried out. To investigate the mechanical and wear properties of CMT weld-clad samples, welding speed (3, 4, 5, and 6 mm/sec) was used as the input process parameter, while maintaining constant current (175 A), nozzle-to-workpiece distance, and shielding gas flow rate (15 l/min). Microstructural examination of weld beads was conducted using optical microscopy and FESEM. Results showed that increasing welding speed enhanced microhardness and wear resistance of the clad surface. Notably, the CMT cladding process demonstrated superior mechanical and wear properties, reduced residual stresses, and lower heat input compared to pulse MIG welding, attributed to minimal dilution.

CONTENTS

LIST OF FIGURES

LIST OF TABLES

LIST OF SYMBOLS AND ABBREVIATIONS

ANOVA	Analysis of variance
ASTM	American Society for Testing Materials
BCP	Background Current Phase
BHN	Brinell Hardness Number
BM	Base Metal
CAV	Constant Arc Voltage
CMT	Cold Metal Transfer
CO	Carbon Monoxide
CO_2	Carbon Di-Oxide
CSC	Conventional Short Circuit
Cu	Copper
DCEN	Direct Current Electrode Negative
DCEP	Direct Current Electrode Positive
DCRP	Direct Current Reverse Polarity
DE	Design Expert
DOE	Design of Experiments
DPC	Digital Process Control
EDM	Electrical Discharge Machine
EDS	Energy Dispersive Spectrometer
EDX	Energy Dispersive X-ray
FCAW	Flux Cored Arc Welding
FESEM	Field Emission Scanning Electron Microscope
FL	Fusion Line
FZ	Fusion Zone
GMAW	Gas Metal Arc Welding
GTAW	Gas Tungsten Arc Welding
HAZ	Heat Affected Zone

HR-XRD	High-Resolution X-ray Diffraction
IMC	Inter-Metallic Compounds
IML	Inter-Metallic Layer
Mg	Magnesium
MIG	Metal Inert Gas
NDT	Non-Destructive Technique
NTD	Nozzle To Workpiece Distance
OCV	Open Circuit Voltage
PCP	Peak Current Phase
PDC	Pulse Dynamic Correction
RSM	Response Surface Methodology
SAW	Submerged Arc Welding
SCP	Short Circuiting Phase
SEM	Scanning Electron Microscope
SMAW	Shielded Metal Arc Welding
SS	Stainless Steel
THI	Thermal Heat Input
TIG	Tungsten Inert Gas
U-CMT	Ultrasonic Assisted Cold Metal Transfer
UTM	Universal Testing Machine
UTS	Ultimate Tensile Strength
VHN	Vickers Hardness Number
VP-CMT	Variable Polarity Cold Metal Transfer
WFS	Wire Feed Speed
WM	Weld Zone / Weld Metal
XRD	X-Ray Diffraction

CHAPTER 1

INTRODUCTION

The interaction between the surface of a solid material and its nearby environment can degrade the surface over time. This degradation of the surface of the material can be caused by creep, fatigue, wear, and corrosion over time due to its nearby environment. Surface engineering is a multidisciplinary activity supposed to tailor the properties of the engineering components surface to advance their capabilities. Surface engineering treated the surface and near-surface area to allow the surface to perform desired functions, which include sacrificial protection of the surface from corrosion, improved wear and corrosion resistance, improved mechanical properties, and reduced friction. [Davis, J.R. (2001)] Surface engineering techniques can be used to improve the electrical, chemical, physical, mechanical, magnetic, corrosion-resistant, and wear-resistant properties of the material or substrate surfaces. Surface engineering can be used to alter the properties of the material's surface in order to reduce its degradation over time. It is practiced by making the surface resistant to the surrounding environment in which it will be utilized. It gives savvy material to a strong plan. Surface engineering is mostly an effective solution for controlling wear on the surfaces of materials. Various methods of surface engineering include cyaniding, cladding, carburizing, and nitriding [Bloyce (1998)]. The development of surface engineering technologies and new alloys has complemented each other in serving the needs of a variety of engineering applications. Such a simultaneous development allows the designers to provide equal

priority for surface quality, manufacturability, bulk strength, and its properties, such that the overall development cycles can be significantly shortened.

Today's surface engineering is a convenient and economic alternative to the use of cladded plate or solid alloy for improving the life of engineering components operating under corrosion and wear. Today's fast-growing industries very much needed surface engineering for cost rationalization and other economic factors, productivity improvements, technical problems, and a drive for having neo-materials with better attributes and qualities. The weak-strength material cladding for improving material attributes is important for every industry so as to ensure the ensure the successful functioning of the material. The materials are cladded to improve their corrosion resistance, wear resistance, and many other utilities for the thermal environment, etc. Material cladding is being utilized for making utensils, tools, and boilers.

1.1 CLADDING

Cladding is a surface altercation technique to add a layer of suitable material to the underlying layer of desired properties by quasi-melting the substratum with the added powder(s) completely melting on the subsurface layer. The cladding process is used for minimum dilution of the base material with good metallurgical bonding. [Gupta & Sharma, 2014]. In the process of cladding, we deposit a thick layer of clad material on a base metal with a low alloy steel or carbon. It is economically wiser to use cladding, as under it, cheaper and more machinable parent material is getting coated with expensive, corrosion-resistant, and wear-resistant metals for achieving desired results in specific areas of

production. Cladding has been one of the most widely used approaches to alleviate corrosion, for example, the deposition of a corrosion-resistive material layer on a base metal or substrate. Cost savings is one of the main pros of this technique, achieved by surfacing a relatively cheaper metal, i.e., carbon steel, with an expensive but corrosive-resistant and wear-resistant layer of stainless steel. It is a surface-adding technique being used in different industries: automotive, power, missile, electronic, biomedical, aerospace, petroleum, textile, petrochemical, chemical, steel, cement, machine tools, etc. [Kumar & Singh, 2012].

1.1.1 Weld cladding

Weld cladding is a surfacing procedure to create a thick layer of corrosion-resistant material on low-carbon steel to diminish corrosion at the surface of the segment. Different conventional weld cladding processes have been utilized for cladding before, and recently created ones are being utilized these days. The Gas Metal Arc (GMAW) cladding process is widely preferred among various cladding procedures such as shielded metal arc weld (SAW) cladding, plasma arc weld (PAW) cladding, laser arc cladding, gas tungsten arc weld (GTAW) cladding, and flux core arc weld (FCAW) cladding due to its ease of use, ability to be used in all positions, superior quality, high deposition rate and efficiency, high reliability, suitability for both non-ferrous and ferrous materials, and ease of automation. The gas metal arc welding process, due to its distinct advantages, continues to be utilized and has been the subject of research for cladding purposes.

1.1.2 Weld Cladding Parameters

To carry out the weld cladding process, input variables have to be identified and selected adequately. The important input parameters that significantly affect the clad bead geometry are: cladding speed (S), voltage (V), cladding current (I), nozzle-to-workpiece distance, wire feed rate, and shielding gas (SG).

Current (I): has a very significant effect on dilution; as the current dilution increases, at a lower level than the current minimum dilution conditions were found [Kumar & Singh, (2012)].

Voltage (V): contributes most to the bead width and dilution percentage. An increasing value of voltage increases bead width and dilution percentage.

Shielding gases: Protecting gases are important for this type of cladding to shield the area from barometrical gases, for example, nitrogen and oxygen, which can cause weld metal embrittlement on the off chance that they interact with the circular segment, or the welding metal. Unadulterated idle gases, like helium and argon, are utilized for nonferrous welding, but with steel, they don't give sufficient weld entrance with (argon) or cause a sporadic circular segment and support splash (with helium). Unadulterated carbon dioxide, then again, takes into account profound entrance welds, but supports oxide development, which antagonistically influences the weld mechanical properties.

Feed rate of wire: Bead height and penetration depth are primarily determined by the wire feed rate, which is the speed at which the wire exits the wire spool and pushes through the nozzle.

Stick-out distance: stick-out distance is the distance between the workpiece and nozzle. It is also having a significant effect on bead geometry and dilution percentage. Dilution decreases with a decrease in stick-out distance and increases with an increase in it.

1.1.3 Dilution

The dilution in welding terms is characterized as the weight of the base metal divided by aggregate weight of the weld metal, i.e. we have a dilution of 0.40, and the part of the weld metal that came from the consumable electrode is 0.60 as appeared in Fig. 1.1

Calculation of Dilution is given in equation 1.1,

$$\text{Dilution} = Ap / (Ap+Ar) \quad (1.1)$$

Where, Ap = Penetration area and Ar = Reinforcement area

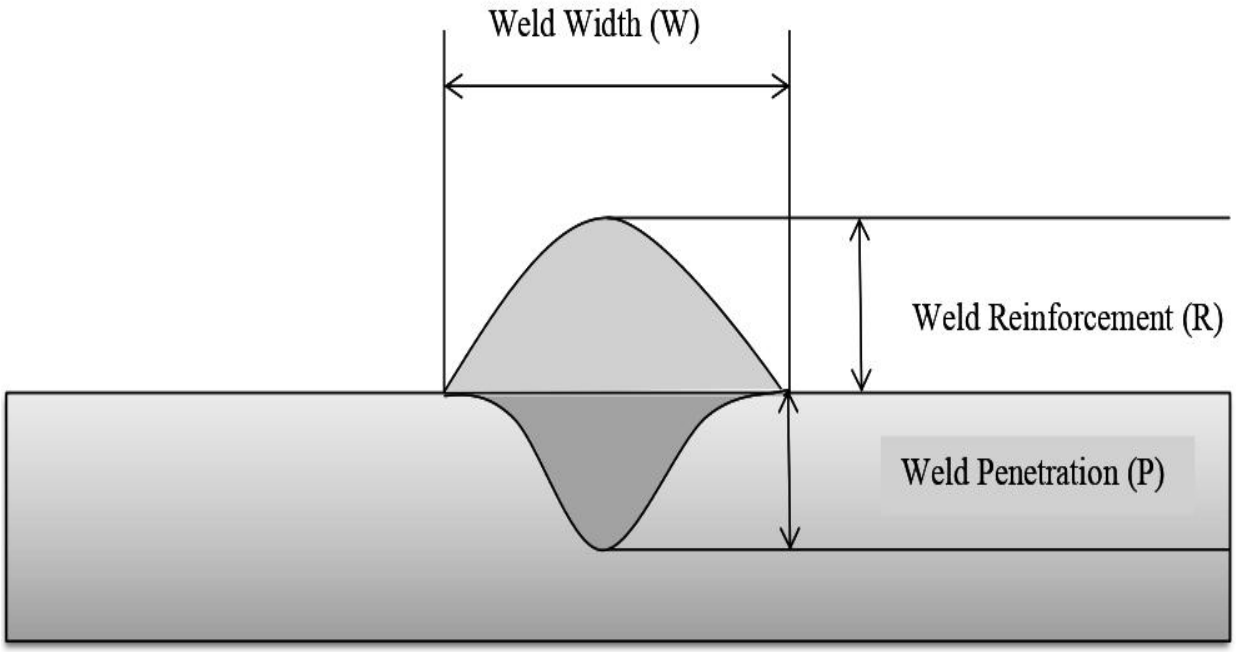

Fig. 1.1 Bead geometry

Dilution increases with decreasing NTD and increasing current and voltage. Minimum dilution occurs at lower levels of current and voltage and high NTD [Kumar & Singh, (2012)].

1.2 COLD METAL TRANSFER PROCESS

The CMT process is an advanced version of the metal arc gas/metal inert gas (MAG/MIG) welding process with an explicit low heat input and process control for the parent metal. CMT is now no longer the best absolutely new technique, but additionally permits utility, which might be yet absolutely unexplored. The evolution of GMAW is important for welding and automation [Fronius, 2005]. The important advantage of this neo-system is the possibility of concurrent dip transfer, pulse arc welding, and a lower heat input than conventional MAG/MIG welding. A unique wire speed controlling system is incorporated into waveform and assists in regulating the arc length and molten metal detachment. In fronius, it provides an explanation that with the development of arc plasma filler, metal moves towards the weld pool until it touches the weld pool and a short circuit occurs. Afterwards, the electrode is retracted, enhancing the droplet detachment, and the current becomes lower. Welding aluminum alloy with steel is the latest application of this new technique, and a spectrum of applications is possible with this new technique [Pickin et al., 2011].

To analyse the energy distribution during different stages of the droplet transfer process, it is essential to examine the voltage and current waveforms. These waveforms provide information about the distinct phases of the process, measured in microseconds [Z.

Sun et al., (2015)] The CMT cycle of the voltage-current waveform is shown in Fig. 1.2. The cycle indicates the following three distinguished phases:

The 'Current at peak Phase' (PCP): known as a "constant arc voltage", which is a short high current pulse that quickly melts the electrode wire and sparks the welding arc to generate a droplet.

The 'Background Current Phase' (BCP): A lower current phase has been correlated with it. When the droplet forms on the tip of the wire during the current at peak phase, to stop the globular transfer, the current is lowered to non-zero, which aids in preventing the formation of spatter. This stage continues until there is a short-circuit.

The 'Short-Circuiting Phase' (SCP): A zero-arc voltage is associated with this phase. In this case, upon contact between the wire and the weld pool, the arc voltage instantly decreases to zero. "Digital Process Control" (DPC) provides the retractor mechanism for the wire feeder concurrently. This mechanism helps with liquid bridge fracture and material transfer into the weld pool by providing a back-drawing force to the wire. The sequence then repeats itself once more once the arc is re-ignited [Feng et al., (2009)].

The welding cycle of the CMT demonstration is illustrated in Fig. 1.3.

a) Arc initiation: The filler metal enters the weld pool during the arcing phase.
b) Short circuiting current: As the filler metal wire dips into the pool of weld, the arc is extinguished. Lower heat input is the result of decreased welding current.
c) Retraction of wire: The wire's rearward movement facilitates droplet separation during the short circuit. The short circuit's current is kept to a minimum.
d) Process continues: The process repeats itself as the wire moves in the opposite direction.

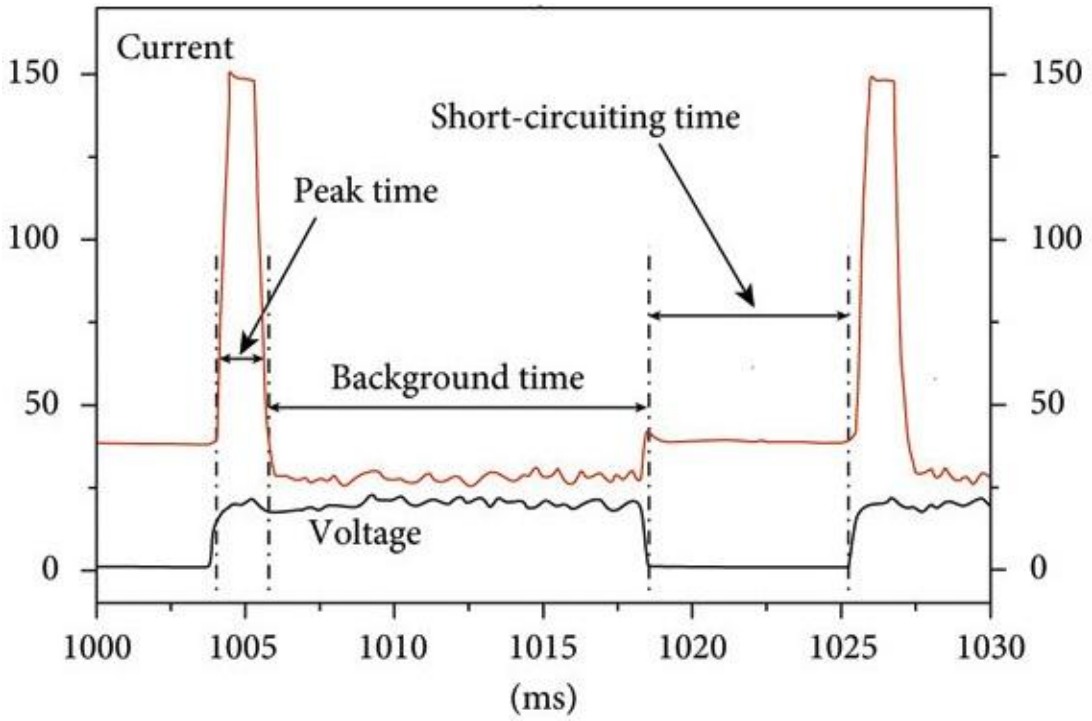

Fig. 1. 2 Voltage and current waveform in CMT

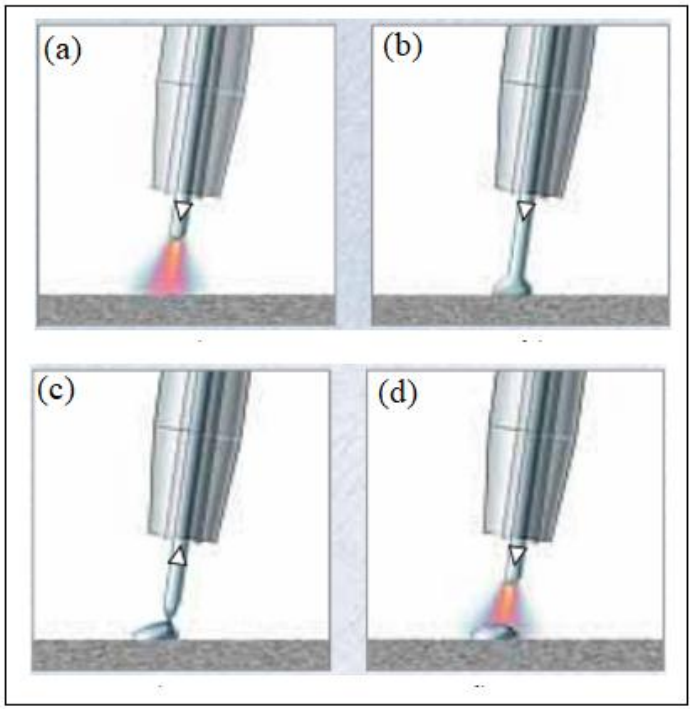

Fig 1.3 CMT Welding Process Demonstration

1.3 STAINLESS STEEL CLADDING

Clad carbon steel is utilized in a range of industries, including chemical processing, oil refining, and offshore oil production. It is also utilized in power generation systems that experience high temperatures and stress corrosion. Stainless steel cladding enhances the longevity of a carbon steel surface by applying a thin coating of stainless steel. Additional benefits of stainless-steel cladding include:

- Enhanced resistance to corrosion and rust, resulting in a longer operational life
- Increased mechanical strength and thermal resistance, reducing the risk of failure
- Exceptional weldability and a polished finish
- More cost-effective compared to other, more exotic Cu-Ni alloys
- Well-suited for sanitary applications.

There are numerous options available when it comes to stainless-steel kinds, allowing for the possibility of cladding in a wide range of distinct applications. It offers increased strength and exceptional resistance to corrosion, because of its combination of ferrite and austenite. They are valued for their exceptional corrosion resistance properties and typically include 10–20% chromium as the primary alloying element. Steel is around 200 times more corrosion resistant than mild steel since it contains more than 11% chromium.

Austenitic: Austenitic steels typically include less than 0.8% carbon,18% chromium and 8% nickel. They are also non-magnetic and cannot be hardened by heat treatment. The majority of the stainless-steel market worldwide is made up of austenitic steels, which are utilized in chemical industries, cooking utensils, and equipment used in food processing.

Ferritic: Ferritic steels also include trace amounts of molybdenum, aluminum, or titanium in addition to 12–17% chromium, less than 0.1% carbon, and trace levels of nickel. Although heat treatment cannot harden certain magnetic steels, cold working can strengthen them.

Martensitic: 11–17% chromium, less than 0.4% nickel, and up to 1.2% carbon are found in martensitic steels. Dental and surgical instruments, blades, and cutting tools are all made of these magnetic, heat-treatable steels.

Duplex: Due to the nearly equal amounts of austenite and ferrite in their metallurgical structure, these grades are also known as duplex (or austenitic-ferritic) grades. They are made to be stronger and more resistant to corrosion than typical austenitic stainless steels.

1.4 MOTIVATION

In the modern world, new developments in welding techniques are taking the place of traditional techniques in advanced engineering applications and workplaces. Today, CMT, an improved version of MIG welding, is utilized all over the world due to its reduced heat input, and low dilution, little spatter formation, and improved bead aesthetics. When it comes to its applications, CMT stands out due to this specific feature. CMT is now being used wire-arc additive manufacturing (WAAM), also known as additive manufacturing.

There are many different varieties of stainless steel available, making cladding feasible for a variety of inventive uses. because its ferrite and austenite composition increase strength and offer the best protection against corrosion. Using a full factorial design matrix, a clad layer of different stainless steels (such as austenitic and super duplex stainless steel) is fabricated over low carbon steel plates by CMT. Further effects of various parameters on

bead geometry, dilution, microstructure, microhardness, and tribological behavior is carried out and also compared with the pulse MIG welding process.

1.5 THESIS OVERVIEW

Chapter 1 contains a description of CMT as well as an explanation of how to use CMT for GMAW.

Chapter 2 includes a review of the literature on stainless steel cladding using CMT and other topics. It includes research gaps as well as the numerous discoveries made by researchers in the field of cladding different types of material with these processes. The research objectives and the flow diagram for the experiment are described.

Chapter 3 provides a comprehensive overview of the CMT mechanism, materials, procedures, and experimentation. It also gives detailed information on the manufacturing process of stainless-steel cladding using the CMT and pulse MIG welding process. The principle of CMT welding is discussed in detail in this chapter. Experimental welding input parameters and procedures, microstructure, micro-hardness, wear test, and residual stress have been explained in this section.

Chapter 4 Low carbon steel is used as a base plate on which the 2507 super duplex stainless-steel bead-on-plate experiment is carried out. The process parameters influence on bead geometry and dilution% is discussed in detail. This chapter also covers optimization of bead-on-plate experiments utilizing CCFCD in RSM and microstructural changes with regard to the process parameters. The best parameters are determined, and a validation test is also conducted. Additionally, using the Cold Metal Transfer (CMT) welding technique this

chapter describes the mechanical and wear characteristics of austenitic stainless steel (308L) cladding over low carbon steel. The effect of various normal loads and frequencies are examined using a ball-on-disc reciprocating tribometer over the wear characteristics of the cladding surface in this chapter. Microstructural changes and wear mechanisms with respect to process parameters are discussed.

Chapter 5 includes a result and discussion on weld-clad beads of 308L stainless steel over low-carbon steel utilizing Cold Metal Transfer (CMT) welding and pulse MIG welding processes. The effects of welding speed on the mechanical and wear properties of CMT clad samples and pulse MIG samples are examined and compared. The microstructural analysis, micro-hardness, tensile properties, and residual stresses of the welded joint are discussed.

Chapter 6 includes the conclusions derived from this research, the notable contributions made, and the potential future scope for the area of study.

1.6 SUMMARY

This chapter explores the challenges of weld cladding, including high dilution, residual stresses, distortion, and compromised mechanical properties. It provides an overview of cladding low-carbon steel using Cold Metal Transfer (CMT) welding, highlighting the advantages and limitations of Gas Metal Arc Welding (GMAW) in cladding. The benefits of CMT over GMAW are discussed, along with the motivation for transitioning from GMAW to CMT. The thesis organization and motivation for this research are also outlined.

CHAPTER 2

LITERATURE REVIEW

2.1 INTRODUCTION

This chapter provides a literature review on GMAW-based Cold Metal Transfer cladding (CMT). The literature review has been used to identify the research gap and establish the objectives of the study. A work plan to clad the low carbon steel plate using the CMT welding process is presented. The literature review is discussed in the following area:

- Cladding of stainless steel using GMAW and other welding processes
- GMAW-based CMT cladding of Stainless steel and other alloys
- Cladding of other alloys using different types of welding processes

2.1.1 Cladding of stainless steel using GMAW and other welding process

Murugan & Parmar (1994) studied the influence of different process parameters on 316 stainless steel cladding on structural stainless steel by GMAW process and found that voltage has a predominant influence on width compared to the other parameters, namely current, wire feed rate, welding speed, etc., and also revealed that at low wire feed rates, penetration increased slightly with increasing voltage, while at high wire feed speeds, penetration increases sharply as the voltage increases because at high wire feed rates, the welding current thereby increases the heat input and thus the penetration increases. Chakrabarti et al., (2013) studied the E2209 stainless steel duplex cladding on a structural steel baseplate using the GMAW process and found that under pulsed mode conditions,

even at higher heat input and the lower the oxygen potential of the shielding gas, the nitrogen level does not decrease correspondingly. Due to the increased reaction rate between the substances present in the arc column and the molten weld pool due to the increased fluidity of the molten weld pool under pulse mode conditions. With increasing heat input, the ferrite content decreases. Welds with a heat input of 0.7 kJ/mm were found to have the highest impact on weld strength and those with a heat input of 0.6 kJ/mm had the lowest impact toughness. Shahi & Pandey, (2008) examine the impact of different universal gas metal arc welding (UGMAW) and gas metal arc welding (GMAW) process parameters on dilution in low carbon structural steel plates and single layer 316L stainless steel cladding. The comparison analysis demonstrates that the dilution obtained in the UGMAW process is substantially smaller than that with the GMAW process because the GMAW process involves external preheating of the filler wire, which leads in a bigger contribution of arc energy by resistive heating. Within the range of input parameters studied, wire feed rate was the most important variable affecting dilution, welding speed. Minimum dilution is obtained at lower wire feed rate, voltage and welding speed levels and at a higher nozzle to plate distance. Kumar and Singh (2012) investigated the cladding of 304L SS over low-carbon steel using the GMAW process and discovered that dilution increases with increased voltage and welding current, but decreases with increased NTD. They also found that the lowest dilution percentage was obtained at lower current levels. Kannan & Yoganandh, (2010) investigated the austenitic SS claddings by gas metal arc welding technique using developed mathematical models. They found that as welding speed increases, weld bead width and reinforcement height both decreases. This is because as

welding speed increases and less filler metal is used per unit length of the weld, the heat input per unit length of the weld bead decreases. Forehand welding techniques result in wider weld beads, while backhand welding techniques result in narrower weld beads. With an increase in welding gun angle, the depth of penetration and bead height decrease. Sreeraj & Kannan, (2012) developed a neural network model from experimental data, in order to demonstrate the potential of using neural networks for calculating the desired clad bead geometry of 308 L SS over mild steel plate. The results indicated that neural network models can be utilised as an alternative tool to the current traditional calculation methods. It has been discovered that the average error for bead width, penetration, reinforcement, and dilution is incredibly small. Gomes et al., (2012) examine the effects of the flux-cored arc welding (FCAW) parameters on the 316L SS cladding bead geometry, productivity, and surface quality. They discovered that every factor that was examined significantly impacted how the cladding procedure turned out. Low percentages of dilution are achieved at low voltages, slow welding speeds, and high NTD. Palani & Murugan, (2007) studied 317L stainless steel cladding on a steel structure base plate using the FCAW welding process, and process parameters were also optimized by the response surface methodology. It was found that penetration increased with welding current while decreasing with increasing welding speed and nozzle plate distance. Furthermore, the dilution % increases to a maximum value and begins to decrease as the distance from the nozzle to the workpiece and the welding speed increase. This may be because the weight of metal deposited per unit length decreases as the welding speed increases. However, as the welding speed increases further, the penetration depth decreases, resulting in a decrease in dilution. Eghlimi et al.,

(2013) analyse the impact of dilution on the ferrite number of the super-duplex SS layer to determine its mechanical qualities and corrosion resistance. This is done by depositing super-duplex SS on high- strength low alloy steel substrates using a pulsed current gas tungsten arc cladding process, which revealed that the amount of ferrite decreased as the heat input increased because ferrite turned into austenite. and it was feasible to deposit SDSS on HSLA steel using pulse current gas tungsten arc cladding without the production of harmful intermetallic phases. Kannan & Murugan, (2006) analyse the effects of different flux cored arc welding (FCAW) process parameters on duplex stainless-steel cladding of low carbon steel plates and show that all clad quality parameters, i.e., bead width, penetration, reinforcement, and the dilution increases as the welding current increases due to the increased welding current density and wire fused per unit of time and decrease with increasing distance between nozzle and welding plate and torch angle. Senthilkumar & Kannan, (2015) investigated the super duplex stainless-steel cladding over a low carbon steel base plate and developed a mathematical model to predict the effect of process parameters. They revealed that the reinforcement form factor exhibited a positive correlation with the nozzle to plate distance, while it showed a negative correlation with the wire feed rate, welding speed, and welding gun angle. This can be attributed to the higher rate at which the base metal is exposed under the arc when smaller weld puddle is formed. On the other hand, the penetration factor displayed a positive correlation with the welding speed but a negative correlation with the welding gun angle. Nouri et al., (2007) examined the impact of welding speed, NTD, wire feed rate, and vertical angle of welding on the dilution and weld bead geometry of 316L SS over X65 steel. The results show that as feed

rate increases, dilution% and bead width, height, and depth increase. However, when arc power rises and more base metals melt, the contact angle of the bead initially reduces and then increases. With decreasing the electrode extension, dilution rises by around 6% on average, while the angle of contact falls by about 7^0.

Table 2.1 Major conclusions on cladding of stainless steel using GMAW and other types of welding process

Clad metal and Base metal	Input parameter	Cladding Process	Prominent results	Researcher Name
316L SS Structural steel IS 2062	Voltage (V)-30,32,34,38 Feed rate (m/min)-6,7,8,9,10 Welding speed (cm/min)-20,25.30,50 NTD (mm)-10,13,16,19,22	Gas Metal Arc Welding Process	Voltage has more predominant effect on bead width. The penetration remains unaffected when voltage is 30-31V. On increasing nozzle to plate distance dilution decreases.	Murugan & Parmar (1994)

Super duplex SS Low carbon structural steel,	Welding Current (A)-185 Welding speed (mm/min)-300 Heat input(kJ/mm) -0.78 Wire Feed Rate (m/min)-9	Gas Metal Arc Welding Process	The heat input and the shielding gas significantly influenced the absorption of nitrogen in the weld deposit. Both the heat input and the nature of the shielding gas have an impact on the corrosion characteristics of weld deposits made from duplex stainless steel. The corrosion property worsens as the heat input increases.	Chakrabarti et al., (2013)
316L SS Low Carbon Steel	Wire Feed Rate (m/min)-6,7,8 Voltage (V)-32,34,36 Welding Speed	GMAW and UGMAW	Among the input parameters examined, the wire feed rate had the greatest impact on dilution, followed by and welding speed. Minimum dilution was	Shahi & Pandey, (2008)

	(cm/min)-32,38,44 Nozzle to Plate Distance (mm)-20,22,24		obtained at higher levels of nozzle to workpiece distance and lower levels of wire feed rate, welding speed and voltage.	
304L SS Mild steel	Current(A)-90,150 Voltage(V)-18,24 Nozzle to work distance (mm)-10,15 Welding Speed (cm/min)-25 Gas flow Rate(l/min)-20	Gas Metal Arc Welding Process	Increase in voltage and current increases dilution percentage. On increasing stick out distance dilution decreases. Minimum dilution percentage obtained at lower level of current and voltage and higher levels of stick-out distance.	Kumar & Singh, (2012)
308L SS	Feed rate	Gas Metal	With increase in wire feed	Kannan &

Low carbon steel	(m/min)-4,5,6,7,8 NTD (mm)-18,20, 22,24,26 Welding speed (mm/min)-160,165, 170,175,180	Arc Welding Process	rate bead height, bead width increases and decreases with increase in welding speed. On reducing stick-out distance and increasing speed penetration increases.	Yoganandh, (2010)
308 L SS Mild steel	Welding Current-200,225,250, 275,300 NTD (mm)-10,14,18,22,26 Welding Speed (mm/min)-150,158,166,	Gas Metal Arc Welding Process	To get the optimum clad angle applied limits of process parameters and optimum bead dimensions can be predicted by ANN and PSO.	Sreeraj & Kannan, (2012)

	174,182			
316L SS Carbon steel	NTD (mm)- 10,15,20,25,30 Welding speed (cm/min)- 20 ,30, 40 ,50 ,60	Fluxed Cored Arc Welding Process	Surface quality is affected by NTD. Welding speed 44 cm/min gives maximum penetration.	Gomes et al., (2012)
317L SS Structural Steel IS 2062	Welding current (A)- 176 ,190 ,210 ,230 ,244 Welding speed (cm/min)- 26 ,29 ,34 ,39 ,42 NTD (mm)- 15, 17 ,20, 23 ,25	Flux Cored Arc Welding	Penetration, wire feed rate and reinforcement increase with the welding current, but decreases with the increase in welding speed. When welding speed and nozzle-to-plate distance increase, dilution increases. but starts decreasing on further increasing welding speed and nozzle to	Palani & Murugan, (2007)

			workpiece distance.	
Duplex SS High strength low alloy steel plates	Peak current (A)- 130,140,150, 160,170 Background current (A)- 50,60,70,80,90 Duty cycle (%)- 30,40,50,60,70 Frequency (Hz)- 3,5,7,9	Gas Tungsten Arc Welding Process.	Inverse relationship between dilution and ferrite number is obtained. On increasing the heat input the ferrite number decreases.	Eghlimi et al., (2013)
Duplex SS Low carbon steel	Welding current (A)- 200,225,250, 275,300 Welding speed	Flux Cored Arc Welding	Dilution is directly proportional to the increase in welding current and welding speed, and inversely proportional to the increase in NTD and	Kannan & Murugan, (2006)

	(cm/min)-20,30,40,50,60 NTD (mm)-22,24,26,28,30 torch angle (◦)-20,15,10,05		torch angle.	
Super duplex SS Low carbon steel	Welding voltage (V)-22,24,26,28,30 Wire feed rate (m/min)-5.08,5.715,6.32, 6.985,7.62 Welding speed (m/min)-	Flux Cored Arc Welding	The reinforcement form factor exhibited a positive correlation with the nozzle to plate distance, while it showed a negative correlation with the wire feed rate, welding speed, and welding gun angle. This can be attributed to the higher rate at which the base metal is exposed under the arc when a	Senthilkumar & Kannan, (2015)

	0.12,0.14,0.16, 0.18,0.2 NTD (m)-0.015,0.017,0.019,0.021, 0.023 Welding gun angle (°)-70,80,90,100, 110		relatively smaller weld puddle is formed. On the other hand, the Penetration form factor displayed a positive correlation with the welding speed, but a negative correlation with the welding gun angle.	
316L SS X65 pipeline steel	Wire feed rate (m/min)-4.5,6.2,8 Travel speed (cm/min)-30,50,70	Pulse Gas Metal Arc Welding	As feed rate increases, weld metal dilution and its dimensions i.e., bead width, height, and depth increases. With decreasing the electrode extension, dilution rises by around 6% on average while the angle of contact falls by about 7^0.	(Nouri et al., 2007)

2.1.2 GMAW-based CMT cladding of Stainless steel and other alloys

Evangeline & Sathiya, (2019) studied the cladding of Inconel 625 super alloy over 316L stainless steel using the CMT method and reported that the clad beads have vertically growing Mo and Nb-containing interdendritic and dendritic precipitates. During the cladding process, the wire feed rate and welding speed have a linear relationship with the heat input. According to the EDS report, clad surfaces have a low Fe content. The corrosion performance of the clad region in the 3.5 wt% NaCl solution was better in the area closer to the interface and higher to the substrate, showing excellent protection for Inconel 625. It was also reported that with wear time and applied load, the wear mechanism changes. Lorenzin & Rutili, (2009) observed the cladding of Inconel 625 on 316L stainless steel using GMAW CMT and brazing and reported that among the tested methods, CMT is the most effective, with a 5.6 kg/h deposition rate and an average surface finish of about 4.2 mm. Considering that Inconel 625 wire has a commonly available iron content of 1 to 1.7%, by dilution, the confrontation process contributed to transporting more than 1% on the surface, which is significantly advantageous. The brazing operation appears normal with negligible deformation due to shrinkage, made in a single pass. Pickin et al., (2011) deposited Al 4043 filler wire over the Al 2024 plate through the CMT process and observed that the short circuit duration could be adjusted to control penetration. An increase in the duration of the short circuit reduces the penetration with a small reduction in the volume of weld material deposition. G.P. et al., (2019) studied the cladding of stellite over H13 steel with CMT and plasma transferred arc welding (PTAW) methods. The average volumetric dilution of the CMT process is lower than that of the PTAW. The microhardness of the clad region has a

similar range in both processes due to its finer dendritic structure. The wear properties of CMT-clad samples are better than those of PTAW samples due to the greater volume of ε-hcp being transformed from filler material to the clad surface. CMT shows better wear performance at room temperature than PTAW. Rajeev et al., (2014) investigated the cladding of an Al-Si-Mn alloy over an Al plate by the CMT process and the thermal spray process and learned that the CMT provides low-dilution clads. The deposition rate, bead angle, and dilution are nonlinear functions of welding speed. The CMT process produces a 2.5-mm thicker cladding than the thermal spray process. Benoit et al., (2015) compared MIG, pulsed MIG, CMT, and TIG for the cladding of ER5356 over the Al6061 plate and reported that the peak temperature for the pulse-mix CMT method is higher, yet it generates a similar rate of cooling as other MIG processes. Compared to other MIG processes, the pulse-mix CMT technique produces beads of higher quality. The HAZ of the CMT sample had the highest level of residual stress. The TIG process creates clad with no detectable porosities and negligible residual stress because the higher heat input encourages the removal of porosity from the fusion zone. Because of this, no porosity can be seen in the radiography. The TIG process has the greatest negative impact on the parent metal's mechanical characteristics. Liang et al., (2017) investigated the cladding of ER4043 Al over 6061 Al plates using TIG-CMT hybrid welding. and concluded that the TIG current influences the contact angle and dilution of the weld bead and improves the wettability of the molten metal. The decrease in microhardness in the partially melted zone (PMZ) is attributed to the finer grain structure compared to the heat-affected zone (HAZ). Additionally, solution strengthening takes place in a specific region inside the PMZ. The suitability of the suggested TIG-CMT hybrid

welding technique for multi-pass welding of aluminum alloy has been demonstrated. Ola & Doern, (2014) performed the cladding of Inconel 718 super alloy over Si and balance Ni plates using the CMT cladding method and concluded that CMT is found to be suitable for low-dilution cladding and clads are free from cracking and porosity. The wire feed rate was linearly related to the heat input. A contact angle greater than 115° is recommended. Solecka et al., (2018) investigated CMT clad layers of Inconel 625 on 16Mo3 steel and found that the clad layers had a cellular-dendritic microstructure, and strong saperation of Mo and Nb particles in the inter-dendritic regions causes a significant increase in hardness in the clad region. Evangeline & Sathiya, (2019b) examined the metallurgical, mechanical, and corrosion properties of dissimilar cladding between Ni-Cr-Mo superalloy and 316L austenitic stainless steel using CMT. The results show that columnar and coaxial dendrites are observed in close proximity to the clad region at the interface, while cellular and columnar dendrites are observed near the fusion border. The microhardness of the clad surface is greater than that of the interface and base, mostly because of the lower heat input and faster cooling rate, resulting in a decrease in the spacing between dendritic arms. The greater hardness of the clad surface is also attributed to the presence of carbides and hard intermetallics. Based on the results, the Ni-Cr-Mo alloy provides protection against corrosion for the substrate. [Luchtenberg et al., 2019)] evaluated the duplex SS weld clad properties on a mild steel plate (ASTM A 516 Gr 60) and demonstrated that as the welding heat input drops, the amount of ferrite and partially converted austenite (PTA) reduces as well. Because there are more austenite/austenite and austenite/ferrite interfaces in the weld overlay than in the rolled S32205 plate, its hardness is higher. The quantity of secondary austenites in the overlay

coatings has little effect on hardness. Conversely, because of the austenite's working hardening, resistance to abrasive wear rises as the quantity of secondary austinites does.

Table 2.2 Major conclusions on GMAW-based CMT cladding of stainless steel and other alloys

Clad metal and Base metal	Input parameter	Cladding Process	Prominent results	Researcher Name
Inconal 625 super alloy 316 L SS	Current(A)- 140,160, 180 Voltage(V)- 17,19,21 Torch Angle (°)- 60,70,80 Welding Speed- (mm/min) 125,150 175 Wear Test- Applied load- 90N,50N and 20N	Cold Metal Transfer	The clad beads have vertically growing Mo and Nb-containing inter-dendritic and dendritic precipitates. Clad surface has a low Fe content. The corrosion performance of the clad region in the 3.5 wt% NaCl solution was better in the area closer to the interface and higher to the substrate, showing excellent	Evangeline & Sathiya, (2019)

			protection for Inconel 625.With wear time and applied load, the wear mechanism changes.	
Inconal 625 316L SS	Bead Current (A)-150 152 153 Voltage (V)- 16.8,16.9,17.0,17.2,17.3	GMAW, Brazing and Cold Metal Transfer	The CMT method is the most promising, as it has a deposition rate of 5.6 kg/h and an average surface finish, height about 4.2 mm. The confrontation process contributed to transport more than 1% on the surface. The brazing operation appears normal with negligible deformation due to shrinkage, made in a single pass.	(Lorenzin & Rutili, (2009)
Filler 4043 Filler 2319	CMT Current (A) -	Cold Metal Transfer	The CMT technique allows for better control	Pickin et al., (2011)

Alloy 2024	144 Voltage (V)-16 Wire feed rate (m /min)- 6. Pulse cladding – Current(A)152 Voltage (V)-19.5 Wire feed rate (m /min−6.8 1.		of dilution, which enables the deposition of a quasi-binary (Al–Cu) layer with a composition that is less prone to cracking. Conventional MIG welding can be applied on top of this layer, perhaps eliminating cracking by employing a binary filler wire.	
Stellite21 H13 steel	CMT: Wire feed rate (m/min)-3.1 Current(A)-117 Voltage(V)-9.6 Speed(mm/min) 127 PTAW: Gas flow rate	Cold Metal Transfer and Plasma Transferred Arc Welding processes	The average volumetric dilution of CMT is lower than that of PTAW, whereas the micro hardness is similar. CMT shows better wear performance at room temperature than	G.P. et al., (2019)

	(LPM)-9 Plasma gas (Ar) flow rate (LPM)-2.7 Powder gas (Ar) Powder flow rate(g/min)-17 Voltage(V)-16 Current(A)-155		PTAW.	
Al-Si-Mn alloy Al plate	Voltage (V)-12.5 Current (A)-80 Wire feed rate (m/min)-4.8 Nozzle-to-plate distance (mm)-5 Welding speed (in./min) 15,20,25	Cold metal arc transfer Cladding	The CMT provides low dilution clads as compared to thermal spray. The deposition rate, bead angle and dilution are nonlinear functions of the welding speed. As compare to thermal spray processes thicker coating of 2.5 mm can be produced.	Rajeev et al., (2014)

5356 Al 6061Al plates	MIG Current(A)-135, Voltage(V)-15.3 Wire speed(cm/min)-7 PULSED MIG Current(A)-105 Voltage(V)-18.2 Wire speed(cm/min)-6 CMT Current(A)-113 Voltage(V)-18.2 Wire speed(cm/min)-6.5 TIG Current(A)-107 Voltage(V)-12.5	MIG, Pulsed MIG, CMT and TIG	Pulsed MIG and CMT mix produces better quality of bead other than TIG and MIG. TIG produces clad without visible pores and low residual stress and additionally, it is the most detrimental process for the mechanical properties of the parent metal.	Benoit et al., (2015)

	Wire speed(cm/min)-2.5			
ER4043 Al Si 5% 6061Al plates	Welding speed (mm/s)- 5,7,9 CMT Welding current (A)- 0,50,60,70 TIG Welding current- 0,60,80,100	TIG-CMT Hybrid Welding	The TIG current effect the contact angle and dilution of weld bead and improves the wettability of the molten metal. Partial melting zone grains are finer than heat affected zone grains, and solution strengthening reduces microhardness. The suggested TIG-CMT hybrid welding technology is ideal for multi-pass aluminum alloy welding.	Liang et al., (2017)
Inconel 718 super alloy	Wire feed rate (m/min)-6,8,10	Cold metal arc transfer	CMT is found to be suitable for low	Ola & Doern,

Si/Ni alloy plate	Speed (m/min)-0.9,1.5,2.1 Push angle (degrees)-5,15,25	Cladding	dilution cladding and clads are free from cracking and porosity. Wire feed rate was linearly related with the heat input. A contact angle greater than 115^{o} is recommended.	(2014)
Inconel 625 16Mo3 boiler tube	Current (A)-200 Voltage (V)-20 Gas flow rate (l/pm)- 17 Feed rate (m/pm)- 0.8	Cold metal arc transfer cladding	The Clad layers had the characteristic cellular-dendritic microstructure. EDS showed Ni, Cr, and Fe micro-segregation into clad layer dendritic areas. In Laves phase nickel, chromium, niobium, and molybdenum were abundant. The interdendritic regions	Solecka et al., (2018)

			have higher hardness than the dendritic regions due to substantial Mo and Nb segregation.	
Inconal 625 316L SS	Current (A)-140,160,180 Voltage(V)-21 Torch Angle (°)- 60,70,80 Travel Speed-(mm/min) 125,150 175	Cold Metal Transfer	The clad surface has higher microhardness than the interface, and base. Ni-Cr-Mo alloy protects the substrate against corrosion. A unique type of cubic precipitate was observed due to the presence of Ti, forming Ti-containing carbonitride, further characterized as NbC.	Evangeline & Sathiya, (2019b)
ER 2209 Duplex SS	Welding Current (A)-	Cold Metal Transfer	The quantity of ferrite and partially transformed	Luchtenberg et al.,

S32205 plates	215 Welding Voltage (V)- 20 Welding Speed (cm/min)- 36,30,23,15		austenite decreases as the heat input decreases. The weld overlay has a higher hardness compared to the rolled S32205 plate because of the numerous interfaces between austenite and ferrite, as well as austenite and austenite. The resistance to abrasive wear is enhanced as the secondary austenites increase, owing to the working hardening of the austenite.	(2019)

2.1.3 Cladding of other alloys using different types of welding process

Benoit et al., (2015) compared MIG, pulsed MIG, CMT, and TIG for the cladding of ER5356 over the Al6061 plate and reported that the peak temperature for the pulse-mix CMT method is higher, yet it generates a similar rate of cooling as other MIG processes. Compared to other MIG processes, the pulse-mix CMT technique produces beads of higher quality. The HAZ of

the CMT sample had the highest level of residual stress. The TIG process creates clad with no detectable porosities and negligible residual stress because the higher heat input encourages the removal of porosity from the fusion zone. Because of this, no porosity can be seen in the radiography. The TIG process has the greatest negative impact on the parent metal's mechanical characteristics. Alvarães et al., (2020) examine the mechanical and microstructural characteristics of an Inconel 625 weld cladding over Gr. 70 steel plate deposited by electroslag welding (ESW). It is found that the presence of Cr, a key alloying element in Ni-based alloys, plays a crucial role in preventing pitting corrosion and facilitating the development of a durable oxide layer that offers excellent corrosion resistance. Additionally, the material's ability to reestablish its protective properties is influenced by the Mo content. Considering its ability to produce single-layer cladding with strong mechanical properties, ESW could be a compelling alternative for use in industrial equipment. The minimal production of secondary phases during the ESW process is essential for achieving excellent resistance to corrosion. Shayanfar et al., (2020) explored the single-pass Inconel 625 cladding over A592 and developed a statistical approach utilizing regression analysis. It was found that the dilution varies depending on the coating powder and substrate. By adjusting the rate of powder injection, scanning rate, or injectable powder ratio to the length of the cladding layer (F/V), the penetration depth can be reduced while keeping the laser power constant. When (F/V) increases, the substrate receives less laser energy, causing the powder to absorb more laser energy and resulting in a decrease in penetration depth. Abioye et al., (2015) studied Inconel 625 cladding over 304 SS using laser cladding and revealed that it is possible to deposit Inconel 625 multiple beads utilizing wire as the feedstock material in a pore- and crack-free,

slightly diluted, and well-bonded manner. The equivalent multiple-bead layer exhibits less Fe dilution than the single bead. In this investigation, a minimum Fe dilution of 4.5% was discovered for both single and multiple laser-clad inconel 625 wire beads. The Inconel 625 wire laser coatings may effectively protect components made of stainless steel since the corrosion product's thickness was less than 0.1 mm at the top surface, which are around 4 mm thick. Singh et al., (2020) studied the mechanical and wear characteristics of WC-10Co-4Cr cladding deposited on AISI 304 SS using TIG welding and found that the current has the greatest impact on wear resistance and hardness followed by welding speed and NTD, and that the argon gas flow rate has the least impact. The enlarged image displays the development of dendritic microstructure in the cladding, coupled with a few partially melted WC grains. The nucleation and development of nano-WC particles have resulted in submicron, angular, and dendritic microstructures due to high heat input. Lotfi et al., (2014) utilize TIG welding to create a clad layer with SiC particles in an Al-Si eutectic matrix. The creation of needle-shaped Al4SiC4 and a fine dispersion of acicular silicon inside the matrix were the results of the 30% SiC addition. Eutectic crystals and coarse silicon particles formed in the clad layer as a result of adding 7.2% or 12% silicon to the initial powder mixture. The initial powder mixture's hardness was boosted by adding more silicon and SiC components. The Al20SiC12Si clad layer has the highest surface hardness and resistance to sliding wear. Baidridge et al., (2013) discovered that the high-power Yb fiber laser appeared to achieve the highest cladding quality with the least amount of porosity and surface flaws when inconal 690 over inconal 600 alloy was tested using the laser cladding method. It is possible to increase the resistance of Inconel 690 to ductility-dip cracking by sparingly including additives like

lanthanum, molybdenum, or niobium. The cooling rate of the cladded layer is influenced by the preheating temperature, laser power and intensity, material shape, and thermal conductivity.

Table 2.3 Major conclusions on Cladding of other alloys using different types of welding process

Clad metal and Base metal	**Input parameter**	**Cladding Process**	**Prominent results**	**Researcher Name**
5356Al 6061Al plates	MIG Current(A)-135 Voltage(V)-15.3 Wire speed(cm/min)-7 PULSED MIG Current(A)-105 Voltage(V)-18.2 Wire speed(cm/min)-6 CMT	MIG, Pulsed MIG, CMT and TIG	Pulsed MIG and CMT mix produces better quality of bead other than TIG and MIG. TIG produces clad without visible pores and with residual stress and additionally, it is the most detrimental process for the mechanical characteristics of the	Benoit et al., (2015)

	Current(A)-113 Voltage(V)-18.2 Wire speed(cm/min)-6.5 TIG Current(A)-107 Voltage(V)-12.5 Wire speed(cm/min)-2.5		parent metal.	
Inconal 625 A516 70 steel plate	Current (A)-1200 Voltage -25 Heat-input (kJ/mm)- 11.7	Electroslag welding Process (ESW)	Cr in the Ni-based alloys, control the initiation of pitting corrosion and promote stable passive oxide layer formation i.e. highly resistant to corrosion. The material's passivation ability is	Alvarães et al., (2020)

			controlled by the Mo content. ESW's decreased secondary phase production is key to its corrosion resistance.	
A516 70 steel plate	Scanning rate (m/s)-3,4,5 Powder feeding rate (mg/s)-100,200,300 Laser power Inconel 625 powder (w)-150,200,250,300	Laser Cladding Process	Dilution changes with altering the cladding powder and substrate. As the ratio of (F/V) increases, less laser energy is delivered to the substrate, resulting in more laser energy being absorbed by the powder and a lower penetration depth.	Shayanfar et al., (2020)
Inconal 625 304 SS	Laser Power (kW)- Transvers Speed (mm/s)-	Laser Cladding Process	The equivalent multiple bead layer exhibits less Fe dilution than the	Abioye et al., (2015)

	Wire Feed Rate-(mm/s)-		single bead. The Inconel 625 wire laser coatings may effectively protect components made of stainless steels since the thickness of the top surface of the multiple-clad beads was less than 0.1 mm, while the overall thickness of the beads was approximately 4 mm.	
WC -10Co -4Cr 304 SS	Welding Current (A)- 50-90 Argon Flow Rate (L/min)-9-13 Stand-off Distance (mm)-1.5-2	Tungsten Inert Gas (TIG) Welding Process	Current has the greatest impact on hardness and wear resistance, welding speed and standoff distance, and that argon gas flow rate has the least impact.	Singh et al., (2020)

			The nucleation and development of nano-WC particles have resulted in submicron, angular, and dendritic microstructure due of high heat input.	
Al−Si/Si-Cp composite A380 Al alloy	Current (A)-140 Voltage (V)-10 Heat-input (Kj/cm)-67	Tungsten Inert Gas (TIG) Welding Process	Needle-shaped Al4SiC4 and a fine dispersion of acicular silicon inside the matrix were obtained due to the 30% SiC addition. 7.2% or 12% silicon in the original powder mixture created coarse silicon particles and eutectic crystals in the clad layer. The initial powder	Lotfi et al., (2014)

			mixture's hardness was boosted by adding more silicon and SiC components. The Al20SiC12Si clad layer has the highest surface hardness and resistance to sliding wear.	
Inconal 600	Stage axes-2,3 Wave length (nm)- 940,808,1064,1070 Max power (W)- 170,800,420,3000 Feed rate (g/min)- 21–39,2.7–4.0, 25–35	Laser Cladding Process	It is possible to increase the resistance of Inconel 690 to ductility-dip cracking by including additives like lanthanum, molybdenum, or niobium. The cooling rate of the cladded layer is influenced by the preheating	Baidridge et al., (2013)

			temperature, laser power and intensity, material shape, and thermal conductivity.	

2.2 RESEARCH GAPS

It is clear from the above literature review that:

1. From literature review it has been discovered that a many research work has been completed on cladding using GMAW, GTAW, FCAW and other welding processes yet at the same time need to investigate further in cladding process by CMT.
2. While certain authors have examined the range of clad materials (substrates), shielding gases at varying flow rates, welding speed, feed rate, and so forth, and how these factors affect the shape, microstructure, and dilution of beads, their interactions with wear characteristics and mechanical properties are not examined together.
3. It has been found that there is a dearth of research on the cladding of Austenitic stainless steel over low-carbon steel using CMT. In addition, very limited work is done on the wear behaviour of CMT clad.
4. There is dearth of studies on the comparison of different cladding techniques of mild steel.

2.3 RESEARCH OBJECTIVES

The following objectives are formulated:

1. Fabrication of various stainless cladding of low carbon steel by CMT process.
2. To study the effect of various process parameters on bead geometry.
3. Optimize the effect of process parameters for best clad layer properties.
4. To study of microstructure and mechanical properties of clad bead.
5. To study of wear properties of clad bead.

2.4 FLOW CHART FOR PRESENT WORK

The various stages of the research activity are as described below:

i. Literature survey.
ii. Selection of work material and filler metal.
iii. Experimental work.
iv. Welding parameters.
v. Optimization of process parameters using RSM.
vi. Testing of clad bead and surface.
vii. Analysis of results
viii. Comparative study of CMT with Pulse MIG process.
ix. Conclusions

The flow chart provides an overview of the whole work. The flow chart for the current work, which details the methodological steps taken during this investigation, is shown in Fig. 2.1.

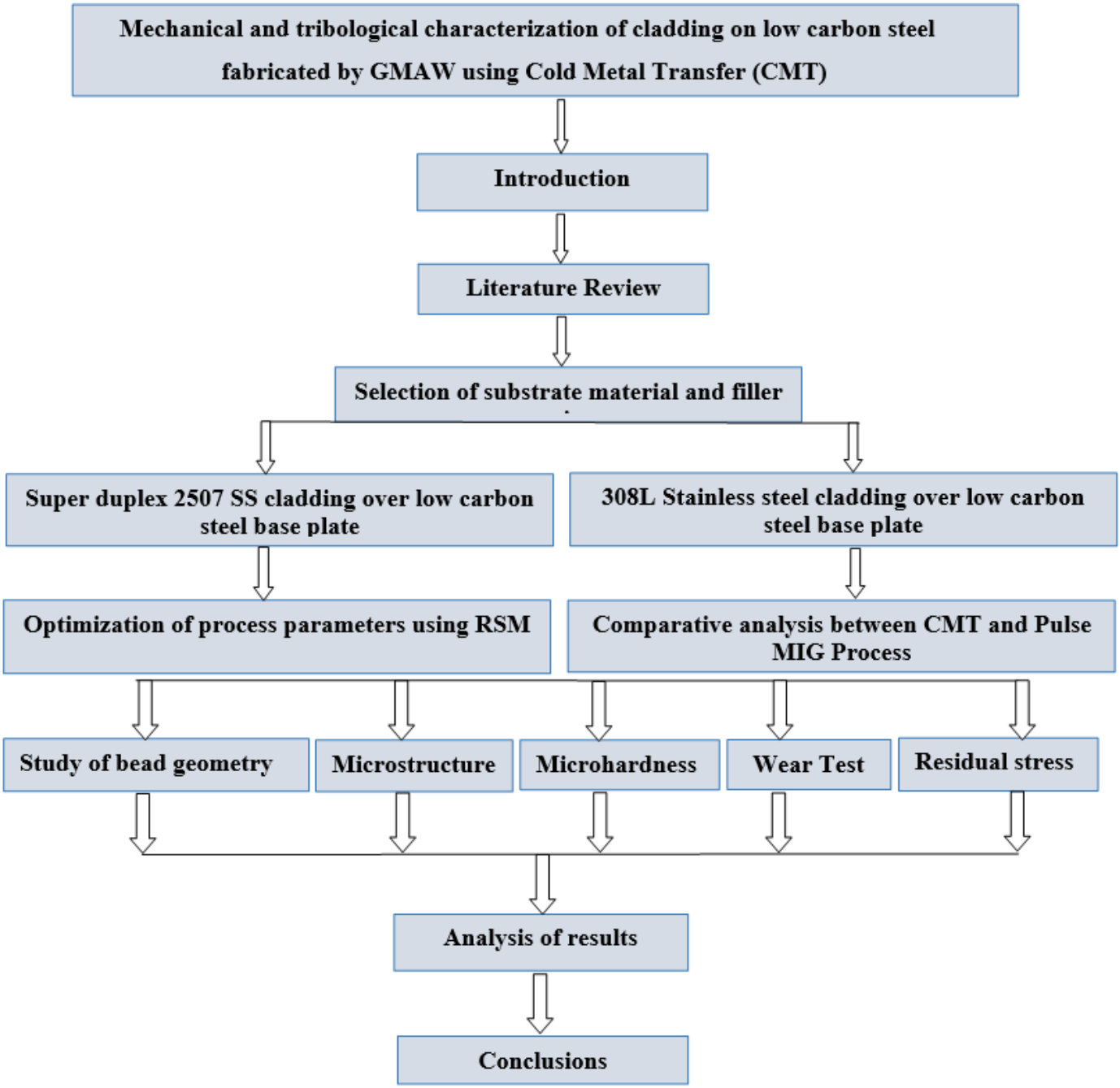

Fig. 2.1 Flow chart of present research work

2.5 SUMMARY

This chapter presents a detailed review of the cladding using the CMT welding process on stainless steel. Major conclusions are highlighted for cladding stainless steels and other alloys over base plates using the GMAW/CMT welding process. The different methods of cladding, process parameters, and other clad material and filler wire combinations and the mechanical and microstructural studies of CMT cladding by numerous researchers are discussed. The core inferences drawn from this study are:

1. The geometry of the bead has a considerable impact on the clad quality. It was seen from the inspection that the importance of the impact of the parameters, i.e., open circuit voltage, wire feed rate, nozzle to work distance, heat inputs, and welding current, on the dilution and bead geometry cannot be ignored.
2. The CMT welding process has the advantage of controlled heat input over conventional GMAW. And also, a new CMT process with suitable process parameters would be suitable for improving the affected areas and servicing damaged and worn-out components.
3. Heat input is influenced by the wire feed rate, current, and welding speed. The wire feed rate and current directly influence the heat input.
4. Some hybrid techniques, i.e., the TIG-CMT hybrid process, the plasma GMAW hybrid process, etc. has also been discussed and found that the hybrid process is suitable for multi-pass welding with high deposition rate and low dilution.
5. The microstructural and mechanical properties of stainless-steel cladding are affected by various process parameters. This can be improved by optimizing these process parameters.

CHAPTER 3

EXPERIMENTAL SETUP & PROCEDURE

3.1 SELECTION OF MATERIAL

3.1.1 Substrate/Base Material

Low carbon steel (IS 2062) of thickness 5 mm was chosen as the base plate for cladding using a CMT welding machine. Low-carbon steel is the most favored type of steel due to its affordability and ability to provide suitable material properties for a variety of applications i.e., shipbuilding, automobile and domestic appliances. Low carbon steel is containing between 0.05 and 0.30 percent carbon. Although low carbon steel is simple to produce and inexpensive, it has a relatively low tensile strength. The substrate material taken for experiments is shown in Fig. 3.1.

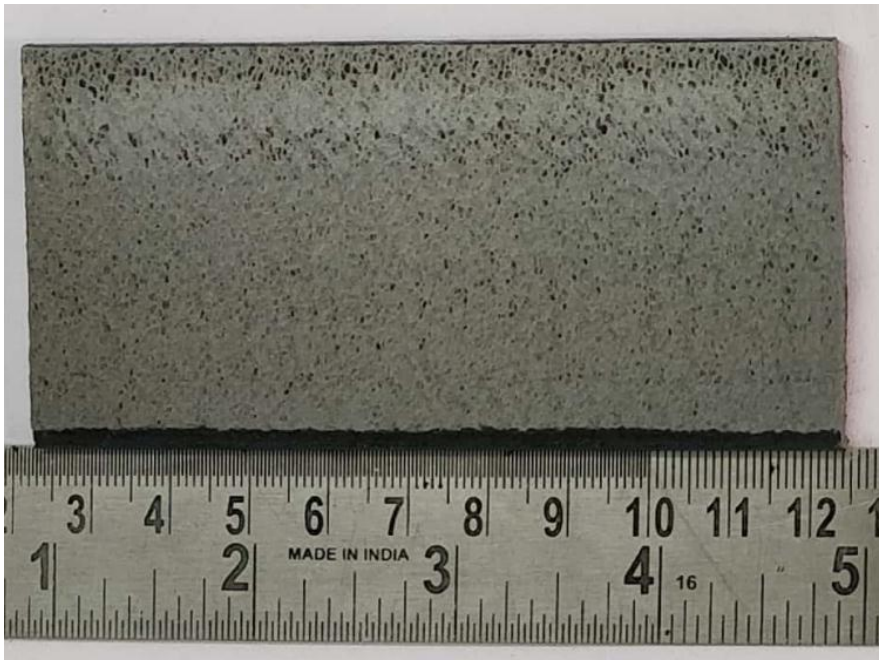

Fig. 3.1 Low carbon steel base plate

The chemical composition of the substrate materials, analyzed using chemical spectroscopy in line with ASTM E415, is summarized in Table 3.1. Additionally, Table 3.2 provides an overview of the base material's mechanical characteristics

Table 3.1 Chemical composition (% weight) of the base plate

IS-2062 Low carbon Steel								
C	Si	Mn	P	S	Ni	Cr	Al	Fe
0.13	0.16	0.58	0.02	0.02	0.02	0.04	0.02	Balance

Table 3.2 Mechanical properties of base material

Properties	σ_{UTS} (MPa)	σ_{YS} (MPa)	δ (%)	$HV_{0.5}$
Low carbon steel	400-500	250	10-30	175
δ – Elongation; $HV_{0.5}$ – Vicker's microhardness at 500 grams load; σ_{UTS} – Ultimate tensile strength (UTS)				

3.1.2 Filler/Clad material

Austenitic steel AISI 308L and super duplex 2507 filler wire having 1.2 mm diameter is used to clad the base plate. The chemical compositions (% weight) of filler materials determined by chemical spectroscopy in accordance with ASTM E 1086 are displayed in Table 3.3. Table 3.4 displays the mechanical properties of the filler wire.

Table 3.3 Chemical compositions (wt %) of AISI 304 SS and ER 308L SS

Materials	Fe	Cr	Mn	Ni	Si	C	P	S	Mo
ER308L	Bal.	19.15	1.42	10.03	0.42	0.029	0.02	0.01	0.25
Duplex 2507	Bal.	25	1.20	8	0.80	0.030	0.035	0.020	4

Table 3.4 Mechanical properties of filler wire

Properties	σ_{UTS} (MPa)	σ_{YS} (MPa)	δ (%)	$HV_{0.5}$
AISI 308 L	585	234	60	230
Duplex 2507	920	550	1.8	300
δ – Elongation; $HV_{0.5}$ – Vicker's microhardness at 500 grams load; σ_{UTS} – Ultimate tensile strength (UTS)				

3.2 PREPARATION OF SAMPLE

3.2.1 Macrostructure and microstructure study

The macrostructure of the weld bead dimensions is used to understand the depth of metal penetration and helps to study the weld strength and quality of the weld. The specimens were made by extracting a 10 x 10 mm sample from the weld bead. The cross section of samples were polished using emery paper with varying grades, ranging from 100 to 2000. Both dry and wet polishing techniques are required to examine the macrostructure of the weld bead. The cross-section of the clad bead sample's microstructure was observed using an optical microscope. The cross-section specimens were polished with 320, 400, 600, 800,

1000, 1200, 1500, 1800, and 2000 grits of emery sheet. Then samples are polished with velvet cloth polishing using three grades of I, II, and III alumina suspension. The 308 L polished surface was etched with the (30 ml HCl + 120 ml distilled water + 10 g $FeCl_3$) [Roy et al., (2021)] for 20 seconds and super duplex 2507 samples were etched using 80 ml of deionized water + 20 ml HCl + 0.3 g sodium metabisulfite [Zhu et al., (2021)]. The samples are washed with distilled water and then dried with a drier to remove the carbon deposits. The microscopic study was carried out using the optical microscope.

3.2.2 Microhardness

Vicker's microhardness tester (STRUERS) was used to estimate the hardness of the fusion region and HAZ of the weld bead samples with an applied load of 500 gm for dwell period of 10 s as per ASTM E384 standard. Before testing, the hardness sample was mounted with bakelite powder in a mounting press to facilitate preparation and testing. Then the specimens were polished up to 1200 grit fine emery paper and by alumina polishing. A diamond pyramid indenter was used to make an indentation. Three indentations were carried out laterally for experimental purposes, and the average of three hardness values was taken for all the samples.

3.2.3 Wear Testing

Wear tests were conducted using a linear reciprocating ball on disc tribometer (DUCOM) as per ASTM standards G133-05. Wear test disk sizes of 20mm x 20mm were taken-out from the middle of the CMT and pulse MIG cladded surface by wire EDM. The wear test specimens are grounded at 0.2 μm surface roughness (Ra) using different emery grade sheets. A tungsten carbide (WC) ball diameter of 8 mm was tested against wear test

specimens. Reciprocating wear tests were performed at a different frequency and normal loads with a constant time of 1000 seconds. All the wear tests were performed three times to ensure repeatability.

3.2.4 Residual Stress

The Pulstec μ-X360n: Advanced HR-XRD for high-resolution 2D X-ray analysis is utilized to measure residual stresses at different locations. Residual stress specimens of 10 mm x 10 mm are extracted from the middle of welded samples by a wire EDM machine. Before the testing, samples are polished with different grades of emery (180, 320, 400, 600, 800, 1000, 1200, 1500, 2000, and 2500) sheets.

3.3 DETAILS OF EXPERIMENTAL MACHINES

3.3.1 CMT Machine

The CMT machine (TPS400i) (Fig. 3.2) is utilized in this study, and the technical specifications are provided in Table 3.5. The total duration of CMT process is reduced to one-fourth during the short-circuit phase, when the maximum current approaches zero. It significantly reduces energy usage by 30% to 40% in comparison of GMAW. During the short-circuiting phase, if a short-circuit occurs, the digital process control system promptly sends a signal, to withdraw the filler wire using the modular power source. This action instantly decreases the current level in this phase. This decrease in electrical current contributes to a decrease in heat input (HI), minimum splatter, low dilution, minimal distortion, and other benefits. [Cao et al., (2008), Lorenzin & Rutili, (2009)].

The CMT machine utilizes direct current electrode positive (DCEP), also known as direct current reverse polarity (DCRP). In this setup, the welding torch that contains the wire electrode is connected to the +ve terminal of the CMT power source, while the base metal (BM) is connected to the -ve terminal. The implementation of DCEP/DCRP is based on the direction of electron flow, where electrons move between negative to positive terminal in the arc column. This flow of electrons contributes to achieving uniform deposition. The positive ions are drawn towards the base metal, resulting in a significantly higher temperature upon impact. This leads to more heat dissipation in the base metal compared to the wire electrode tip, which aids in enhancing penetration. Direct current electrode negative (DCEN) produces welds that are thicker, but the arc is unstable and there are many interruptions in the arc. This means that altering one of these parameters will also result in changes to the other two. Arc length correction is the coefficient that adjusts the arc length, enabling even greater precision in controlling heat input. The range varies from a decrease of 10% to an increase of 10%. The negative range is utilized to achieve a shorter arc length, resulting in a narrower weld bead and more penetration by reducing the voltage. The positive range is utilized to achieve a longer arc length, resulting in a broader weld bead and reduced penetration by increasing the voltage. Zero represents the neutral arc length.

Pulse dynamic correction is a technique used to adjust the pulses frequency per second. The range varies from “-10% to +10%.” The negative range refers to a decrease in the force or energy required to detach droplets, resulting in a shorter arc length while maintaining the same stickout distance. It decreases the duration and magnitude of the

electrical pulses, hence increasing the frequency per second. The positive range refers to an increase in the force or energy required to detach droplets, which in turn increases the length of the arc while maintaining a consistent stickout distance. It elongates the duration and magnitude of the pulses, hence decreasing the frequency per second. Hence, it reduces penetration by creating a broader weld bead.

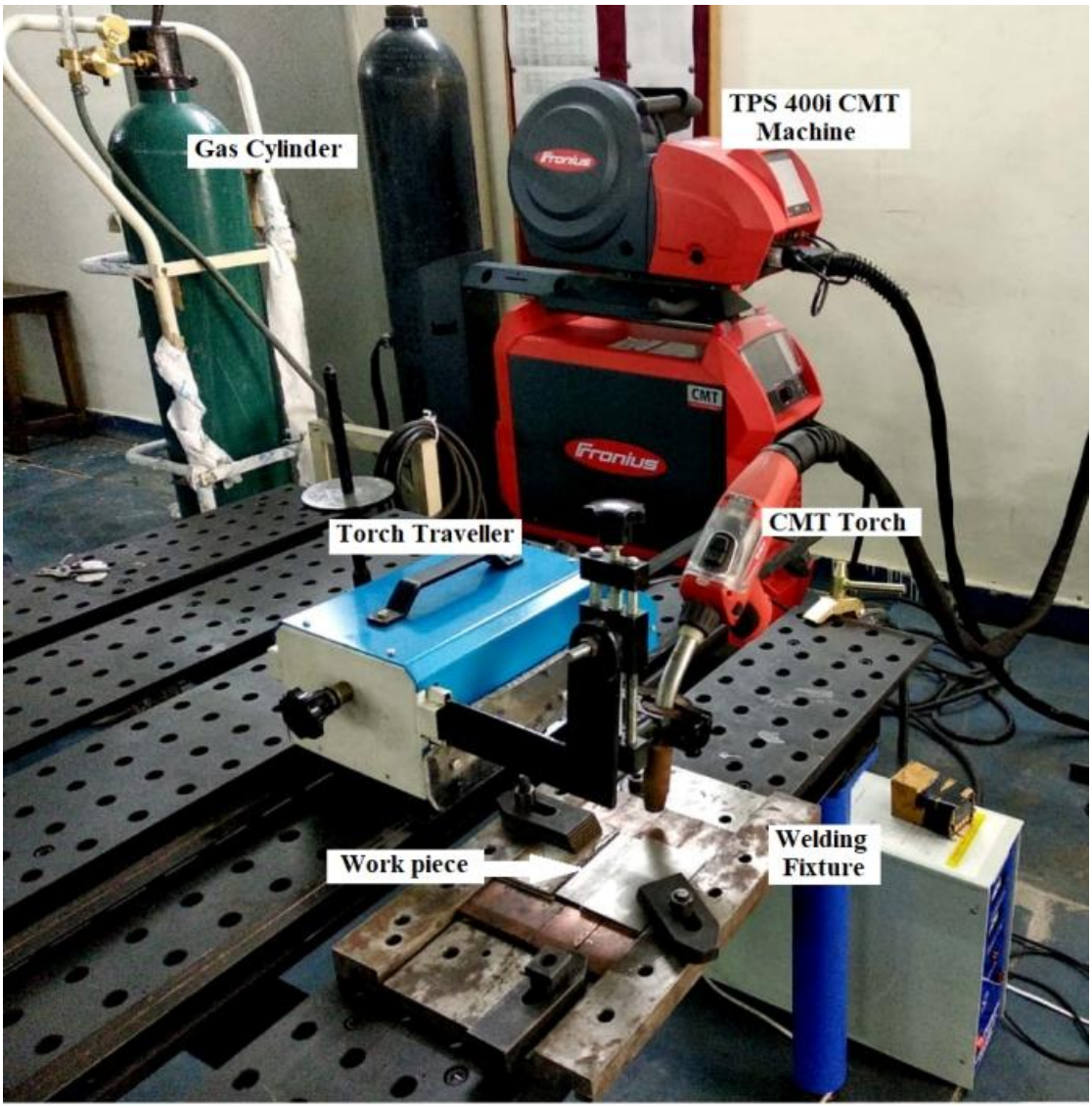

Fig. 3.2 CMT welding machine (TPS400i)

Table 3.5 CMT welding machine specifications (TPS 400i)

Main Voltage	3×460V
Main range	323-529 V ac
Fuse Protection	35A slow blow
Mains tolerance	+/- 15%
MIG current range	3-400 A
MIG voltage range	14.2-34.0
Duty cycle 104^{O} F (40^{O} C)	400 A @ 40%
	360 A @ 60%
	320 A @ 100%
Degree of protection	IP 23
Dimensions (L×W×H) mm	706×300×510 mm
Weight	32.5 kg

3.3.2 Wear Testing Machine

The principle involves applying pressure and motion to a pin or ball against a flat object, either in a dry or heated state. The upper specimen undergoes a linear reciprocating motion, which can be adjusted by manipulating the load, frequency, stroke length, and temperature. The load is exerted by the top specimen as it presses against the horizontally mounted flat lower specimen. The software receives input for the load, stroke length, frequency, temperature, and test time. Meanwhile, the software acquires and displays the frictional force. The dimensional change of both the ball and flat specimen is measured after the test

in order to determine the wear volume and wear rate. The sensor measures the friction force during the test and shows it on the screen. It can be utilized to evaluate variations in the contact state or the kinetic friction coefficient over time. The device operates using the WINDUCOM 2010 software, which consists of many screens. A single screen is used to input test parameters for operating the test rig and simultaneously collect sensor output to store and display on the screen. The second screen is used to evaluate the test results, while the third screen is used for calibrating the test apparatus.

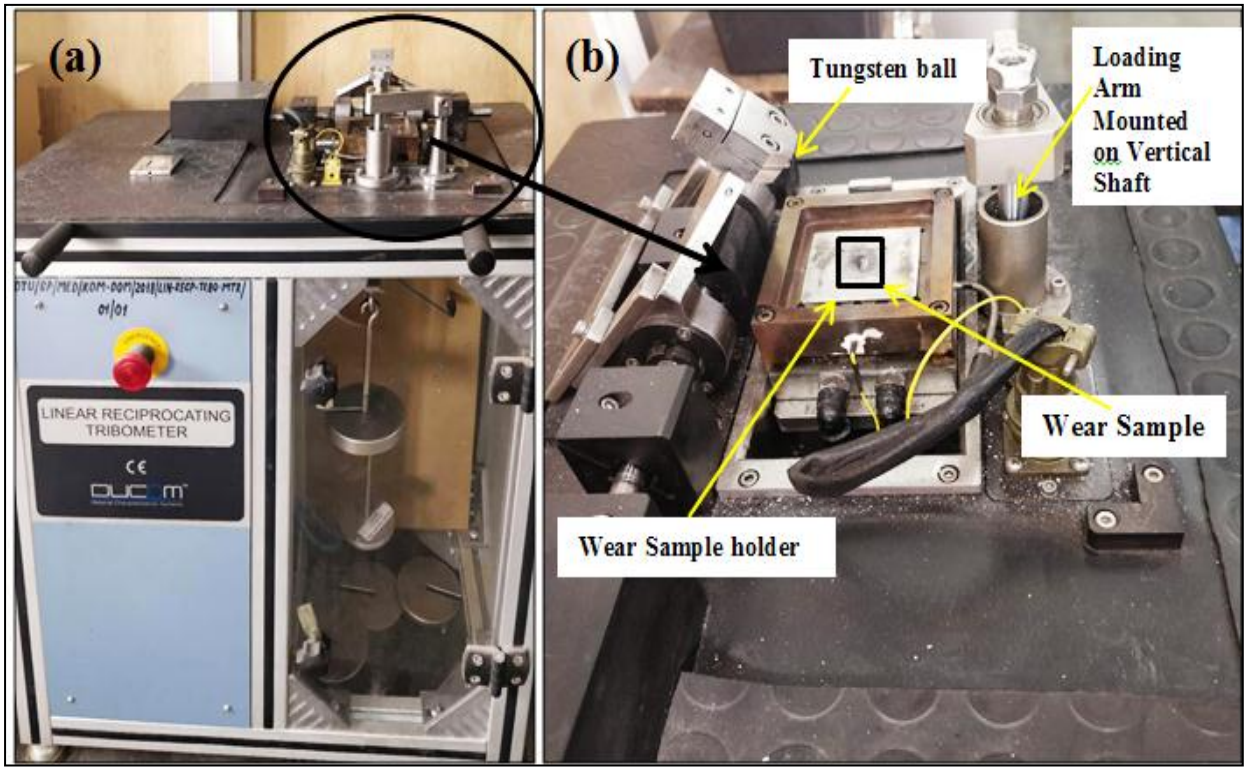

Fig. 3.3 Tribology machine (Model: DUCOM Linear reciprocating tribometer)

Table 3.6 Wear Testing Machine specifications

Normal Load	N	5-50
Frequency	Hz	Up to 50Hz
Stroke	Mm	1-20
Frictional Force	N	0-50
Temperature	^{0}C	Ambient to 550 ^{0}C
Data acquisition card	NI-6321	
Total Height	Mm	920
Size L×B×H	Mm	600×520×920

3.3.3 Microhardness Machine

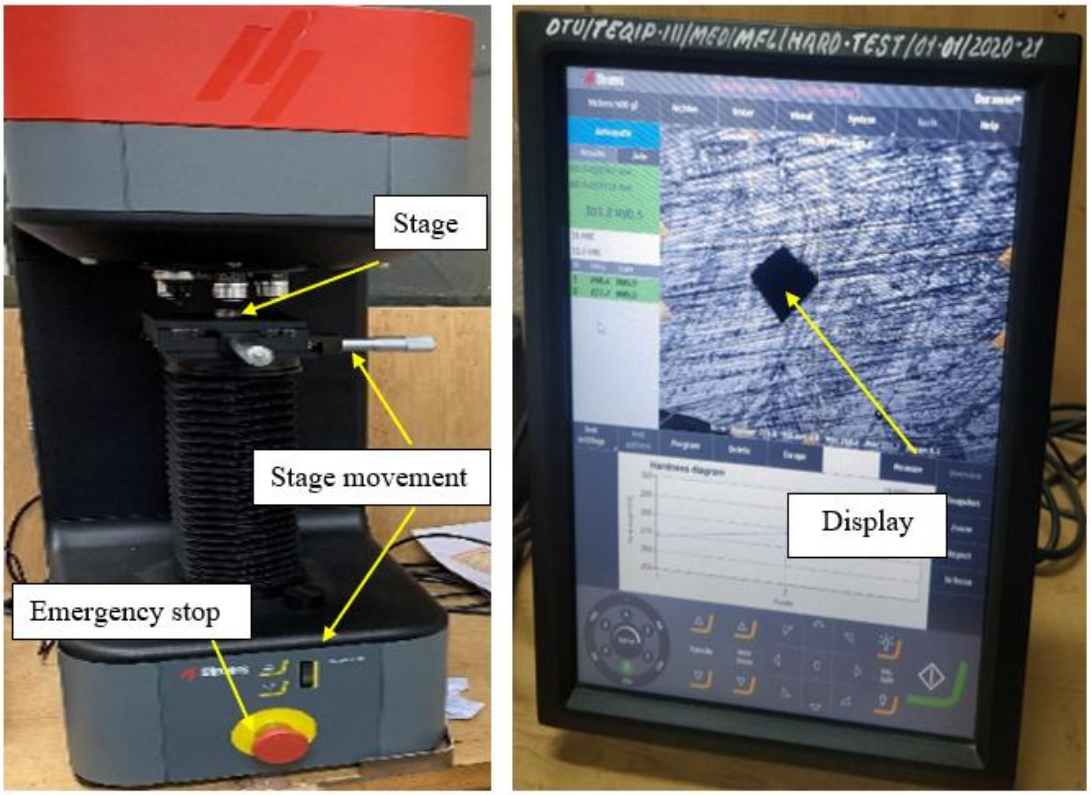

Fig. 3.4 (Struers Duramin-40) Microhardness testing machine

The technical specifications of the Struers Duramin-40 are provided in Table 3.7.

Table 3.7 Microhardness testing machine specifications

Model	Duramin-40 M1
Load Range (Main Loads)	10 gf-10kgf
Vickers Capability	Yes
Knoop Capability	Yes
Brinell Capability	Yes
Stages and Turrets	
XY-Stage	Manual
XY Stage or anvil size (mm)	90×90
XY Stage stroke, max (mm)	25×25
Vertical capacity	172
Throat depth (mm)	170
Motorized Z-axis	Yes
Motorized turret	Yes
Turret positions	6
Anti-collision protection	Yes
Machine weight	101 Kg
Evaluation camera resolution	18 MP
Auto illumination	Yes
Laser or LED guider	Yes
Operation	Embedded Windows 10PC with 15-inch touch screen
Communication Port	HDMI, VGA, RJ45, WLAN, USB, RS232

It is a method employed to ascertain the hardness or ability to resist the penetration of the material being examined. It is conducted on samples that are either very thin or small, or on specific small sections within a cladded sample that require measurement. The microhardness study is conducted using a Struers Duramin-40, as depicted in Fig. 3.4. During the microhardness test, a Vickers diamond indenter is applied to the material's surface using a penetrator and a light weight of 500 grams. When a force is exerted on a material, it creates an indentation that results in permanent deformation at the surface of the substance. Using a square-shaped diamond indenter, the pressure is monitored for a predetermined period of time (10 seconds of dwell time) in a controlled environment. The Vickers hardness value is determined by measuring and calculating the diagonal resulting from the indentation made on the surface of the material, using a specified formula.

3.3.4 Optical Microscope

The GX41 inverted metallographic microscope is ideal for quickly and accurately analyzing specimens and assessing if metallurgical qualities meet production standards. The tiny and lightweight form of the device enables easy portability. This device stands out for its mobility and ergonomics, as well as its ergonomic eyepoint adjustment. Additionally, it offers great image quality and resolution, thanks to its brightfield and polarized illumination. Having a small and efficient body allows for increased mobility and improved ergonomics. The compact body of this device may be easily installed in a limited area and is also portable, making it suitable for both laboratory use and on-site inspection in manufacturing settings. The GX41 is equipped with a tilting binocular observation tube that allows the user to adjust the eyepoint ergonomically. This feature enables you to comfortably utilize the GX41 while

either standing or seated, creating a pleasant working environment. The use of brightfield and polarized illumination ensures exceptional image quality and outstanding resolution, resulting in vivid and well-defined observations at all levels of magnification. This is a result of the utilization of infinity-corrected UIS2 optics, which enable the viewing of high-clarity pictures that completely occupy the field of view (F.N.22). The objective magnifications for both clear polarizing and bright-field observations vary from 5x to 100x.

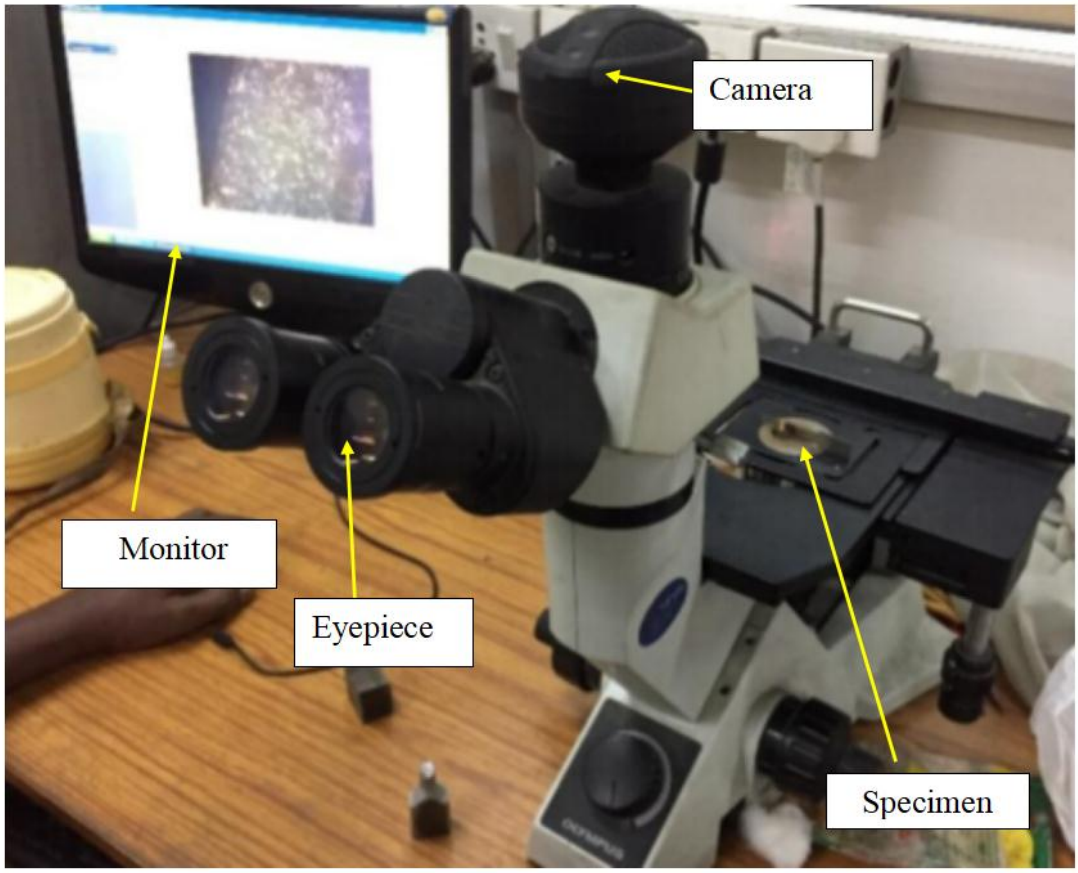

Fig. 3.5 Olympus GX41 compact inverted metallurgical microscope

The optical microscopy is conducted using the Olympus GX41 small inverted metallurgical microscope, as depicted in Fig. 3.5. The technical specifications of this microscope are provided in Table 3.8.

Table 3.8 Optical Microscope specifications (Make: Olympus GX41)

Optical System		UIS2 Optical System (Infinity-corrected)	
Microscope Frame	Observation Method		BF/KPO
	Reflected /Transmitted		Reflected
	Illumination System	Reflected light	30W Halogen or Fiber Light Guide (Light Source :100 W)
	Focus	Motorized/Manual	Manual Revolving Nosepiece Up/Down Movement (Stage Stationary Type)
		Stroke	9 mm
		Resolution/Fine adjustment sensitivity	Fine Stroke per Rotation 0.2 mm
	Revolving Nosepiece	Manual type	Quadruple for BF
Stage	Stroke		120(X)×78(Y) mm
Observation Tube	Standard Field (Field no. 18)	Inverted Image	Tilting Binocular Observation Tube
	Standard Field (Field no. 20)	Inverted Image	Binocular/Trinocular/Tilting Binocular Observation Tube
	Wide Field (Field no. 22)	Inverted Image	Binocular/Trinocular/Tilting Binocular Observation Tube
Dimensions			236(W)×624(D)×407(H) mm
Weight			10 Kg

3.3.5 Field Emission Scanning Electron Microscope

Field emission refers to the emission of electrons from a material's surface due to the application of a strong electric field. Scanning electron microscopy (FESEM) is performed

using an electron-optical column, as depicted in Fig. 3.6. The technical specifications of FESEM are provided in Table 3.9. The electron beam used to capture the image should be minimized, often to a size of approximately 10 nm. The resolution of the picture is affected by the electron probe size acquired through the FESEM procedure.

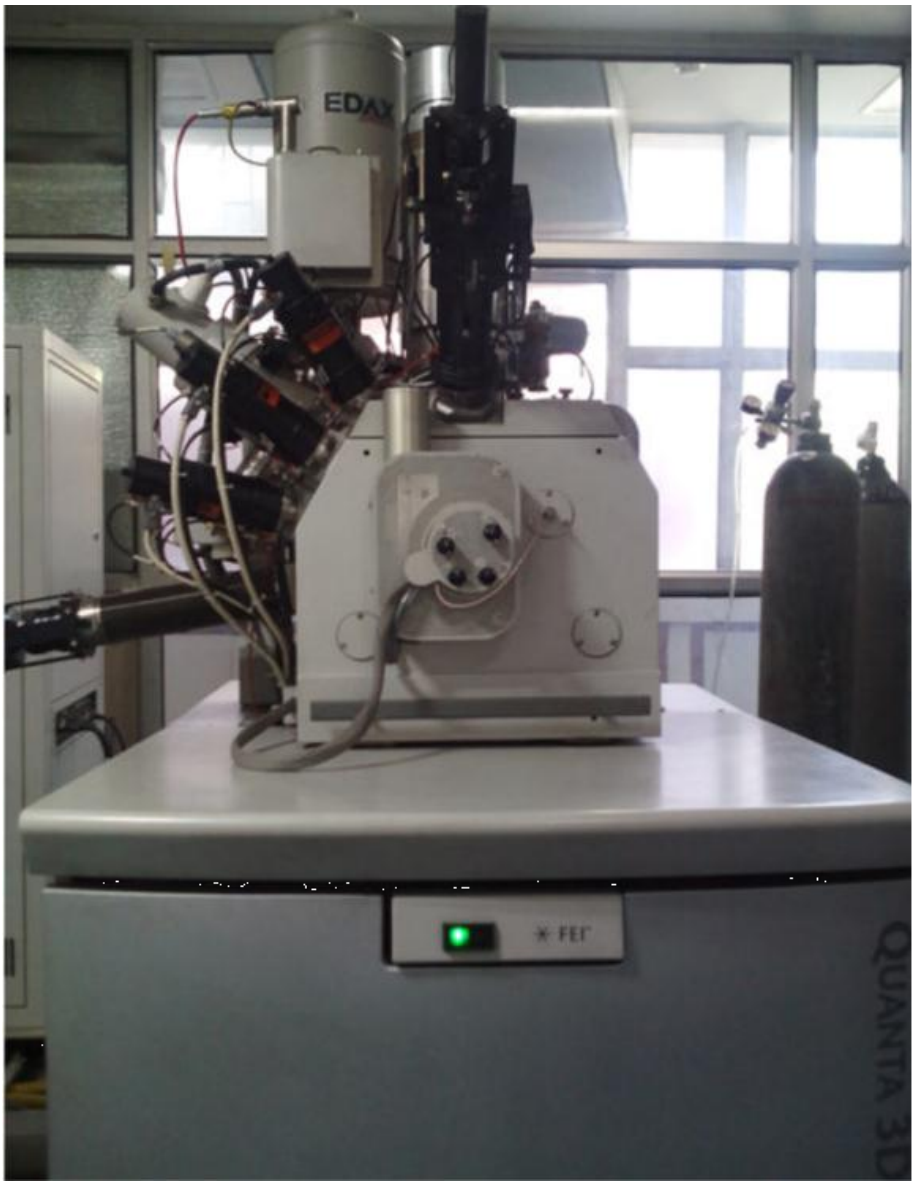

Fig. 3.6 Scanning Electron Microscope with Field Emission Gun (FEG-SEM) (Model: FEI QUANTA 3D FEG)

Table 3.9 FESEM specification

Electron Optics	High-resolution FESEM column optimized for high brightness/high current
Ion Optics	Magnum ion column with Ga liquid metal ion source with a lifetime of 1500 hours
Electron beam resolution	-1.2 nm @ 30 kV @ high vacuum mode -1.5 nm @ 30 kV @ ESEM mode -1.5 nm @ 3 kV @ low vacuum mode
Ion beam resolution	10 nm @ 30 kV @ 1pA
Accelerating Voltage	200 V to 30 kV for electron beam imaging and 5 to 30 kV for ion beam imaging
Detectors	Everhardt-Thornley SED, Low-vacuum SED, Gaseous SED, IR-CCD, EDS detectors and Gaseous BSED
Specimen stage	4-axis motorized eccentric goniometer stage X=50 mm, Y=50 mm, T=-5+75° (manual), Z=50 mm (25 mm motorized), rotation =360° continuous

Raster scanning is the term used to describe the procedure in which the electron probe covers the entire specimen. During the scanning process, high-energy electrons are sent towards the specimen, causing them to scatter upon interaction. The scattering behavior is observed in electron interactions, manifesting as both elastic and inelastic processes.

The resulting image from the scanning process may exhibit varying levels of brightness in reaction to the electron bombardment. The varying brightness is attributed to the presence of secondary electrons and backscattered electrons, which can be distinguished based on its kinetic energy, with the latter possessing more energy. The images produced with the secondary electron reveal solely the surface morphology, providing no information about the underlying structure. Only topographical differences are observed. On the contrary, backscattered electron pictures possess depth, revealing information about the underlying structure of the material. This information is derived from signals originating from half of the depth of penetration. They exhibit contrasting pictures based on the chemical makeup of the item. [Egerton, (2005)].

3.3.6 X-Ray Diffraction

Diffraction patterns occur when light is scattered by a regularly arranged structure with a high degree of order, resulting in constructive interference. Constructive interference is only noticed at certain angles. The goal of the XRD data analysis is to find patterns that match the crystal structure's orientation. The Miller indices of the peaks in the diffraction pattern are analysed in order to investigate this further. The wavelength employed for X-ray radiation and the interatomic spacing are nearly identical. When X-rays encounter atoms, they scatter and create a diffraction pattern. The advance machine (Bruker D8) is utilized for XRD spectrum analysis, as depicted in Fig. 3.7. The technical specifications of this machine can be found in Table 3.10.

The diffraction peaks recorded on the XRD correspond to the atomic planes. The diffraction peaks that are created are directly correlated to the atomic planes, providing

valuable information for the analysis of both the microstructure and atomic structure. The position of the peak's diffraction is determined using Bragg's equation, which states that $n\lambda = 2dhklSin\theta$. The term "dhkl" refers to the interplanar spacing between the crystal planes of an atom that are parallel to each other. θ represents the angle formed between the incident beam and lattice normal at the reflection point. λ represents the wavelength, whereas n represents the order of reflection, which is an integer. Bragg's law aids in determining the angle of peaks diffraction occur as a result of the constructive interference caused by X-rays scattered off the atom's crystal planes.

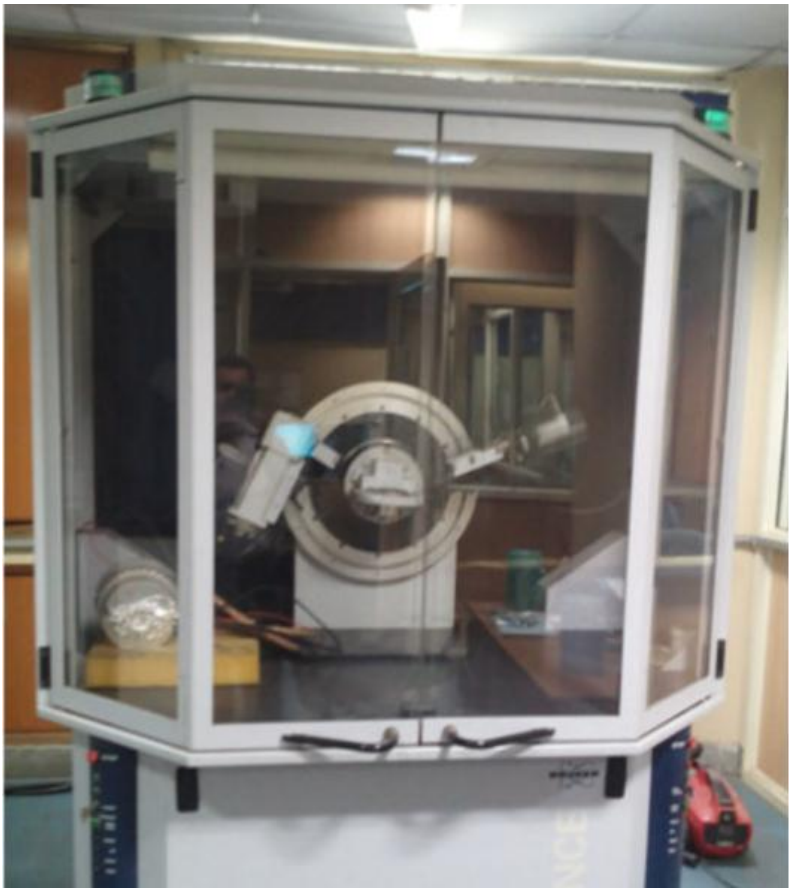

Fig. 3.7 (Model: BRUKER D8 ADVANCED) X-Ray diffraction

Table 3.10 Specification of XRD machine

Source	2.2 kW Cu anode long fine focus ceramic X-ray tube
Running Condition	40 kV and 40 mA
Beam [Cu-$K_{\acute{a}1}$]	Collimated, compressed and frequency filtered by a Gobel mirror and V-Groove
Collimated beam dimensions	0.3 mm by 11 mm
Gobel mirror	60 mm multilayer X-ray mirror on a high on a high precision parabolic surface
Maximum and minimum measurement circle diameter (Goniometer)	250 mm and 100 mm
Smallest angular step size	0.0001°
Reproducibility	+/-0.0001°
Maximum rotational speed	1500°/min
Angular range (Theta)	-5° to 40°
Angular range (2Theta)	-10° to 60°
Sample Size	200 mm in diameter and 50 mm thick
Maximum count rate	2×10^6 s^{-1} (although it should not be exposed to in excess of 5×10^5 s^{-1} for periods longer than about 1 second)
Detector electronics count rate	3×10^7 s^{-1}

3.3.7 Residual Stress Measuring Machine

The High-Resolution X-Ray Diffractometer (HR-XRD) - Pulstec μ-X360n model, capable of advanced 2D analysis is utilized to measure residual stresses at different locations of the weldment, as depicted in Fig. 3.8. The technical specifications of this machine may be found in Table 3.11. The μ-X360n Pulstec High-Resolution Full 2D X-ray Diffraction (HR-XRD) equipment was used to assess the residual stresses of the welded joints in different areas. The device specification includes a conventional Cr x-ray tube with a collimator size of 1 mm, operating at 30 kV and 1 mA. This apparatus operates based on the Cosa method, which involves capturing a complete Debye-Scherrer ring to record the entirety of diffraction using a two-dimensional detector. The specification includes conventional Cr (x-ray) tube with a a current of 1 mA and voltage of 30 kV. The collimator size is φ 1 mm, and the measurement conditions are also provided. The method is based on the Cosα technique, which captures a complete Debye-Scherrer ring. This ring provides information about grain orientation (texture) and grain coarsening, among other things. The ring is obtained with a single, brief exposure to x-rays using a two-dimensional detector. The method is expedited as it eliminates the need for sample tilts at various angles, unlike the conventional sin2ψ technique. This approach involves exposing the material to x-rays, with a penetration depth of up to 1 μm, in order to detect the fundamental atomic plane spacing and any changes in spacing caused by processing. The lattice spacing is determined by measuring the Debye ring using a 2D detector in a single measurement.

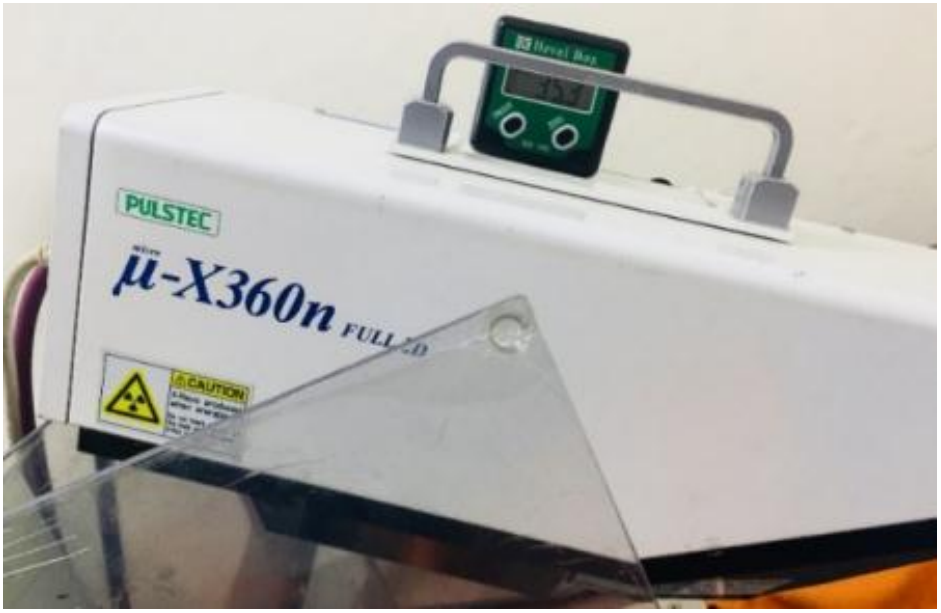

Fig. 3.8 High-Resolution X-ray Diffraction (HR-XRD) machine

Table 3.11 Residual stress machine specifications

X-ray tube	30 kV and 1mA (Safety and Ecology)
Collimator size	φ 1 mm (φ 0.04 inch)
X-ray detector	Full 2 D (visual analysis)
Precision mech.	Not necessary
2D Full data of Debye-Scherrer ring	Max. 500 points
Cos ά line data	Max. 125 points
Permissible range	± mm (easy setting)
Measurement time	90 sec.
Portable	Air cooling, Goniometer not required
Sensor unit weight	4 kg (8.8 lbs) (Z height stage)
Power supply unit weight	6 kg (13.2 lbs)

3.4 OPTIMIZATION OF CMT CLADDING PROCESS PARAMETERS

3.4.1 Process Parameters

Welding Current: In GMAW/CMT welding, the generation of heat input mainly depends upon the welding current. The welding current influences the size of weld width, dilution, and depth of penetration as a result of the good microstructural and mechanical properties of clad beads. The selection of the welding current value is determined by the thickness of the base material. Appropriate welding current is required for fabricating sound cladding with low dilution.

Welding speed: welding speed is a vital welding parameter for generating heat input during welding. Higher welding speeds produce lower heat input as a result of improper penetration. Too much lower welding speed creates high heat input, which may result in excess melting of the base material, which results in high dilution. The welding speed is the total time the welding torch takes to complete the welding.

Nozzle to work distance (NTD): The distance between the base material and the filler wire tip is the NTD. An increase or decrease in the NTD value affects the welding current. A suitable NTD should be maintained for better results.

Voltage: The arc voltage is directly proportional to the heat input. In this work, welding current is taken as an independent welding parameter, and the voltage depends upon the welding current. When changing the welding current, the machine automatically adjusts the voltage value.

Gas flow rate: shielding gas protects the molten weld pool from the formation of ill effects from harmful atmospheric gases such as hydrogen, nitrogen, oxygen, etc. Gas flow rate

influences the quality of weld bead and penetration. In this work, constant gas flow is maintained.

Pulse Dynamic Correction Factor: This parameter dispenses the droplet detachment at a slower rate or uniform energy level from the filler wire. The direct current is affected and the mean current is regulated by the pulse dynamic correction factor. [G.P. et al., 2019]. There are three arc correction factor levels: -10, 0, and +10. When the detachment of droplet force is required for the lower side (-10), no increase or decrease in the separation of droplet force (0) for the higher side (-10) is fixed in the machine.

Wire feed rate: The wire feed rate refers to the velocity at which filler wire is supplied to the weld bead. The wire feed rate directly affects the formation of weld width, HAZ, and intermetallic layer thickness.

3.4.2 Response Surface Methodology

Response surface methodology (RSM) is primarily employed to model and analyze the impact of multiple independent variables on a dependent variable, with the goal of response optimization [Montgomery, (2017)]. The Central Composite Design (CCD) is employed to determine the importance of the model for the Design of Experiments (DOE). CCD under RSM is implemented by applying the software Design Expert (DE).

The response surface study examines how the independent variables, denoted as x1, x2....xn, impact a dependent variable Y or response. The objective is to maximize the response. The bead shape and physical characteristics of bead-on-plate and CMT cladding are influenced by several factors, including the travel speed (mm/sec), shielding gas flow rate (L/min), current (A), NTD, filler wire material etc.

Three independent factors, namely current, welding speed, and Nozzle to work piece distance (NTD) are selected for super duplex cladding using CMT. The response function is expressed by equation 3.1.

$$Y = \varphi (A, B, C) \quad (3.1)$$

The equation's variables are defined as follows: Y is the outcome, φ is the response function, and A, B, and C symbolize the input variables: current, welding speed, and NTD, respectively. The relationship between the responses and independent variables is modeled using a quadratic equation 3.1, which combines these variables and their interactions. The equation includes: Y: the response; bo: the constant term; b1, b2, and b3: coefficients for linear effects; b12, b23, and b31: coefficients for interaction effects; b11, b22, and b33: coefficients for quadratic effects; and x1, x2, and x3: coded levels for current (A), welding speed (B), and NTD (C). This equation establishes a mathematical relationship between the input variables and the response, accounting for both linear and nonlinear effects. Selected welding parameters and their levels are shown in Table 3.12. The design matrix for the CMT weld bead of Super duplex 2507 stainless steel is displayed in Table 3.13.

Table 3.12 Welding parameters and levels

Welding process parameters	**Units**	**Levels**		
Welding Current	A	160	180	200
Welding Speed	mm/sec	3	4	5
NTD	mm	10	12	14

3.5 EXPERIMENTAL PROCEDURE

3.5.1 Super Duplex 2507 SS Cladding over low carbon steel plate

Table 3.13 DOE for CMT weld bead of Super duplex 2507 stainless steel.

		Factor 1	Factor 2	Factor 3
Std	Run	Current	Welding Speed	NTD
		A	mm/sec	mm
11	1	180	3	12
9	2	160	4	12
8	3	200	5	14
13	4	180	4	10
1	5	160	3	10
16	6	180	4	12
15	7	180	4	12
12	8	180	5	12
19	9	180	4	12
3	10	160	5	10
14	11	180	4	14
2	12	200	3	10
20	13	180	4	12
4	14	200	5	10
18	15	180	4	12

Continued on page no. 90

10	16	200	4	12
5	17	160	3	14
6	18	200	3	14
17	19	180	4	12
7	20	160	5	14

The design of experiments is given in Table 3.13. The weld on bead samples are shown in Fig. 3.9. A Super duplex 2507 filler wire diameter of 1.2 mm and an IS 2062 low carbon steel base plate of dimensions 100mm × 50mm × 5mm were chosen for weld-on-bead. A CMT welding machine (TPS400i) was used to perform the experiments. Shielding gas of argon (99.99%) with a flow rate of 15 LPM. Preliminary weld trial runs were conducted to fix the welding parameters. The samples were cleansed using a steel wire brush and acetone to eliminate the oxide coating and any other undesirable contaminants from the welded surface.

Fig.3.9 Super duplex 2507 weld on bead samples

3.5.2 Comparative study of CMT and Pulse MIG weld on bead

IS 2062 low carbon steel base plate of dimensions 100mm × 50mm × 5mm and an ER308L filler wire diameter of 1.2 mm were chosen for weld-on-bead. A CMT welding machine

(TPS400i) was used to perform the CMT and Pulse MIG welding experiments. Shielding gas of argon (99.99%) with a flow rate of 15 LPM and a nozzle-to--piece distance of 10 mm was fixed for all experiments. Preliminary weld trial runs were conducted to fix the welding parameters. Fig. 3.10 shows weld bead trails performed at different welding currents, and Fig. 3.11 shows the CMT macro images of the weld bead at current (a) 75A, (b) 100A, (c) 125A, (d) 150A, (e) 175A, and (f) 200A. Improper weld penetration and a lack of fusion were observed at lower currents than in the 175 A samples and at higher current (200A) melting of more metal occurs. Experiments were conducted at different welding speeds, ranging from 3 mm/sec to 6 mm/sec, at intervals of 1 mm/sec with a constant 175 A welding current using the CMT and pulse MIG welding processes.

Table 3.14 Welding parameters of Pulse MIG and CMT weld bead samples

S.No.	Welding Current (A)	Welding Speed (mm/sec)
1.	175	3
2.	175	4
3.	175	5
4.	175	6

Fig. 3.10 CMT weld beads trails performed at different welding current

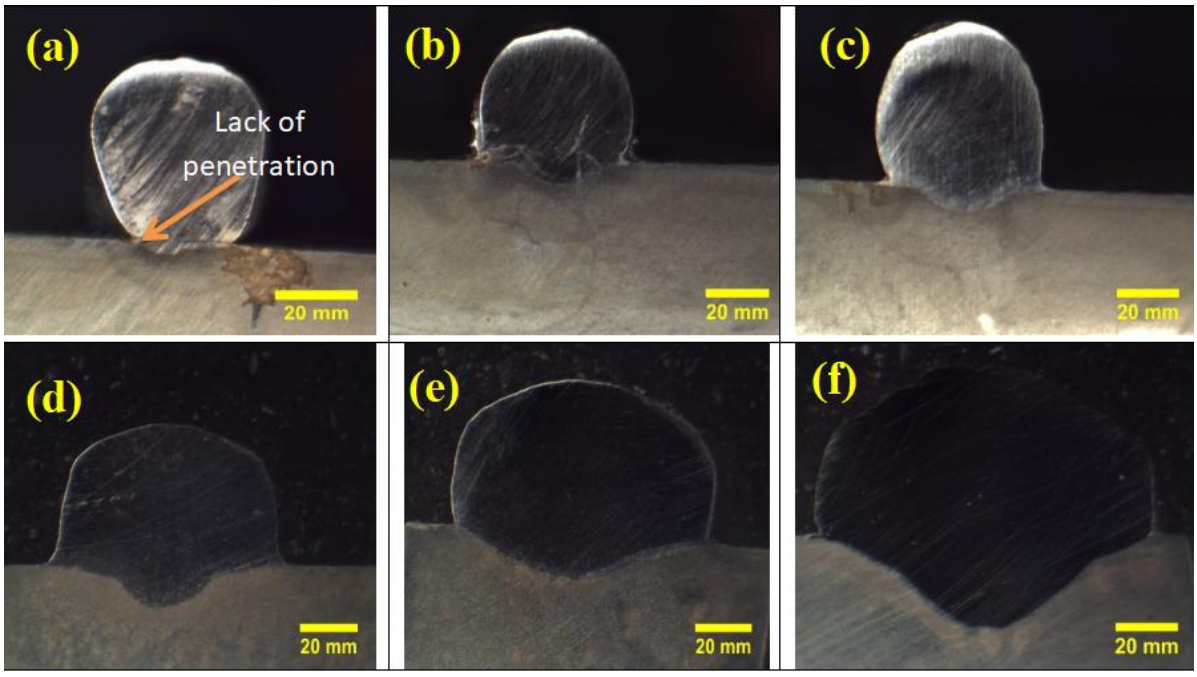

Fig. 3.11 Macro image of CMT weld bead at current (a) 75A (b)100 A(c) 125 A(d)150 A (e) 175A (f) 200A

The selected process parameters for different samples are exhibited in Table 3.14. The dependent parameters in CMT and MIG P are current, voltage, and wire feed rate (WFR). Modifying the value of the first parameter leads to changes in the other due to synergistic relationships. The selection of the current and welding speed for studies is based on the significant influence they have on the geometry of the bead, as indicated by the literature survey and numerous experimental trials.

3.5.3 Wear Study

ER 308L filler wire (1.2 mm diameter) is chosen to perform cladding over the low-carbon steel base material. The CMT (TPS400i) welding machine experimental setup, as shown in Fig. 3.12 (a), was used to generate the cladding surface over the base plate. Fig. 3.12 (b)

shows the 308L SS cladding on a low-carbon steel plate and the specimen extracted from the cladding surface, and Fig. 3.12 (c) shows the cross-section of the clad sample extracted at different welding speeds to examine the effect of welding speed on clad surface characteristics and its wear behavior. Wear tests were conducted on the ball on the disc reciprocating tribometer (DUCOM) as per the ASTM G133-05 standard. Various parameters, such as load, frequency (sliding velocity), stroke, and sliding distance, affect the wear properties. The load and frequency parameters are selected for wear studies based on the literature review and number of trial runs. In the wear test, the clad specimen was kept in contact with a 6mm-diameter tungsten ball undergoing linear reciprocating motion for 15 minutes by varying different loads (30N, 40N, and 50N) and frequencies (5Hz, 10Hz, and 15Hz) at a specific stroke length of 10 mm in unlubricated wear conditions. The various process parameters taken for the wear test are shown in Table 3.15. Before the wear test, the specimens were grounded on a 1500-grade emery sheet and cleaned with acetone. Before and after the wear test, the wear samples were weighed. FESEM with EDS analysis was used to study the wear mechanisms. The wear surface and clad surface phase constitution were determined with an X-ray diffractometer (XRD).

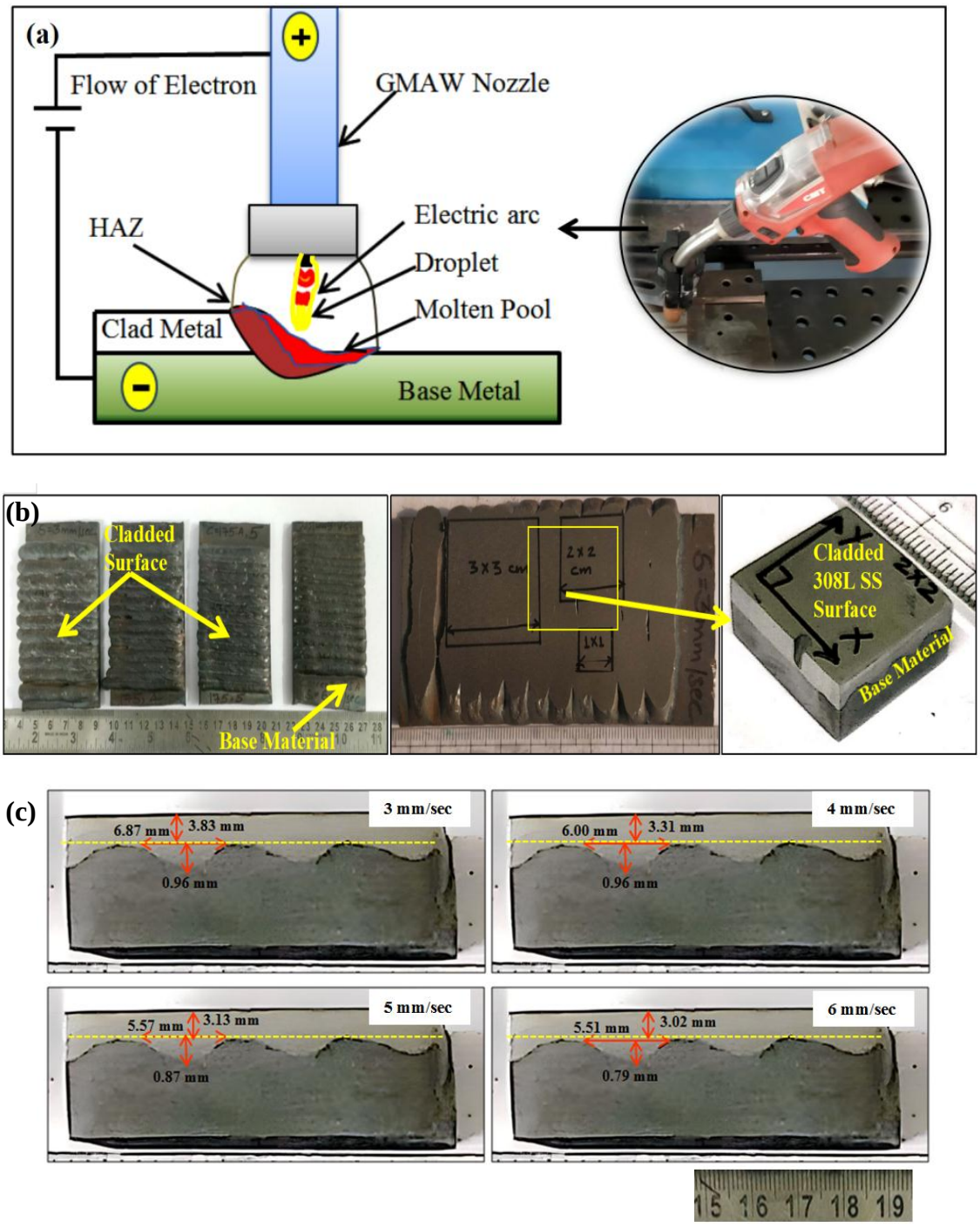

Fig.3.12 (a) CMT experimental setup (b) 308L SS cladding on low carbon steel plate and extracted sample for wear test (c) cross-section of clad sample extracted at different welding speeds

Table 3.15 Process parameters for wear test

Process parameters			
Welding Speed	3 mm/sec	4 mm/sec	5 mm/sec
Load	30 N	40 N	50 N
Frequency	5 Hz	10 Hz	15 Hz

3.6 SUMMARY

The selection of substrate and filler materials was covered in this chapter. Super Duplex 2507 and AISI 308L stainless steel were selected as the filler wires for cladding over low-carbon steel. Various characterizations of the substrate and filler materials were reported. The detailed description of the preparation of samples for various tests, including macrostructure and microstructural characterization, microhardness, wear, and residual tests. Various cladding, microstructural, and mechanical characterization equipment were discussed. The metallurgical characterization procedure, which involved analyzing the microstructure, phase analysis, and determining the elemental composition, was demonstrated using optical microscopy, FESEM, and X-ray diffraction (XRD). The preparation of all specimens followed the guidelines set by ASTM standards. Experimental methods for 308L bead-on-plate, wear test of cladded plates, and super duplex 2507 weld on bead over low carbon steel are explained briefly. Optimization for the super duplex 2507 weld bead-on-plate was carried out using CCFCD under RSM.

CHAPTER 4

RESULTS AND DISCUSSION

4.1 OPTIMIZATION OF CMT CLADDING PROCESS OF SUPER DUPLEX STAINLESS STEEL ON LOW CARBON STEEL

4.1.1 Introduction

The service life of the components used in chemical, petrochemical, paper, and pulp industries is shortened by a lack of wear resistance, which results in substantial financial and energy savings. Low-carbon steels are traditional materials that have the necessary strength to meet industrial demands, are inexpensive, and are comparatively simple to produce [Senthilkumar & Kannan, (2015)]. The stainless-steel material is replaced with low-carbon steel for wear-resistant applications. The microstructure of stainless steel is intimately related to its strength and other characteristics. 2507 SS have equal proportions of austenite and ferrite grains, which increase strength, resistance to pitting, and resistance to stress corrosion cracking compared to their austenitic alloy. Due to their high sensitivity to heat, these materials have a restricted operating temperature range between -100 °C and 300 °C to prevent ductility loss and the development of brittle phases. Due to strict processing restrictions implemented to avoid the loss of the desired qualities, the manufacture of bulk stainless-steel components is restricted [Sathirachinda et al., (2009); Tan et al., (2009)]. Cladding can be an alternative method to produce a thick layer of wear-resistant material, often stainless steel, deposited over a low-carbon steel substrate. Various

techniques can be used to create the claddings, including roll bonding, centric casting, welding, explosive cladding, etc. [Chen et al., (2019)]. Due to its capacity to work with prefabricated components and its ability to regulate heat input, welding is a favored cladding procedure. Mathematical models can be used to determine the relationship between the bead dimensions and the heat input. [T. Kannan & Yoganandh, (2010)]. The CMT technique is a modified version of MIG welding that explicitly uses low heat input and process control for the parent metal without sacrificing the strength of the metallurgical connection between the substrate and the coating. With increased welding speed, the penetration has increased due to higher base metal exposure below the arc with a comparatively smaller weld pool. [Gunaraj & Murugan, (1999)] reported that RSM can be utilized to analyze the effect of process factors on submerged arc welding of copper beads over mild steel plates. The weld penetration, reinforcement, width, and dilution % decreased with increased welding speed. [Shahi & Pandey, (2008)] compared GMAW and Universal GMAW cladding of 316L SS using the RSM technique to optimize the process parameters quantitatively. The dilution increases with increases in wire feed rate, open circuit voltage, and welding speed and decreases with increases in preheat current and nozzle-to-plate distance. The dilution obtained in the universal GMAW process is lower than that obtained in the GMAW process due to the external preheating of the filler wire, which increases the amount of arc energy contributed by resistive heating. [Shahi & Pandey, (2008)] reported that 316L CMT clad bead over mild steel has minimum dilution for a lower wire feed rate and lower welding speed. [Murugan & Parmar, (1997] produced 309L SS weld on bead over structural steel plate using the GMAW process and revealed a low

dilution level with crack-free claddings. [Kumar & Singh, (2012)] examined the cladding of 304L SS over low-carbon steel using the GMAW process and found that the minimum dilution percentage was obtained at the lower levels of current. [Kannan & Yoganandh, (2010)] performed the cladding of 308L SS over low carbon steel using the GMAW process and observed that with increasing wire feed rate and decreasing speed, the height of the weld bead and width increases. [Murugan & Parmar (1994)] investigated the 316 L SS cladding over low carbon steel using the GMAW process and discovered that bead width is significantly affected by the change in voltage. [Varghese et al., (2019)] studied the microstructure and volumetric dilution of Inconel 617M clad over 316L stainless steel using CMT and TIG processes at different currents. The CMT has less volumetric dilution and no HAZ when compared to the TIG. The overlay coatings displayed columnar dendritic microstructure with fine inter-dendritic precipitates. [Pant et al., (2019)] investigated 316L cladding over low-carbon steel using the LASER process and found that laser power and powder flow rate are mainly influencing the clad layer height. [Palani & Murugan, (2006)] discovered that when cladding 317L SS over mild steel plate with a flux-cored arc welding method, the penetration, bead width, and height increase as the welding current increases and decrease with increasing welding speed.

4.1.2 Recoding of responses

The weld beads fabricated at different process parameters and their macro images are shown in Fig. 4.1 and Fig. 4.2, respectively. The input welding parameters and their responses are presented in Table 4.1. The estimation of dilution percentage is given below (Mishra et al., 2023).

$$\text{Dilution (\%)} = \frac{A_P}{A_P + A_R} \quad (4.1)$$

AP and AR are the areas of penetration and reinforcement, respectively. The AP and AR were measured using Image J software. For every test, an average of three weld samples is taken.

Fig. 4.1 Weld bead images as per design matrix

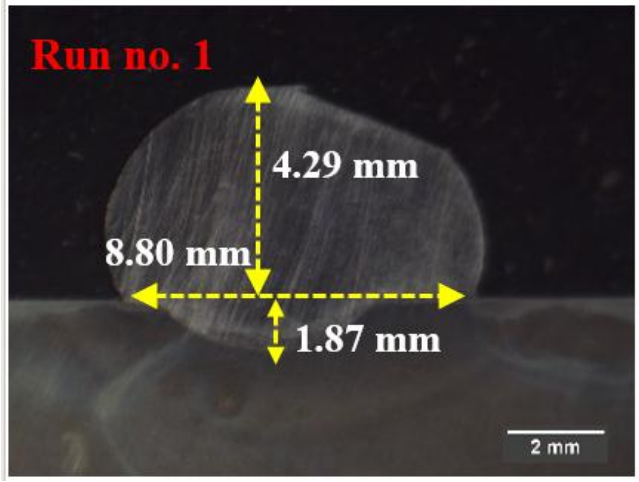
Run no. 1
4.29 mm
8.80 mm
1.87 mm
2 mm

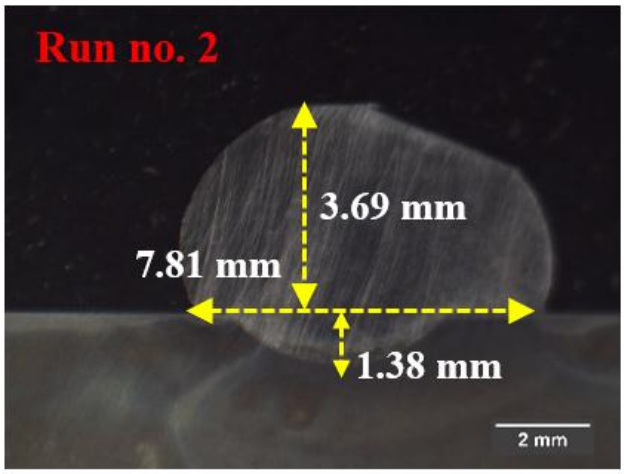
Run no. 2
3.69 mm
7.81 mm
1.38 mm
2 mm

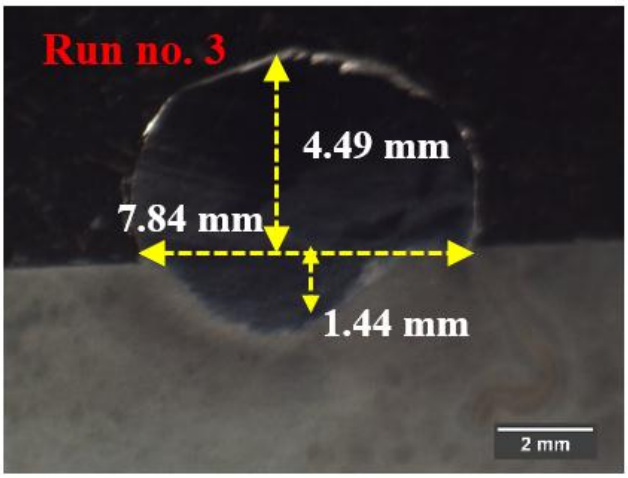
Run no. 3
4.49 mm
7.84 mm
1.44 mm
2 mm

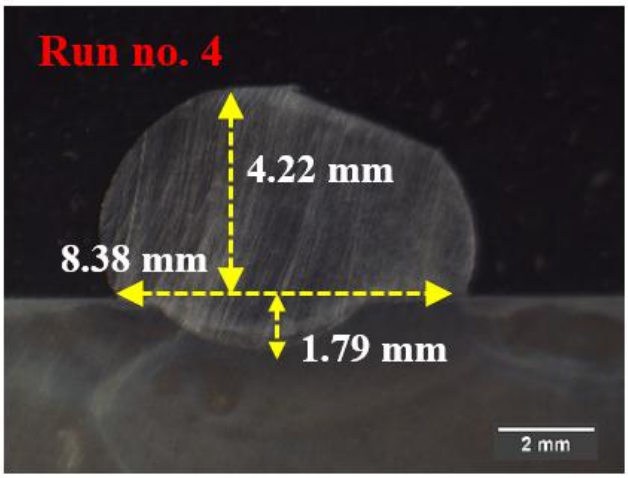
Run no. 4
4.22 mm
8.38 mm
1.79 mm
2 mm

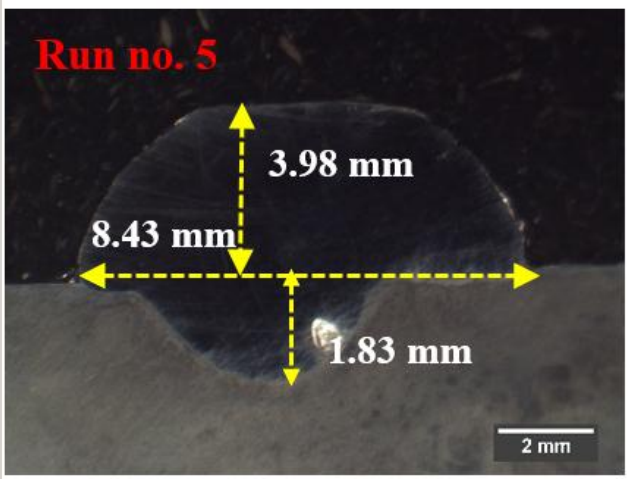
Run no. 5
3.98 mm
8.43 mm
1.83 mm
2 mm

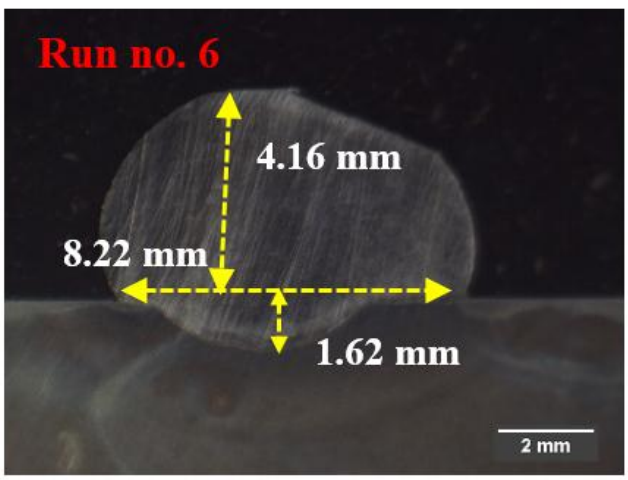
Run no. 6
4.16 mm
8.22 mm
1.62 mm
2 mm

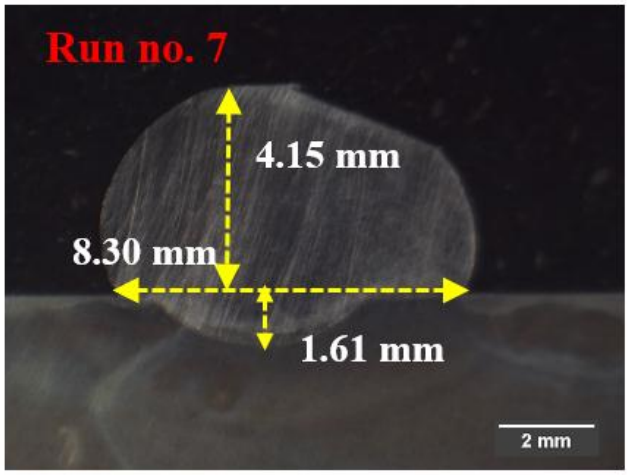
Run no. 7
4.15 mm
8.30 mm
1.61 mm
2 mm

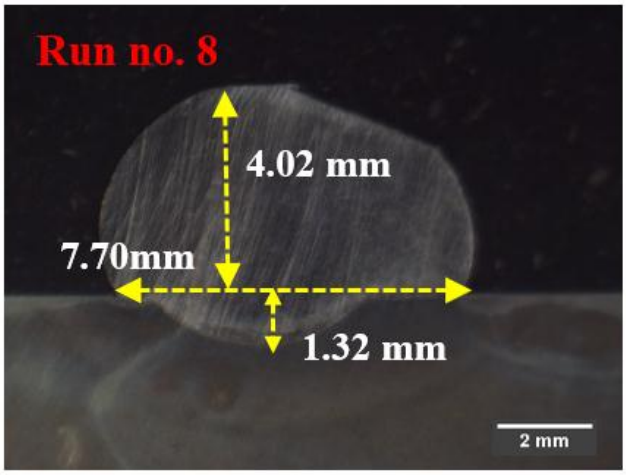
Run no. 8
4.02 mm
7.70mm
1.32 mm
2 mm

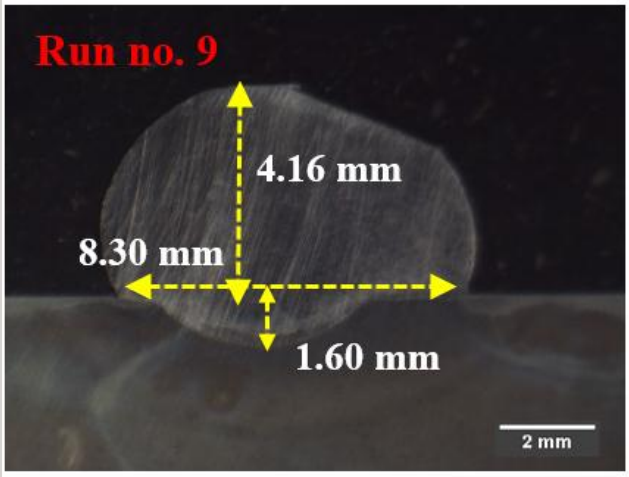
Run no. 9
4.16 mm
8.30 mm
1.60 mm
2 mm

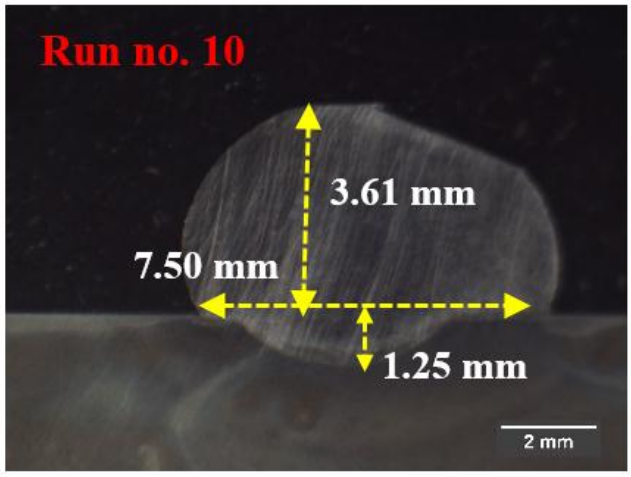
Run no. 10
3.61 mm
7.50 mm
1.25 mm
2 mm

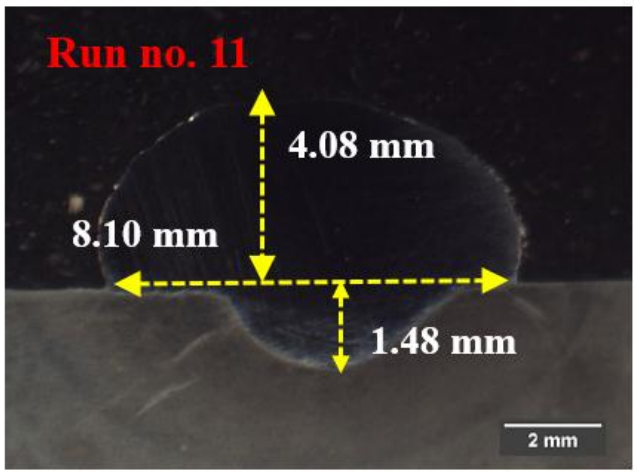
Run no. 11
4.08 mm
8.10 mm
1.48 mm
2 mm

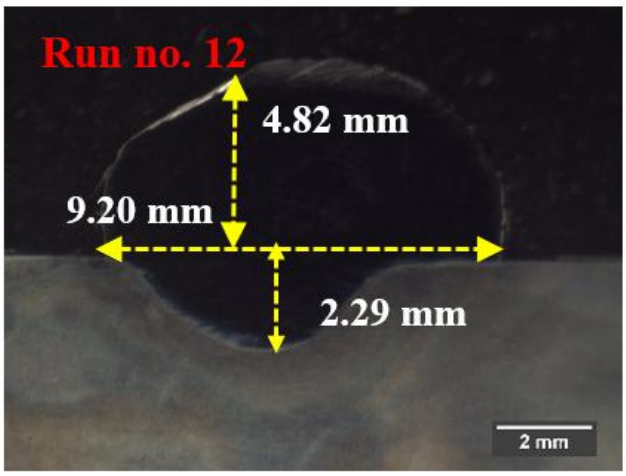
Run no. 12
4.82 mm
9.20 mm
2.29 mm
2 mm

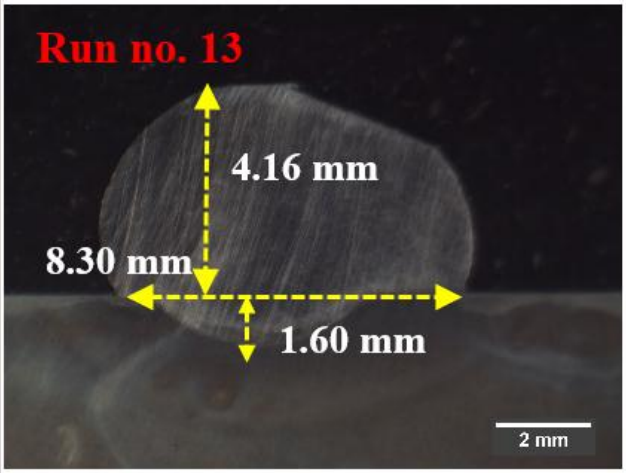
Run no. 13
4.16 mm
8.30 mm
1.60 mm
2 mm

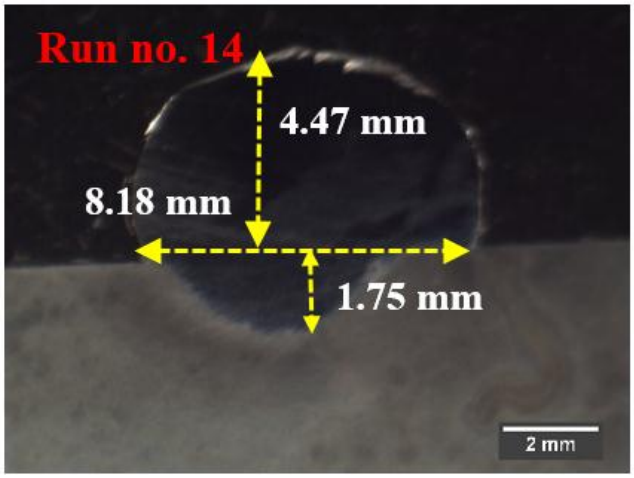
Run no. 14
4.47 mm
8.18 mm
1.75 mm
2 mm

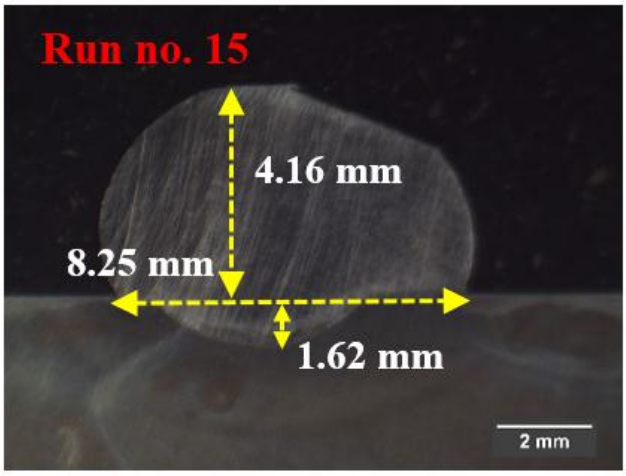
Run no. 15
4.16 mm
8.25 mm
1.62 mm
2 mm

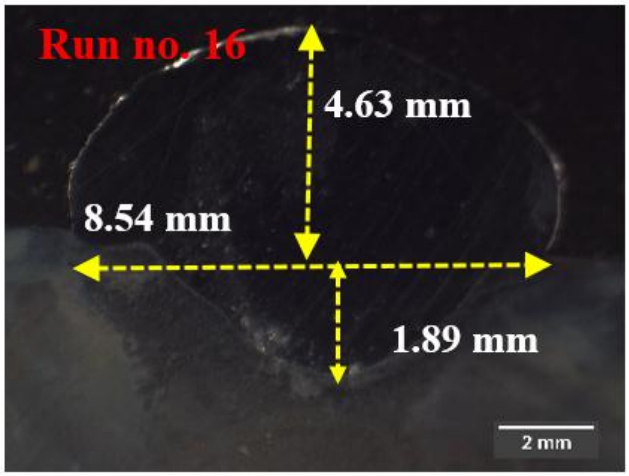
Run no. 16
4.63 mm
8.54 mm
1.89 mm
2 mm

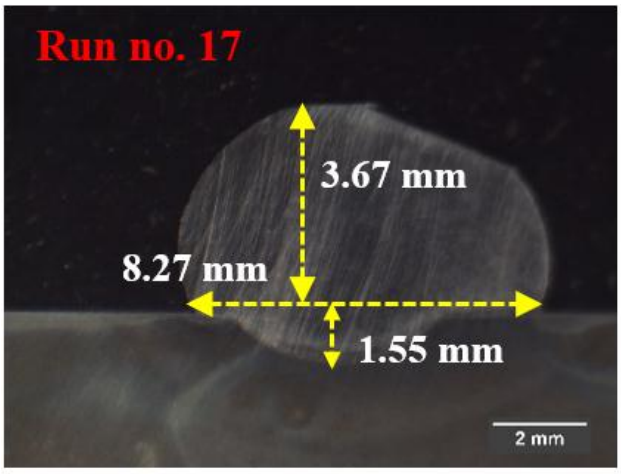
Run no. 17
3.67 mm
8.27 mm
1.55 mm
2 mm

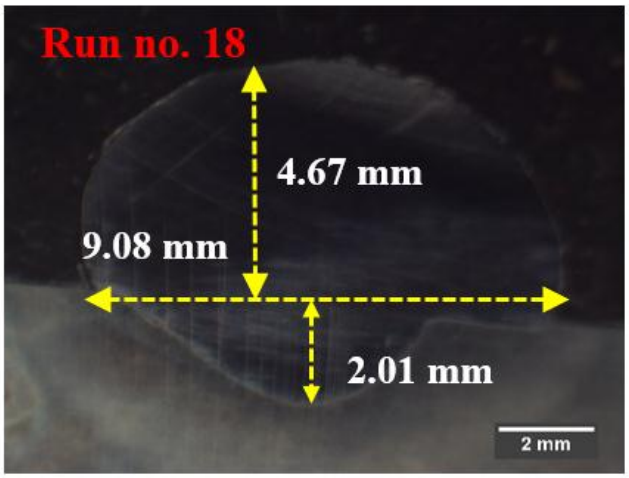
Run no. 18
4.67 mm
9.08 mm
2.01 mm
2 mm

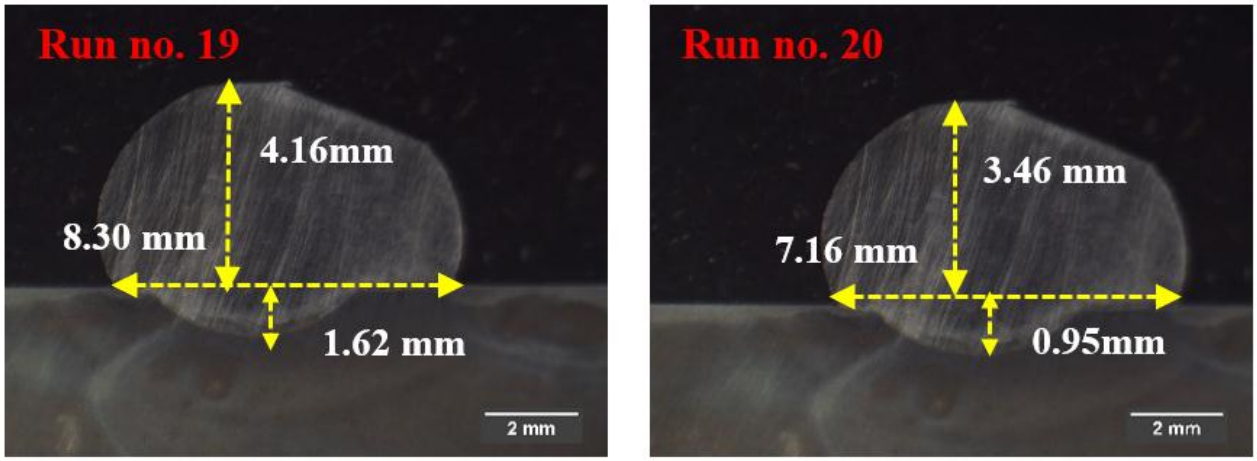

Fig. 4.2 Macro images of weld bead

Table. 4.1 Input welding parameters and experimental results with predicted values

R.No.	Welding current (A)	Welding speed (mm/sec)	NTD (mm)	Bead width (mm)		Bead Height (mm)		Penetration (mm)		Dilution%	
				Act.	Pred.	Act.	Pred.	Act.	Pred.	Act.	Pred.
1	180	3	12	8.80	8.81	4.29	4.29	1.87	1.88	18.91	18.83
2	160	4	12	7.81	7.83	3.69	3.69	1.38	1.39	15.35	15.34
3	200	5	14	7.84	7.83	4.49	4.49	1.44	1.44	13.81	13.81
4	180	4	10	8.38	8.39	4.22	4.22	1.79	1.78	17.80	17.73
5	160	3	10	8.43	8.43	3.98	3.97	1.83	1.82	19.73	19.75
6	180	4	12	8.22	8.26	4.16	4.16	1.62	1.62	16.15	16.06
7	180	4	12	8.30	8.26	4.15	4.16	1.61	1.62	16.00	16.06
8	180	5	12	7.70	7.73	4.02	4.02	1.32	1.31	13.77	13.76
9	180	4	12	8.30	8.26	4.16	4.16	1.60	1.62	16.00	16.06
10	160	5	10	7.50	7.50	3.61	3.61	1.25	1.25	15.00	14.99

Continued on page no. 105

11	180	4	14	8.10	8.14	4.08	4.08	1.48	1.49	14.90	14.87
12	200	3	10	9.20	9.21	4.82	4.82	2.29	2.29	21.47	21.50
13	180	4	12	8.30	8.26	4.16	4.16	1.60	1.62	16.00	16.06
14	200	5	10	8.18	8.17	4.47	4.47	1.75	1.75	16.75	16.77
15	180	4	12	8.25	8.26	4.16	4.16	1.64	1.62	16.00	16.06
16	200	4	12	8.54	8.56	4.63	4.63	1.89	1.88	17.41	17.32
17	160	3	14	8.27	8.27	3.67	3.67	1.55	1.54	17.00	17.00
18	200	3	14	9.08	9.07	4.67	4.68	2.01	2.01	19.14	19.17
19	180	4	12	8.30	8.26	4.16	4.16	1.62	1.62	16.00	16.06
20	160	5	14	7.16	7.14	3.46	3.47	0.95	0.946	11.60	11.59

4.1.3 Model equation

The Face-centred CCD-based models have been developed for bead width, height, Depth of penetration, and dilution. Design-Expert software is used to generate these models. The response function represents the weld geometry, expressed in Equation 4.2. The Φ denotes the responses. Equation 4.3 illustrates the responses and independent variables related to the second order's general polynomial Equation.

$$Y = \Phi (A, B, C) \quad (4.2)$$

A is the welding current, B is the welding speed, C is the NTD, and Y is the response.

$$\mathbf{Y}=b_0+b_1x_1+b_2x_2+b_3x_3+b_{11}x_1^2+ b_{22}x_2^2+b_{33}x_3^2+b_{12}x_1x_2+ b_{13}x_1x_3+b_{23}x_2x_3 \quad (4.3)$$

Where, Y is responses. Here, the intercept is b_0, the coefficient values for linear effects are b_1, b_2, and b_3, the coefficient values for interaction effects are b_{12} and b_{13}, the coefficient values for quadratic effects are b_{11}, b_{22}, and b_{33}, and the coded levels for independent variables (i.e.

x_1, x_2, and x_3). The values of the coefficients are controlled using Equation 4.3, and the multi-response mathematical model for responses is presented in Equation 4.4 to 4.7 in terms of coded variables. The high levels of the factors are coded as +1, and the low levels are coded as -1. The coded equation helps identify the relative impact of the factors by comparing the factor coefficients.

Bead Width = +8.26 + 0.3670*A - 0.5400*B - 0.1240*C - 0.0275*AB + 0.0050*AC - 0.0050*BC - 0.0671*A^2 + 0.0079*B^2 - 0.0021*C^2 (4.4)

Bead Height = +4.16 + 0.4673*A - 0.1367*B - 0.0721*C + 0.0040*AB + 0.0408*AC + 0.0398*BC + 0.0042*A^2 - 0.0028*B^2 - 0.0108*C^2 (4.5)

Depth of penetration = +1.62 + 0.2412*A - 0.2846*B – 0.1480*C + 0.0080*AB - 0.0015*AC - 0.0065*BC + 0.0195*A^2 - 0.0215*B^2 + 0.0195*C^2 (4.6)

Dilution % = +16.06 + 0.9900*A – 2.53*B – 1.43*C + 0.0100*AB – 0.1075*AC - 0.1600*BC + 0.2795*A^2 + 0.2395*B^2 + 0.2495*C^2 (4.7)

4.1.4 Analysis of variance (ANOVA)

ANOVA is used to check the adequacy of the developed model with 95% confidence level. The ANOVA results for bead width, bead height, Depth of penetration and dilution % are exhibited in Table 4.2

Table 4.2 ANOVA test results for various responses

(a) Bead Width

Source	SS	DOF	Mean Square	F-value	p-value	Contri. %	
Model	4.46	9	0.4959	418.86	< 0.0001	99.55	**Significant**
A-Current	1.35	1	1.35	1137.58	< 0.0001	30.13	
B-Welding Speed	2.92	1	2.92	2462.85	< 0.0001	65.17	
C-NTD	0.1538	1	0.1538	129.87	< 0.0001	3.43	
AB	0.0061	1	0.0061	5.11	0.0473	0.136	
AC	0.0002	1	0.0002	0.1689	0.6897	0.004	
BC	0.0200	1	0.0200	16.89	0.0021	0.44	
A^2	0.0124	1	0.0124	10.45	0.0090	0.26	
B^2	0.0002	1	0.0002	0.1453	0.7111	0.004	
C^2	0.0000	1	0.0000	0.0102	0.9217	0	
Residual	0.0118	10	0.0012			0.26	
Lack of Fit	0.0053	5	0.0011	0.8040	0.5917		**not significant**
Pure	0.0066	5	0.0013				

Continued on page no. 108

Error							
Cor Total	4.48	19					
Std. Dev.	0.0344	**R^2**		0.9974			
Mean	8.23	**Adjusted R^2**		0.9950			
C.V. %	0.4180	**Predicted R^2**		0.9916			
		Adeq. Precision		84.7479			

(b) Bead Height

Source	**SS**	**DOF**	**Mean Square**	**F-value**	**p-value**	**Contri. %**	
Model	2.45	9	0.2721	32729.02	< 0.0001	99.94	**Significant**
A-Current	2.18	1	2.18	2.626E+05	< 0.0001	88.97	
B-Welding Speed	0.1869	1	0.1869	22474.94	< 0.0001	7.62	
C-NTD	0.0520	1	0.0520	6252.19	< 0.0001	2.12	
AB	0.0001	1	0.0001	15.39	0.0028	0.004	
AC	0.0133	1	0.0133	1597.74	< 0.0001	0.54	
BC	0.0126	1	0.0126	1520.29	< 0.0001	0.51	
A^2	0.0000	1	0.0000	5.91	0.0354	0	

Continued on page no. 109

B^2	0.0000	1	0.0000	2.54	0.1419	0	
C^2	0.0003	1	0.0003	38.38	0.0001	0.012	
Residual	0.0001	10	8.315E-06			0.004	
Lack of Fit	0.0000	5	2.762E-06	0.1992	0.9494		**not significant**
Pure Error	0.0001	5	0.0000				
Cor Total	2.45	19					
Std. Dev.	0.0029	**R^2**		1.0000			
Mean	4.15	**Adjusted R^2**		0.9999			
C.V. %	0.0694	**Predicted R^2**		0.9999			
		Adeq. Precision		663.1880			

(c) Depth of penetration

Source	**SS**	**DOF**	**Mean Square**	**F-value**	**p-value**	**Contri. %**	
Model	1.62	9	0.1794	1084.29	< 0.0001	99.99	**Significant**
A-Current	0.5818	1	0.5818	3515.29	< 0.0001	35.91	
B-	0.8100	1	0.8100	4894.14	< 0.0001	50	

Continued on page no. 110

Welding Speed							
C-NTD	0.2190	1	0.2190	1323.52	< 0.0001	13.51	
AB	0.0005	1	0.0005	3.09	0.1091	0.030	
AC	0.0000	1	0.0000	0.1088	0.7484	0	
BC	0.0003	1	0.0003	2.04	0.1835	0.018	
A^2	0.0011	1	0.0011	6.35	0.0304	0.067	
B^2	0.0013	1	0.0013	7.65	0.0199	0.08	
C^2	0.0011	1	0.0011	6.35	0.0304	0.06	
Residual	0.0017	10	0.0002			0.104	
Lack of Fit	0.0008	5	0.0002	0.8389	0.5741		**not significant**
Pure Error	0.0009	5	0.0002				
Cor Total	1.62	19					
Std. Dev.	0.0129	**R^2**		0.9990			
Mean	1.62	**Adjusted R^2**		0.9981			
C.V. %	0.7920	**Predicted R^2**		0.9955			
		Adeq. Precision		148.1424			

Continued on page no. 111

(d) Dilution%

Source	SS	DOF	Mean Square	F-value	p-value	Contri. %	
Model	96.83	9	10.76	2308.78	< 0.0001	99.95	**Significant**
A-Current	9.80	1	9.80	2103.30	< 0.0001	10.11	
B-Welding Speed	64.11	1	64.11	13758.1	< 0.0001	66.18	
C-NTD	20.45	1	20.45	4388.37	< 0.0001	21.11	
AB	0.0008	1	0.0008	0.1717	0.6874	0.00825	
AC	0.0924	1	0.0924	19.84	0.0012	0.095	
BC	0.2048	1	0.2048	43.95	< 0.0001	0.021	
A^2	0.2149	1	0.2149	46.12	< 0.0001	0.022	
B^2	0.1578	1	0.1578	33.86	0.0002	0.16	
C^2	0.1713	1	0.1713	36.75	0.0001	0.17	
Residual	0.0466	10	0.0047			0.048	
Lack of Fit	0.0278	5	0.0056	1.49	0.3374		**not significant**
Pure Error	0.0187	5	0.0037				

Continued on page no. 112

Cor Total	96.87	19					
Std. Dev.	0.0683	**R^2**		0.9995			
Mean	16.44	**Adjusted R^2**		0.9991			
C.V. %	0.4152	**Predicted R^2**		0.9981			
		Adeq. Precision		205.1829			

Table 4.3 Coefficient of determination values

Responses	R^2	Adjusted R^2	Predicted R^2
Bead width	0.9974	0.9950	0.9916
Bead Height	1.0000	0.9999	0.9999
Depth of Penetration	0.9990	0.9981	0.9955
Dilution %	0.9995	0.9991	0.9981

The accuracy of bead width, bead height, Depth of penetration and dilution % and dilution was analyzed by utilizing the determination coefficients, namely "R^2," "Adjusted R^2," and "Predicted R^2". The coefficients of determination (R^2) values for responses are exhibited in Table 4.3. These values, close to 1, shows strong correlation between the predicted and experimental values and show a good model fit. The "Predicted R^2" values align consistently with the corresponding "Adjusted R^2" values. Consequently, these models are suitable for precisely predicting the optimized processing parameters. Fig. 4.3 depicts the expected vs.

actual response, which nearly coincides, demonstrating the applicability of the second-order regression equations and concluding that the model is significant.

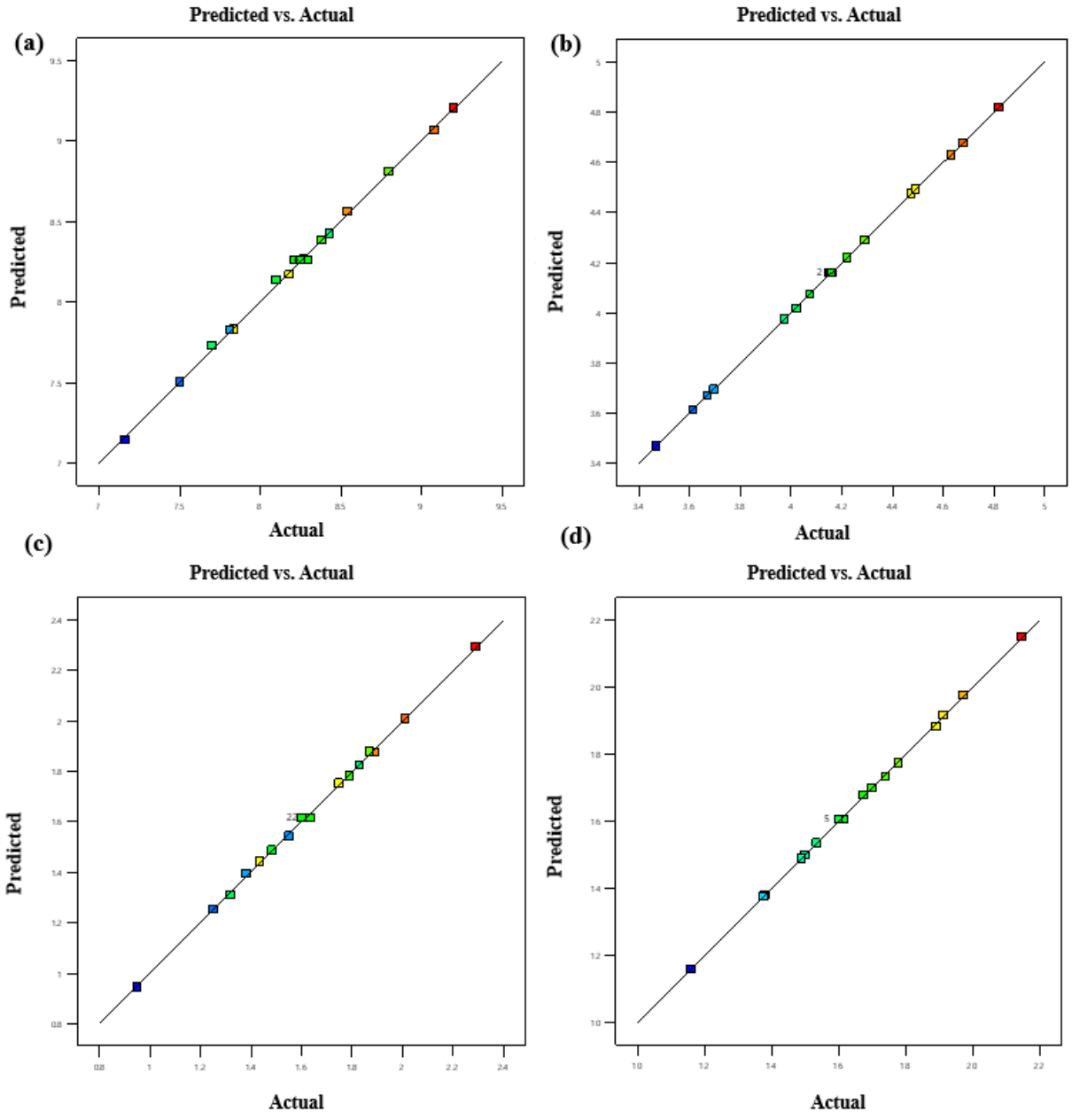

Fig. 4.3 Predicted vs actual graphs for (a) Bead width (b) Bead height (c) Depth of penetration (d) Dilution %

Fig. 4.4 to 4.7 shows the interaction curve of input and output parameters for Bead width, Bead height, Depth of penetration and dilution % respectively. The Factors and their interactions significantly impact the result, according to ANOVA.

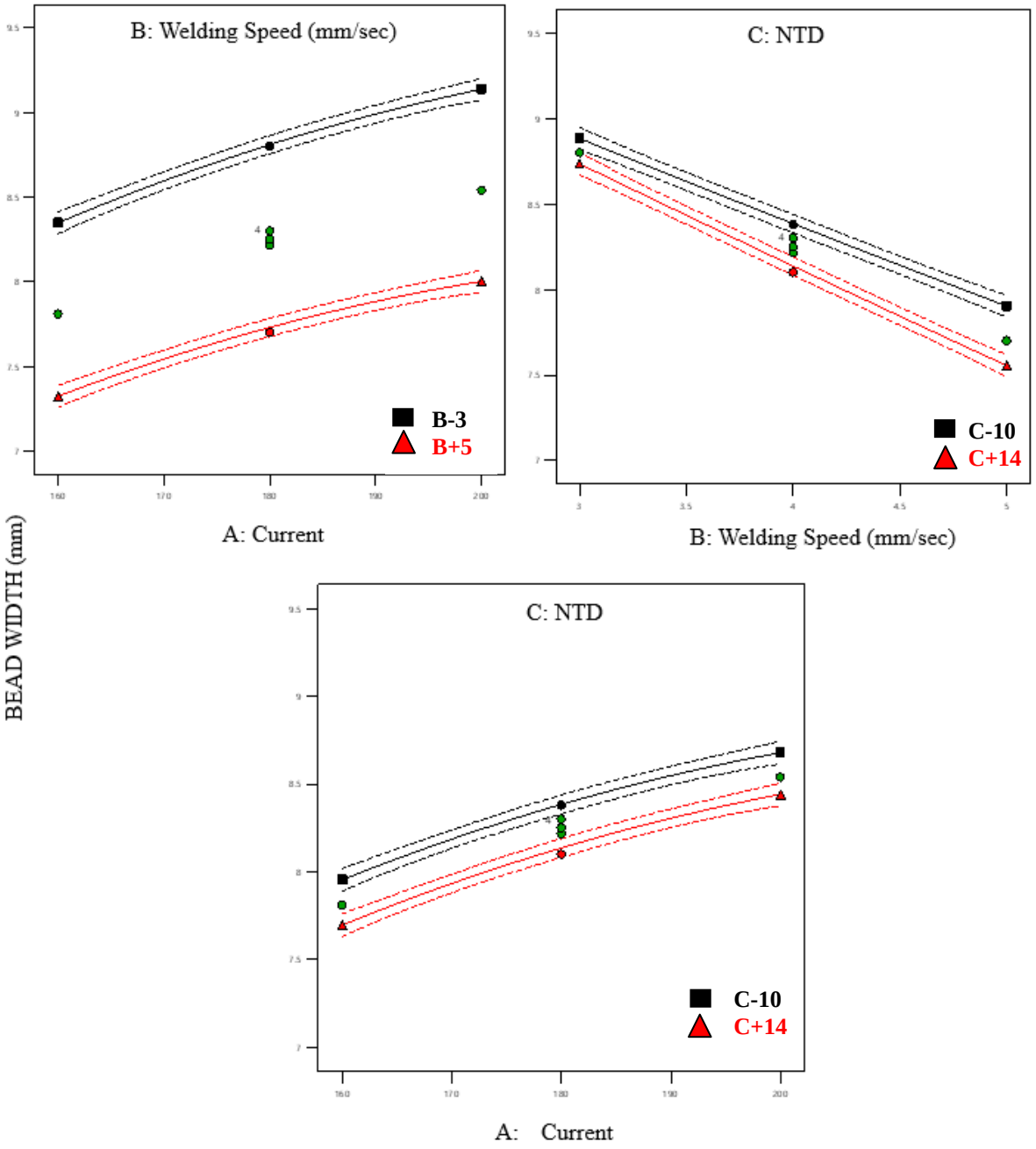

Fig. 4.4. Interaction curve for Bead width

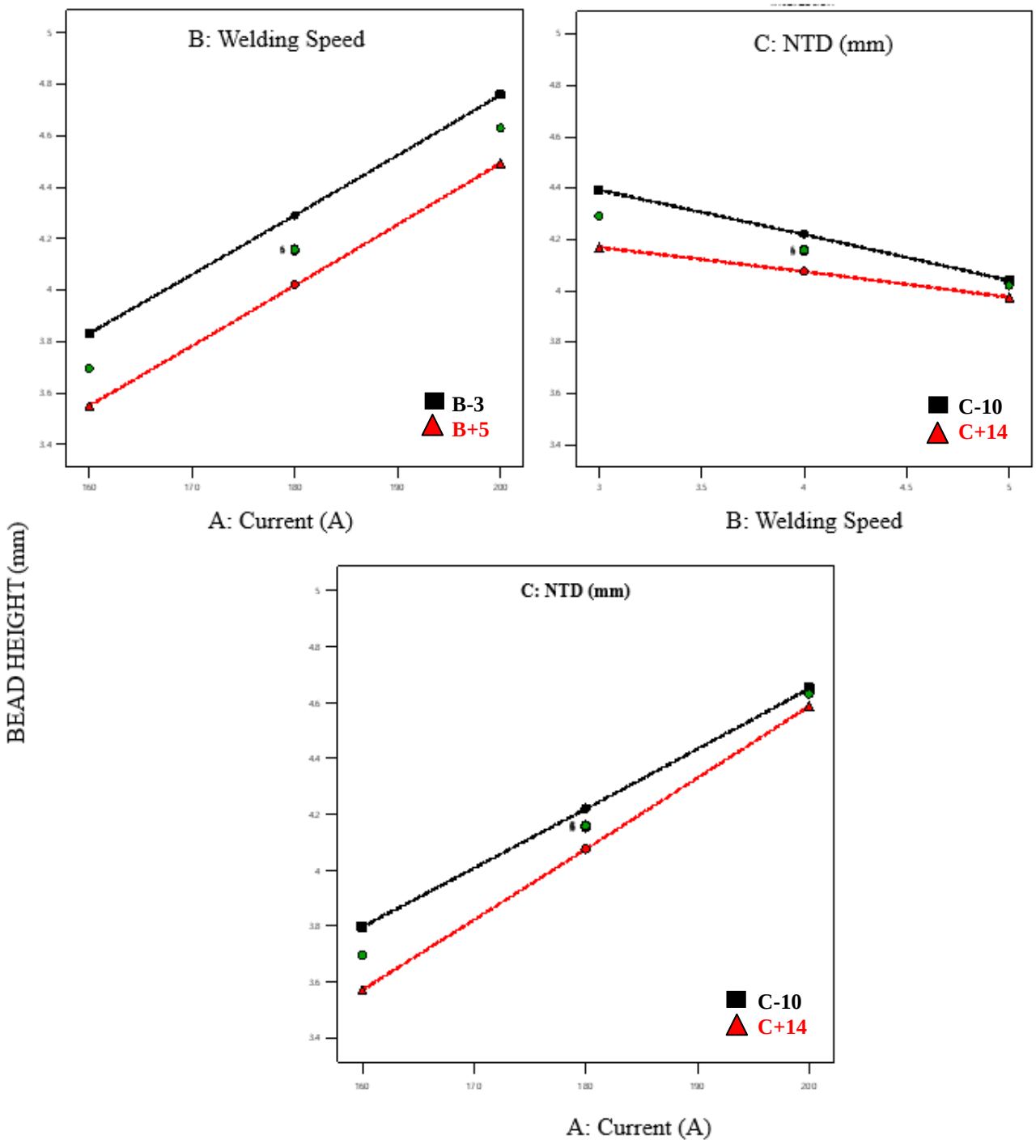

Fig. 4.5. Interaction curve for Bead height

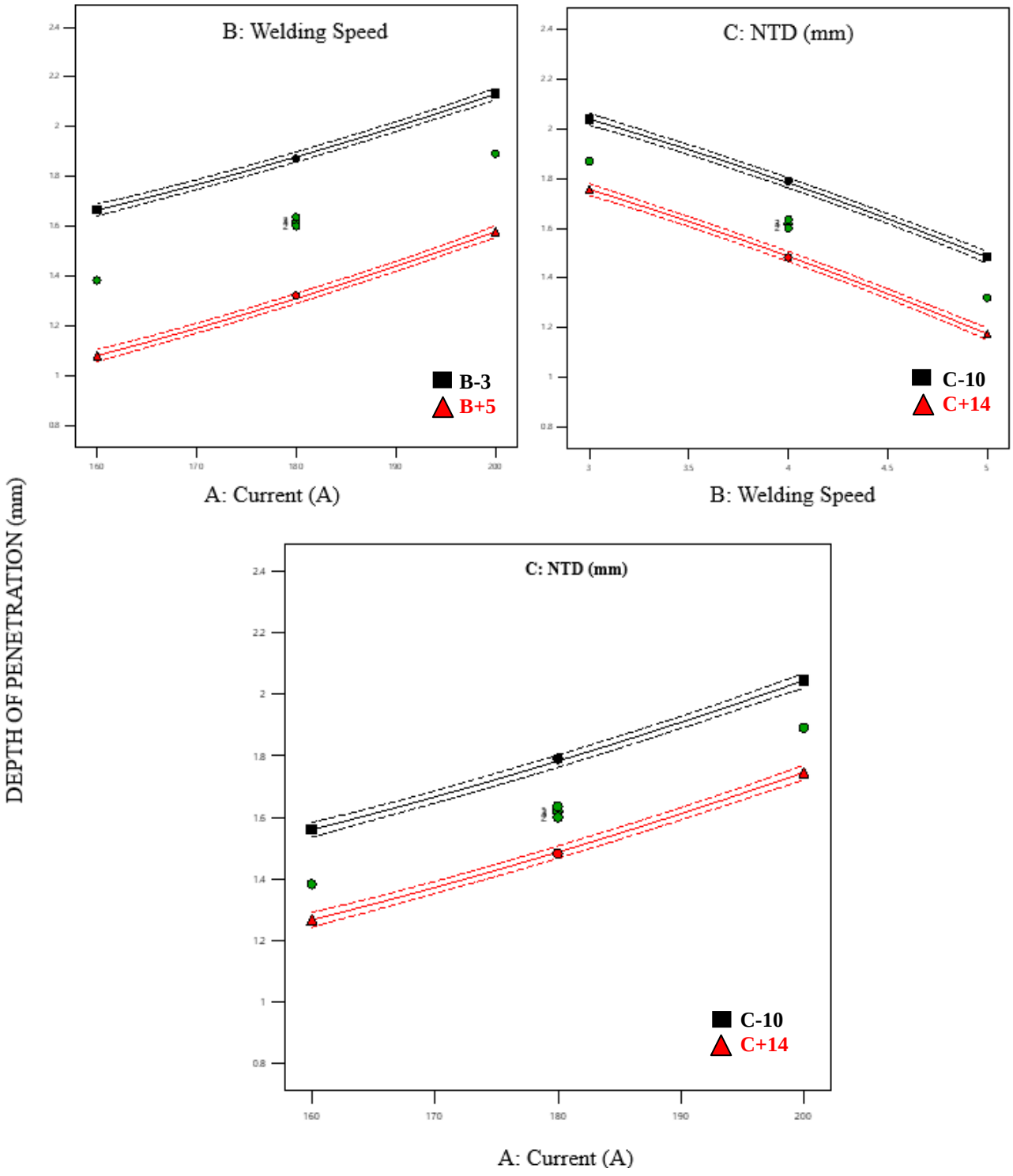

Fig. 4.6. Interaction curve for depth of penetration

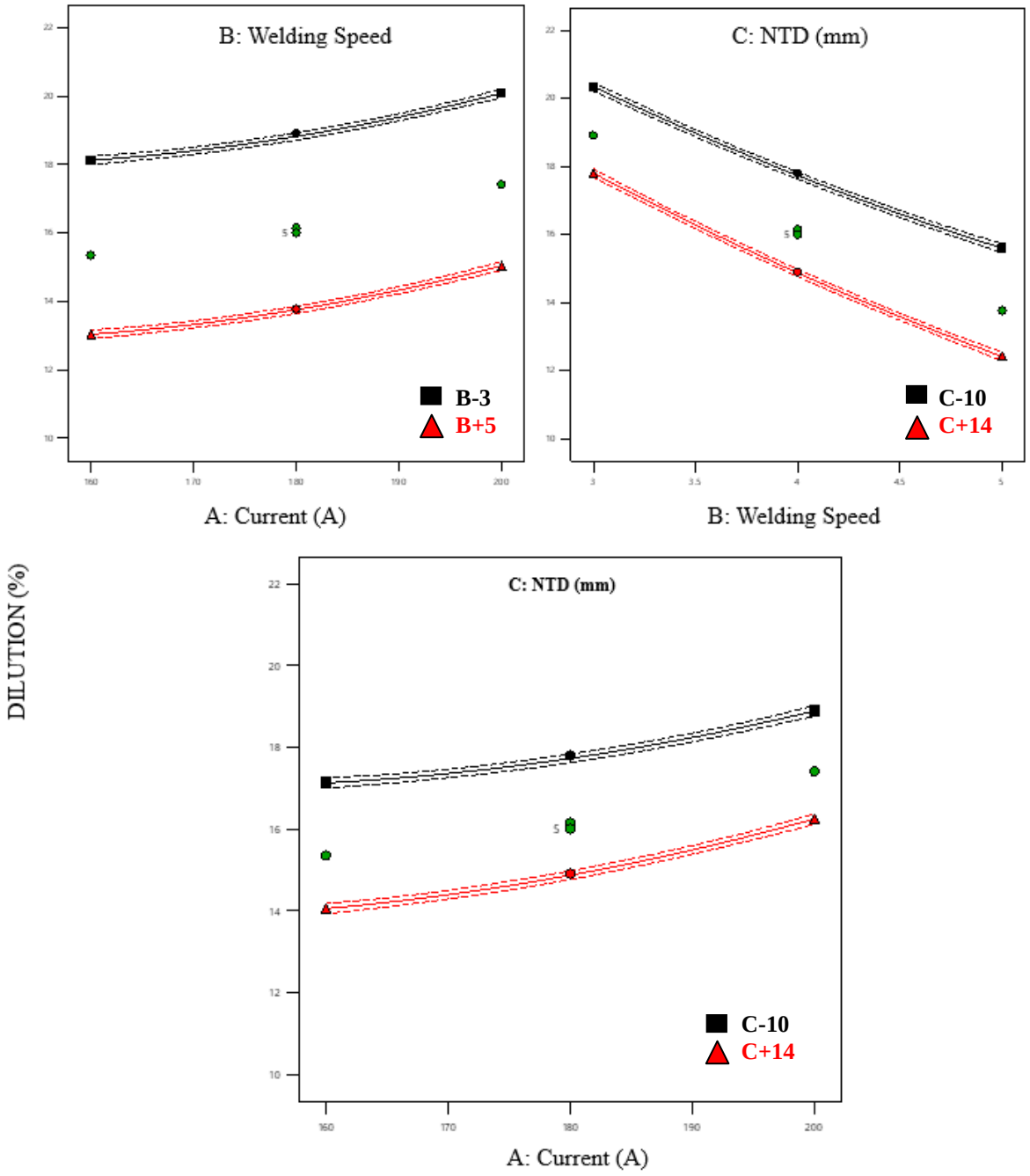

Fig. 4.7. Interaction curve for dilution %

Fig. 4.8 to 4.11 shows the three-dimensional surface plot of interaction between input and response variable for bead width, bead height, depth of penetration and dilution % to

understand the interaction of the process parameters (current, welding speed and Dilution %) with the responses.

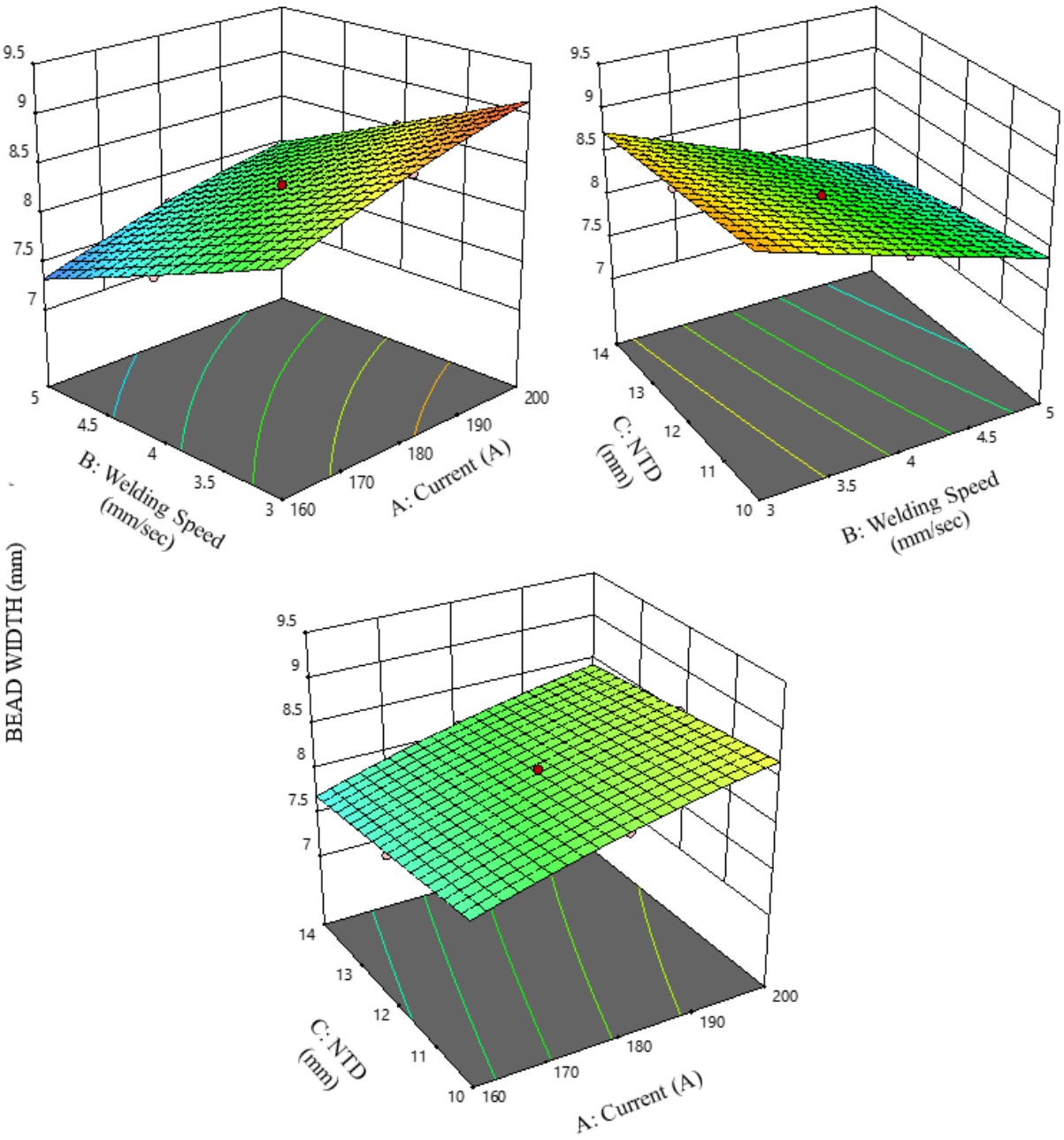

Fig. 4.8. Three-dimensional surface plot of interaction between input and output variables for bead width

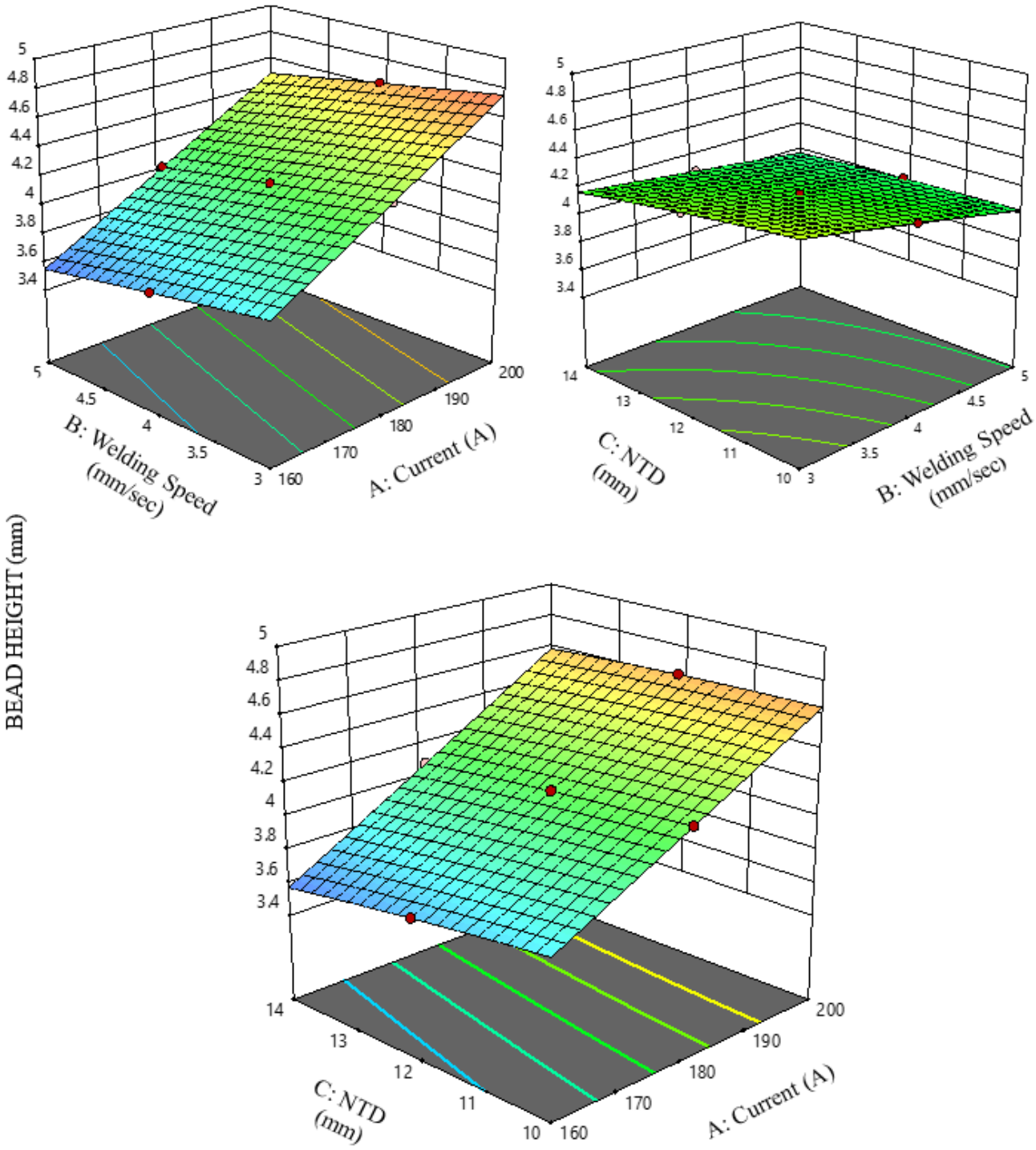

Fig. 4.9. Three-dimensional surface plot of interaction between input and output variables for bead height

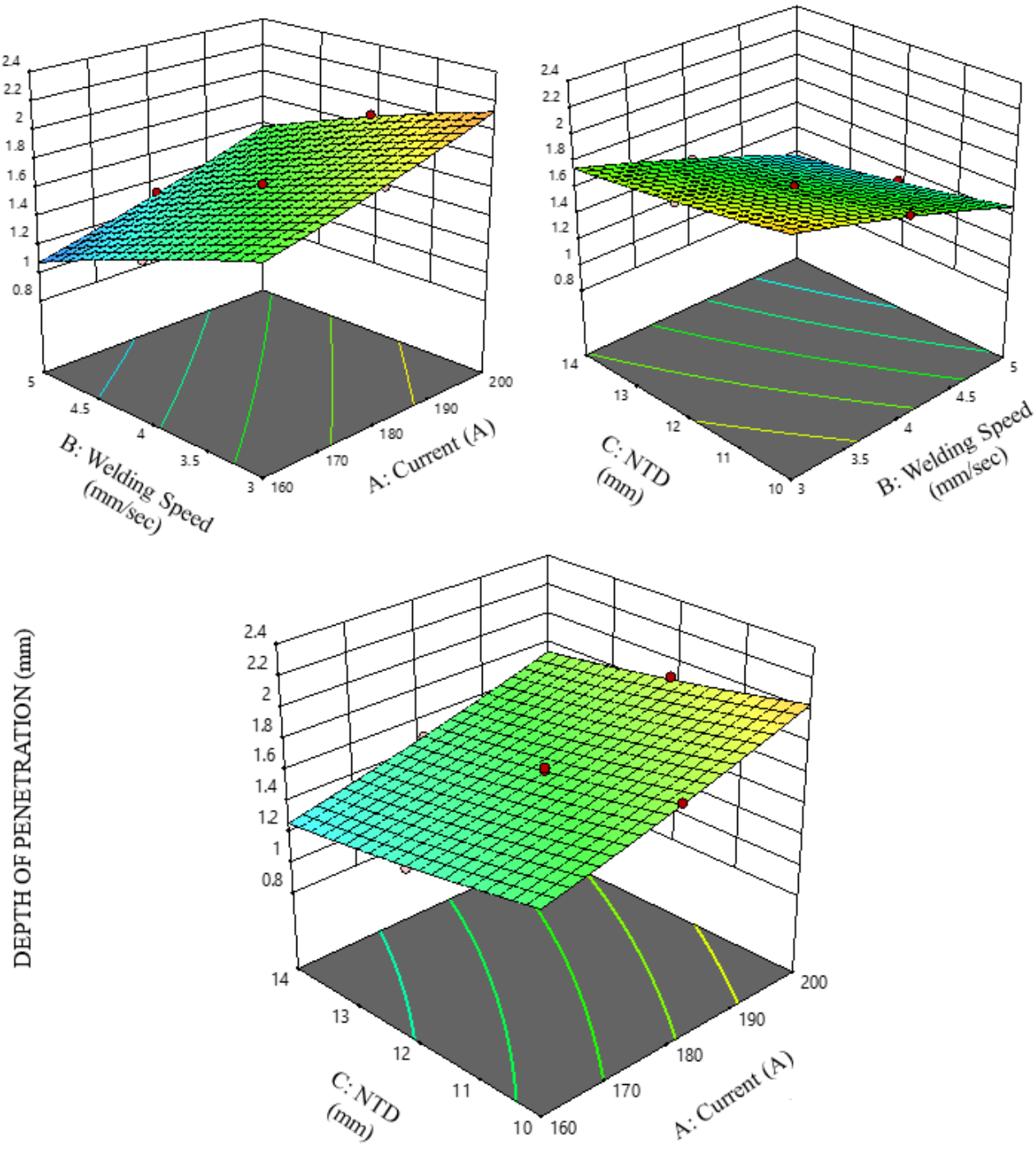

Fig. 4.10. Three-dimensional surface plot of interaction between input and output variables for depth of penetration

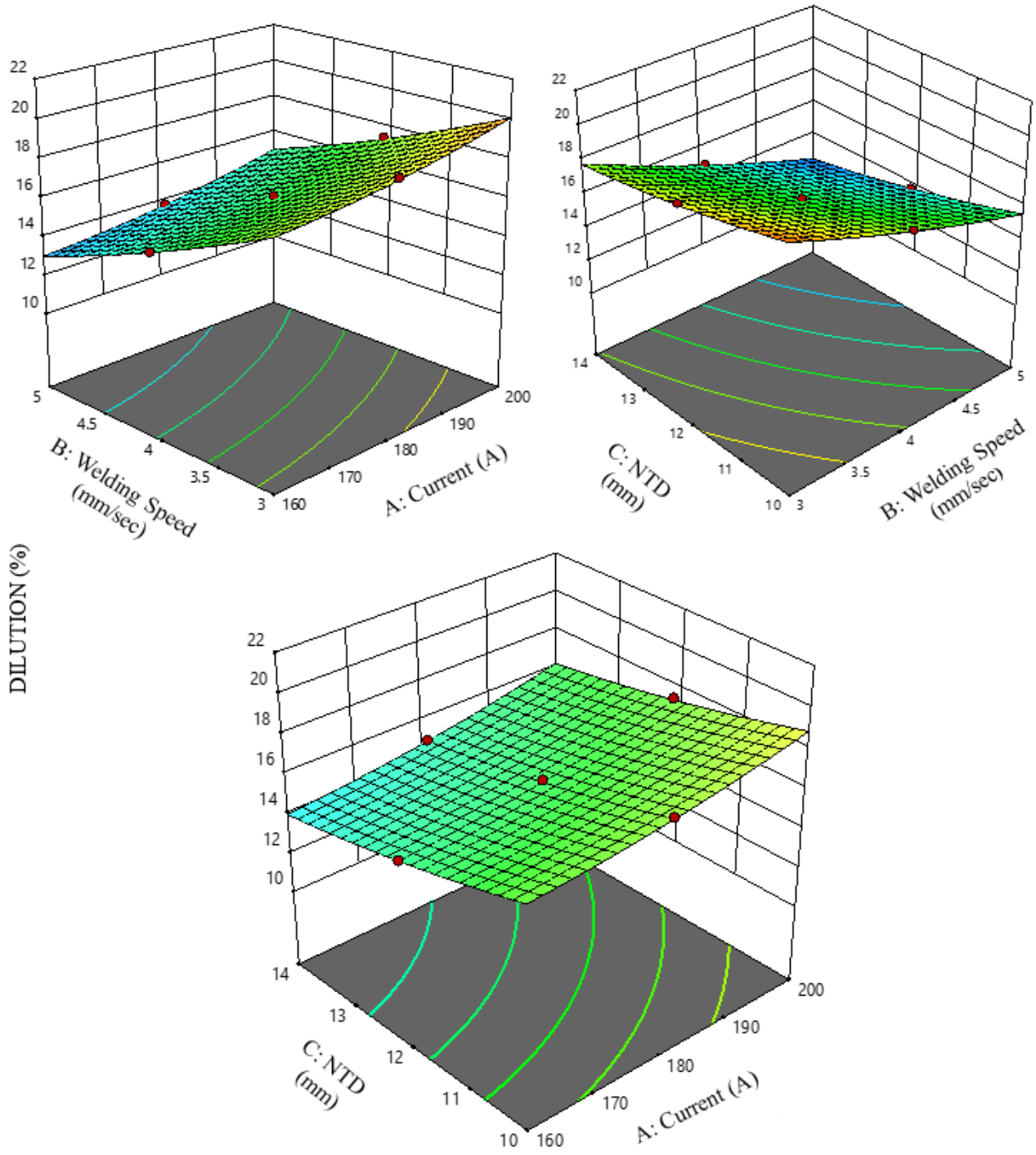

Fig. 4.11. Three-dimensional surface plot of interaction between input and output variables for dilution %

4.1.5 Optimal parameters

The aim was to optimize process parameters to achieve maximum the bead width and height while minimizing the depth of penetration and dilution. Fig. 4.12 shows the numerical optimization of the (a) input welding parameters and (b) response variables.

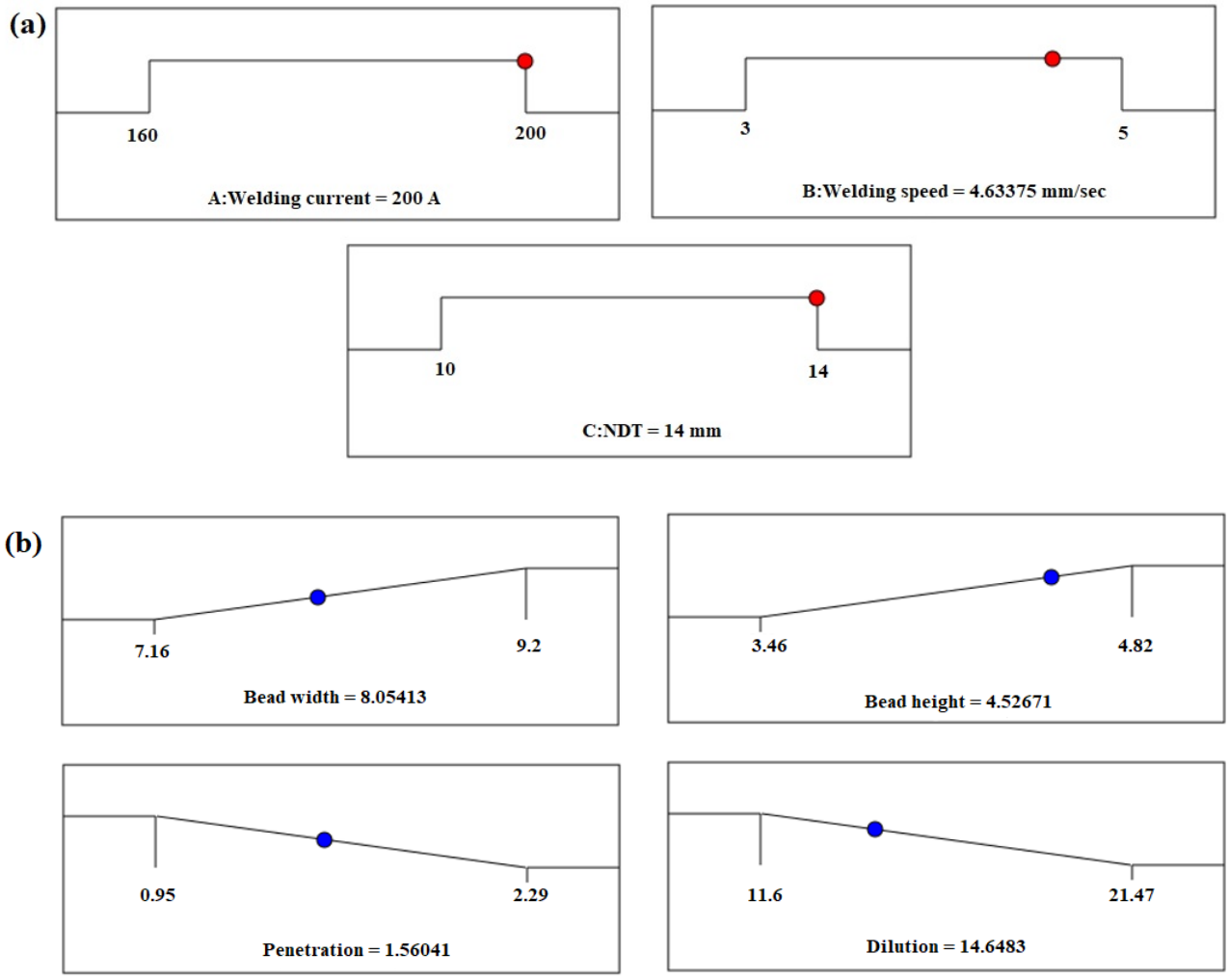

Fig. 4.12 Optimization of the (a) input welding parameters and (b) response variables

The optimal current, welding speeds and NTD values are 200 A, 4.64 mm/sec, and 14 mm, respectively. These optimal parameters generate a response for the values of optimum bead

width (8.05 mm), bead height (4.52 mm), Depth of penetration (1.55 mm) and dilution % (14.64 %), which provides better bonding between substrate and cladding material which improves clad quality and minimizes distortion. A suitable bead geometry with proper dilution is required to produce a better-clad surface.

4.1.6 Confirmation test

The experiments were conducted to verify the mathematical model equations 4.4 to 4.7. Three confirmatory runs were performed using the same experimental setup with the optimal input parameters. The average confirmation test results are shown in Table 4.4. The confirmation test results are close to the predicted values; hence, the model is accurate.

Table. 4.4 Experimental and predicted value of response at optimized conditions (200 A, 4.634 mm/sec, 14 mm)

	Predicted value	**Experimental value**	**% Error**
Bead width	8.0542	8.1054	0.0063
Bead Height	4.5267	4.6010	0.0162
Penetration	1.5604	1.4924	-0.0456
Dilution	14.6483	15.2424	0.0389

4.1.7 Effect of input welding parameters on responses

Macro images of weld bead shown in Fig. 4.2 demonstrate how weld bead geometry and dilution % are significantly impacted by process parameters, such as welding current, welding speed, and nozzle to workpiece distance.

a) Effect of welding speed on bead geometry and dilution %

Fig. 4.13 illustrate that, an increase in welding speed (3-5 mm/sec) results in a decrease in depth of penetration, that is nearly 30% of the initial value due to the low heat input. Furthermore, bead width is demonstrated to decrease as welding speed increases, but bead height is less affected than bead width because of an increase in heat input per unit length of the weld bead caused by high welding current. At lower welding speed, a higher amount of heat input is generated on the substrate material, causing more melting and deeper encroachment, results in increasing dilution.

b) Effect of welding current on bead geometry and dilution %

Fig. 4.13 also illustrates how increase in welding current effects the bead geometry and dilution %. The penetration increases as current increases. This could be because the arc spreads over a larger region of the base metal as the voltage increases due to the arc cone's growth. The increase in heat input causes the weld to gradually increase. On increasing welding current, the dilution % increases due to the overheating of molten droplets at the filler wire's tip, leading to more significant dilution in the weld pool. Increase in welding current has positive effect on bead width and bead height.

c) Effect of Nozzle to workpiece distance on bead geometry and dilution %

Further, it was observed that Dilution %, penetration and bead height decrease as the distance (NTD) between the nozzle and the workpiece rises. This is brought on by insufficient gas efficiency during lengthy NTDs and excessive heating during short NTDs. In contrast, bead width was less impacted by an increase in nozzle to workpiece distance because heat input per unit length of the weld bead decreases on increasing NTDs.

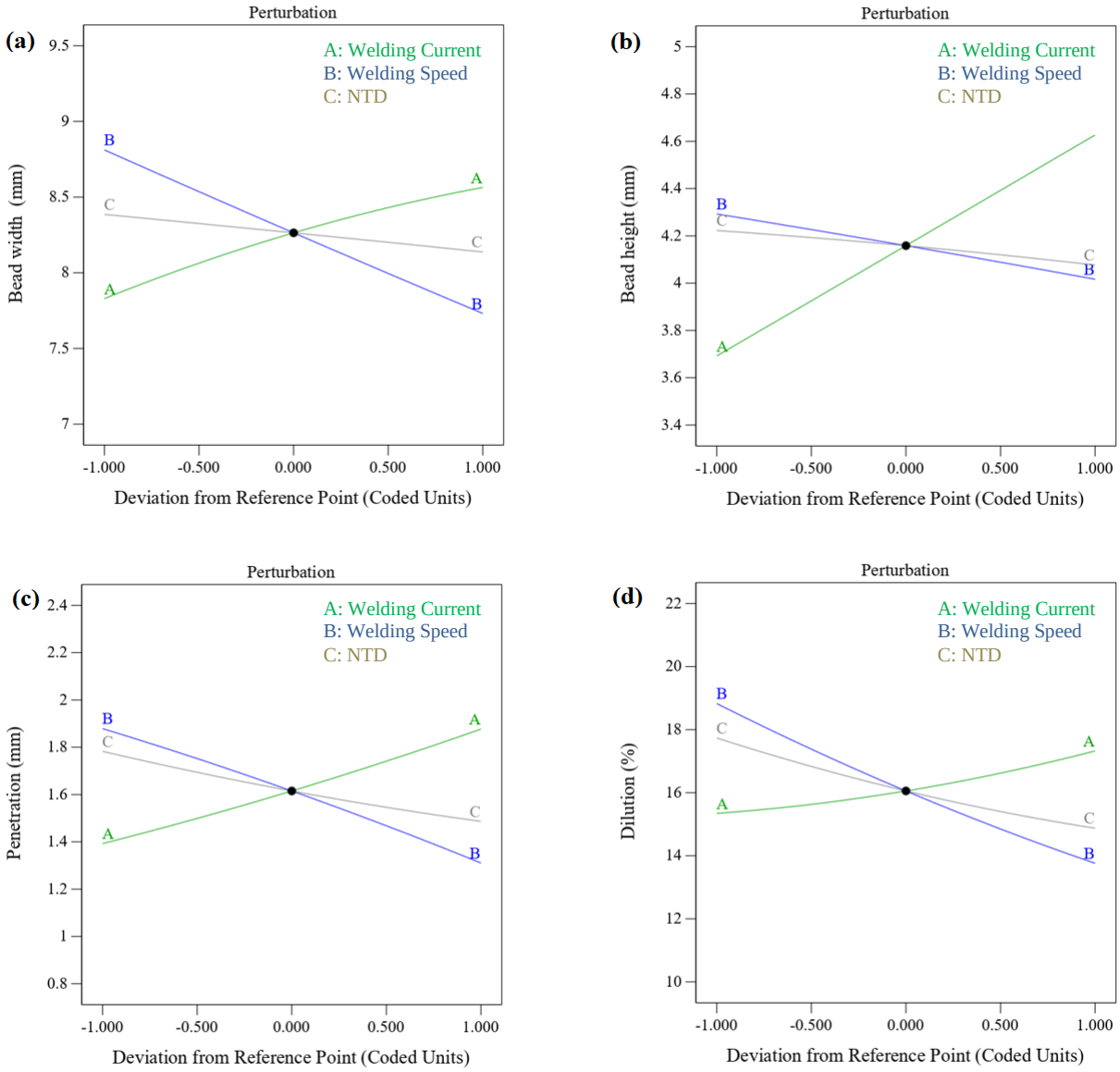

Fig. 4.13 Effect of input parameters on response variables (a) Bead width (b) Bead height (c) Depth of penetration (d) Dilution

4.1.8 Microstructure characterization

The clad samples were prepared from the optimal parameters. The cross-section of the clad sample was extracted for the microstructural studies, as shown in Fig. 4.14. Fig. 4.15 (a) and

(b) display the SEM images of the weld bead region and dilution region and respective EDS plots are shown in Fig. 4.15 (c) and (d).

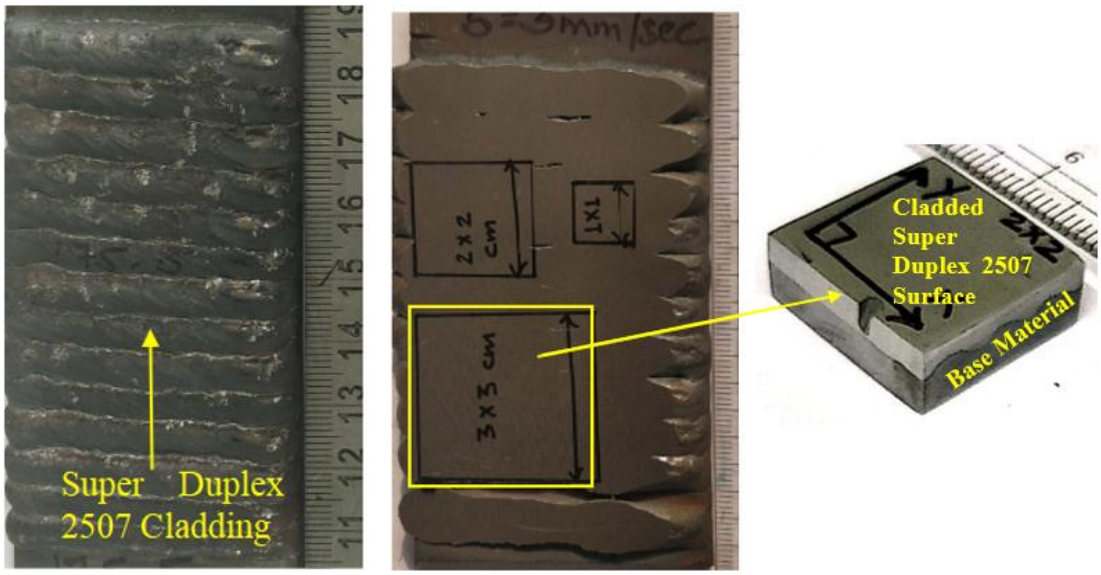

Fig. 4.14 Extracted CMT clad sample

The EDS plot confirms the uniform dissolution of alloying elements with the base material. There is no considerable difference in the chemical composition of the clad bead and dilution region. The SEM image confirms the higher fraction of ferrite in the dilution region compared to the clad bead region due to the re-melting of the adjacent base alloy during the cladding process. The rate of cooling influences the development of γ-austenite phase in super duplex stainless steel [Kannan et al., (2021)]. The different types of austenite were generated by the subsequent transitions of the solid-state ferrite phase that solidified through the melted metal: grain boundary austenite (GBA), Widmanstätten austenite (WA), intragranular austenite (IGA) and partially transformed austenite (PTA). GBA was primarily detected at the interfaces of ferrite grains, displaying a uniform orientation in the direction of the Z-axis. WA had a side-plate shape and occupied a considerable percentage

of the columnar ferrite. IGA exhibited a smaller size compared to both GBA and WA and was scattered within the ferrite grains [Lervåg et al., (2020)]. The clad sample has less micro inclusion and a better finish.

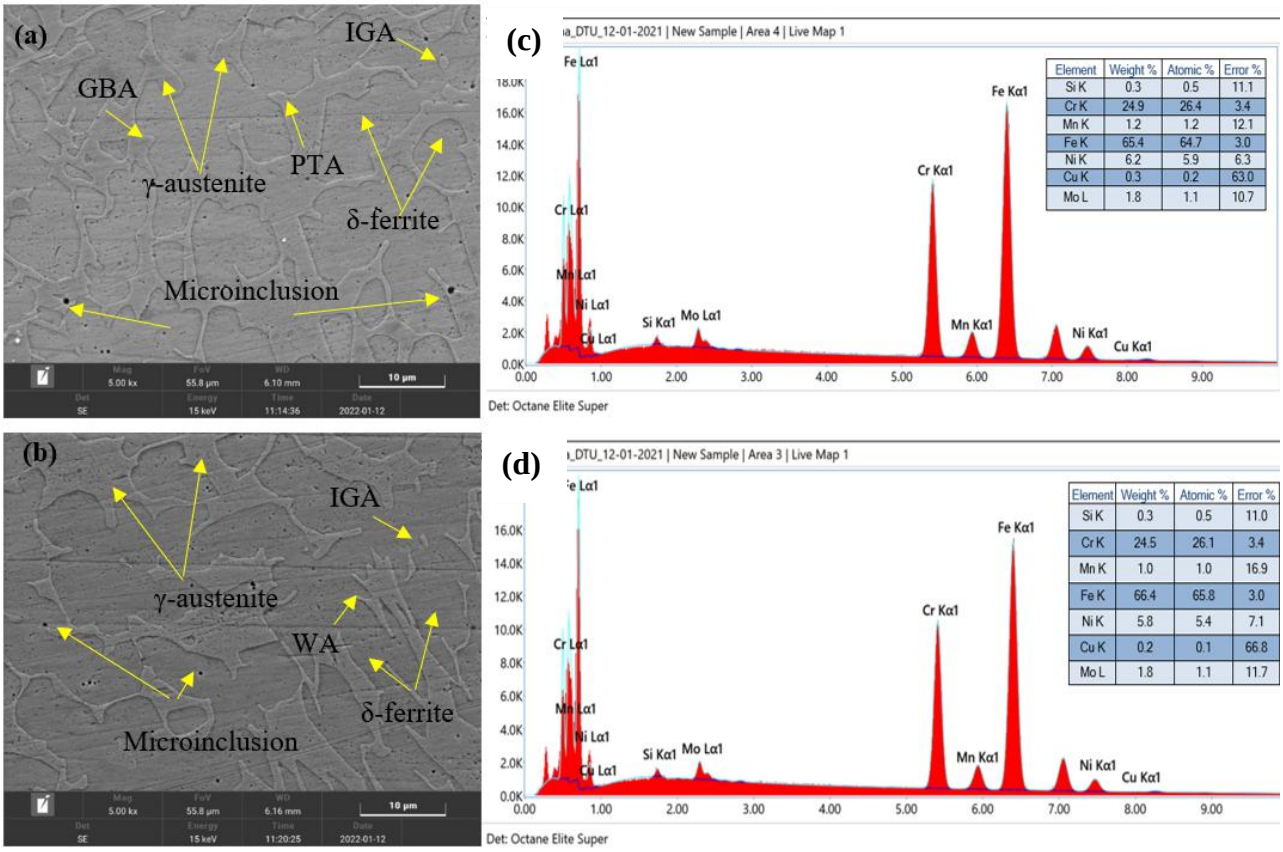

Fig. 4.15 SEM images of the clad sample (a) Weld bead Region (b) Dilution Region (c) EDS plots of Weld bead Region (d) EDS plots of Dilution Region

4.1.9 Microhardness

The micro-hardness of super duplex 2507 SS clad samples fabricated at optimum parameters was examined by the Vickers Micro-hardness tester (DRAMIN-40 STRUERS) at a load of 500g and a dwell time of 10 seconds as per the ASTM E384 standard (Mishra et al., 2023). Microhardness, variation along the clad surface, dilution region and base metal region, is

shown in Fig. 4.16. The Fig. shows that the microhardness increases in the order of unaffected base metal, HAZ, and clad bead region. The mean microhardness of the sample is 253.52 ± 5 HV0.5. The top surface of the clad bead had a higher microhardness due to a faster cooling rate. The existence of partially unmelted grains, which are partly introduced as nuclei by the clad bead's new precipitating phase during the solidification phase, causes the high hardness of the dilution boundary region in the clad beads. Microhardness decreases in the HAZ. The area close to the dilution region has relatively slow cooling rates, resulting in coarse-grained microstructure, whereas the area adjacent to the base metal observes more significant thermal gradients [S. Kumar & Shahi, (2011)].

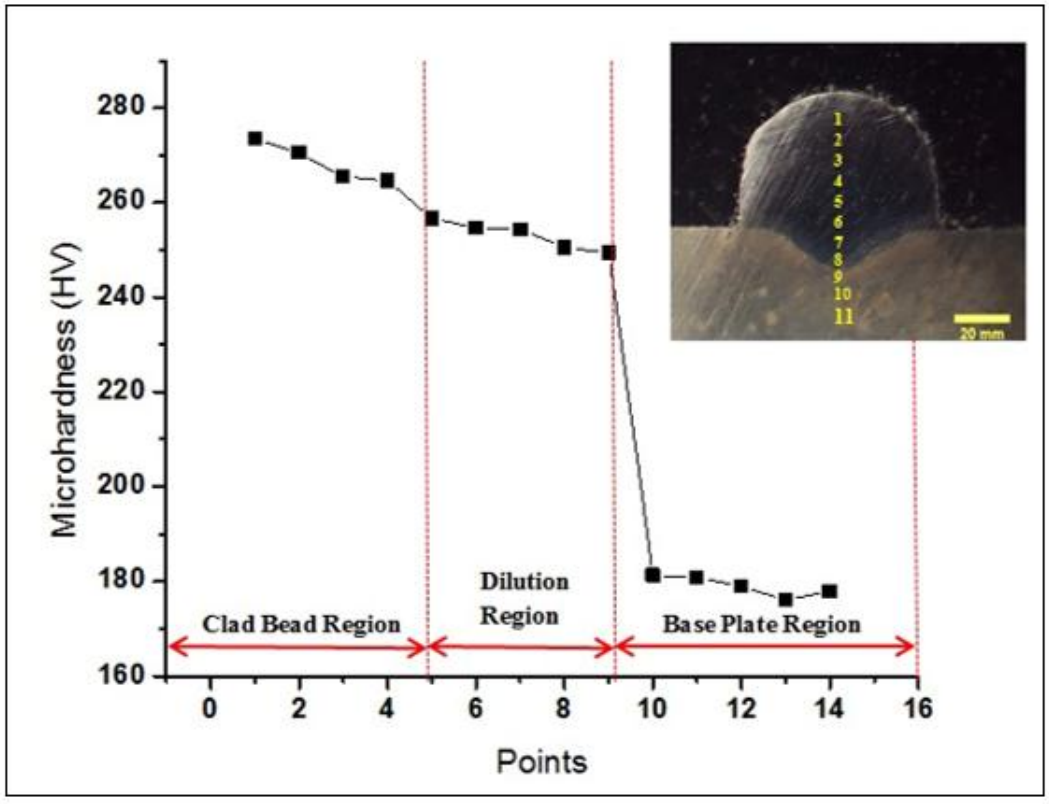

Fig. 4.16 Microhardness variations along the clad surface, dilution region and base metal region

4.1.10 Wear properties

Wear tests of super duplex 2507 clad samples were conducted using a linear reciprocating ball on a disc tribometer (DUCOM) as per ASTM standards G133-05 [Mishra et al., (2023)]. Wire EDM extracted the wear sample size of 20mm x 20mm from the middle of the clad surface, as shown in Fig. 4.14. The top surface of the clad wear test specimens was polished with a 1500-grade emery sheet before testing. A tungsten carbide ball with an 8 mm diameter was tested against wear test specimens. Reciprocating wear tests were carried out at a constant frequency of 10 Hz and normal loads of 40 N for 1000 seconds. To assure reproducibility, all wear tests were repeated three times. The variation of wear rate to Time and the variation of coefficient of friction (COF) with sliding Time for base metal and clad surfaces are shown in Fig. 4.17 (a) and (b), respectively. Initially, at 0 to 60 sec, the COF increases at a higher rate due to a higher wear rate, further gradually becoming stable as the sliding Time increases. The hard phases in the super duplex stainless-steel act as a protective layer during wear tests, increasing wear resistance. The COF of the clad surface is lesser than that of the base material because the hard surface creates a contact area when a constant force is applied [Chowdhury & Helali, (2007a)]. SEM with EDS analysis is used to investigate the wear behaviour of the worn samples, which is shown in Fig. 4.18 (a), (b) and (c), which shows that the wear track width of the base material is larger than the clad surface wear track, and wear debris also visible on the wear surface along the sliding direction, Because of the higher hardness of the surface, the contact surface area with a hard counter ball may be less than the base material. Fig. 4.18 (c) shows an overlay of element line

scanning over the SEM image of the clad surface and its wear track, which indicates the decrease in chromium content in the wear track.

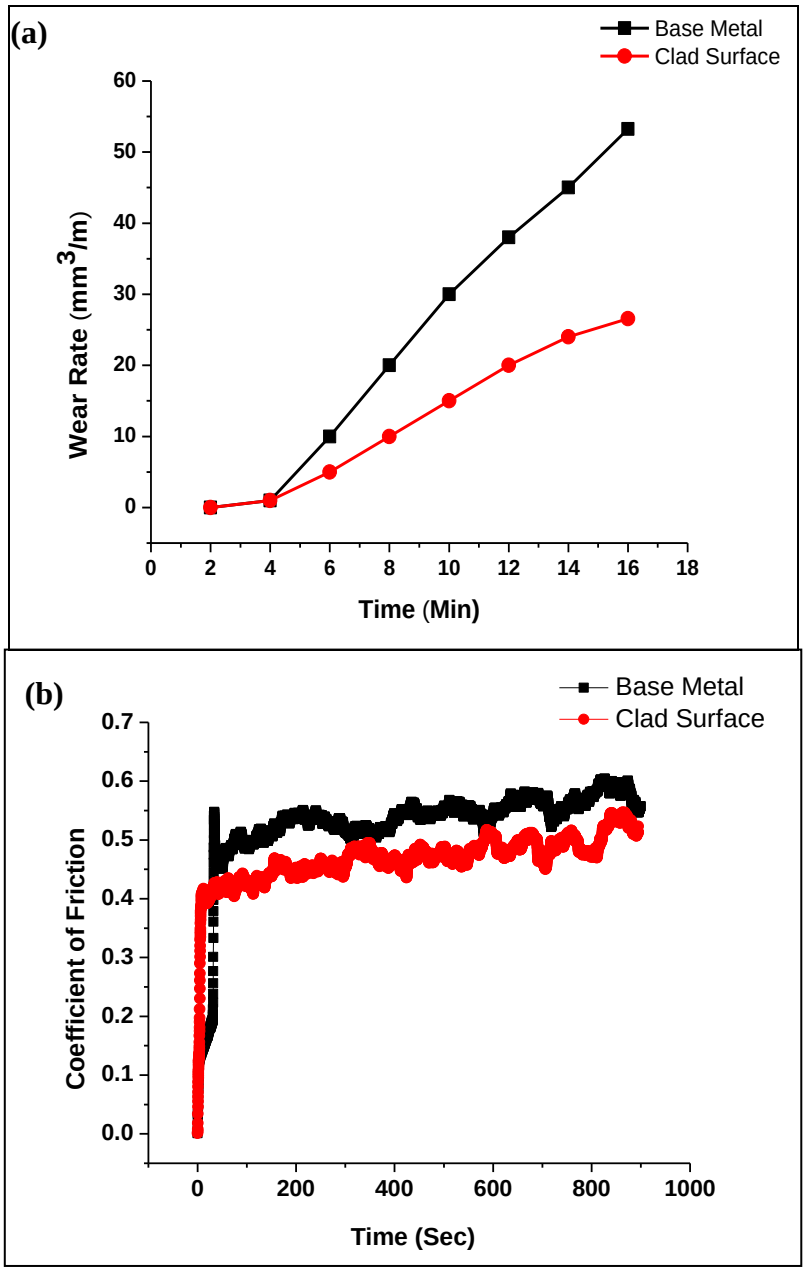

Fig.4.17. (a) Wear rate vs Time (b) Coefficient of friction behaviour of cladded surface and base material

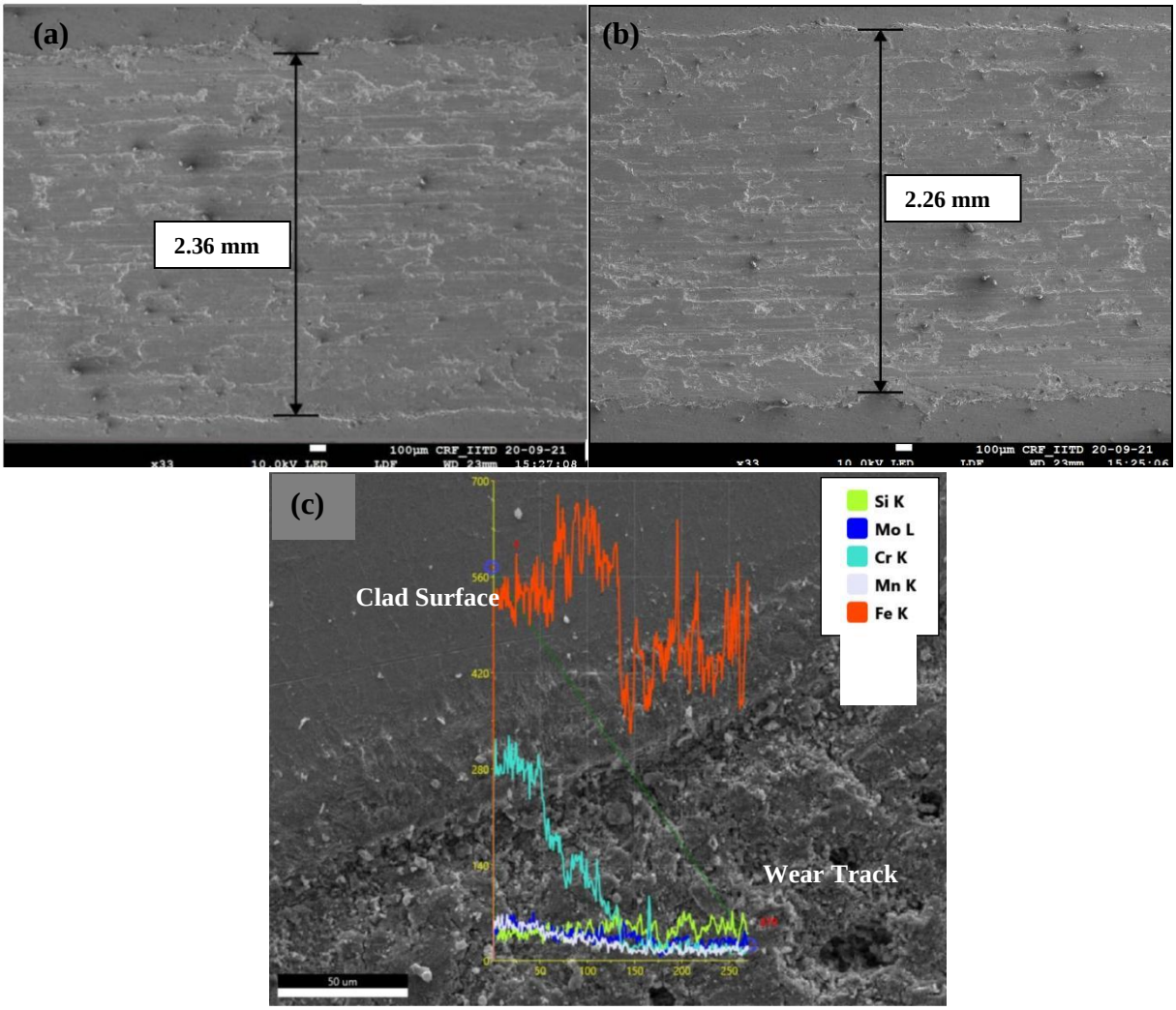

Fig. 4.18. EDS analysis of wear track of (a) low carbon steel (b) super duplex 2507 (c) element line scanning over the SEM image of the clad surface and its wear track

The primary mechanism causing the wearing effect is abrasive. The wearing period deepens oxidative damage and alters the worn surface morphology. Due to the large exposed surface, the metallic pieces remaining at the contact can break into tiny sizes and oxidize quickly.

4.2 CMT CLADDING PROCESS OF AUSTENITIC STAINLESS STEEL ON LOW CARBON STEEL

4.2.1 Microstructural analysis

Fig. 4.19 (a-e) shows the microstructures of the fusion region and the clad bead regions of austenitic stainless steel at different welding speeds. Base metal consisted of refined and equiaxed austenite grains. The dendritic arms grow along the direction of the heat flow. The clad bead comprises a few columnar dendrites that are growing epitaxially. Columnar dendrites develop parallel to the direction of deposition. Cellular dendrites have been missing in the contact area, as illustrated in Fig. 4.19 (a). A deeper examination revealed that the delta ferrite developed across most of the fusion border region, as shown in Fig. 4.19 (b). This melting and re-solidification were caused by the continuous boundary layer, which forms when a small quantity of the nearby base metal melts in situ due to the superheat released from the weld pool. Fig. 4.19 (c) shows the presence of cellular dendritic austenite that contains δ –ferrite in clad bead region. Cellular dendrites without secondary arms, austinite grains, and equiaxed grains characterize the microstructure morphology from the substrate to the clad area due to the increasing rate of grain growth and decreasing temperature gradient. This growth transition is mainly caused by the molten pool's temperature gradients and grain growth rate austenite in the deposited area to the right of the cladding line exhibit no evidence of retained ferrite. Fig. 4.19 (d) and (e) illustrate the FESEM image of a clad surface prepared at 3 mm/sec and 6 mm/sec welding speeds, respectively. It is inferred from the observation that the clad surface prepared at low

welding speed has more inclusions than the surface prepared at high speed due to the high heat input, which deteriorates the surface profile of the sample and mechanical properties.

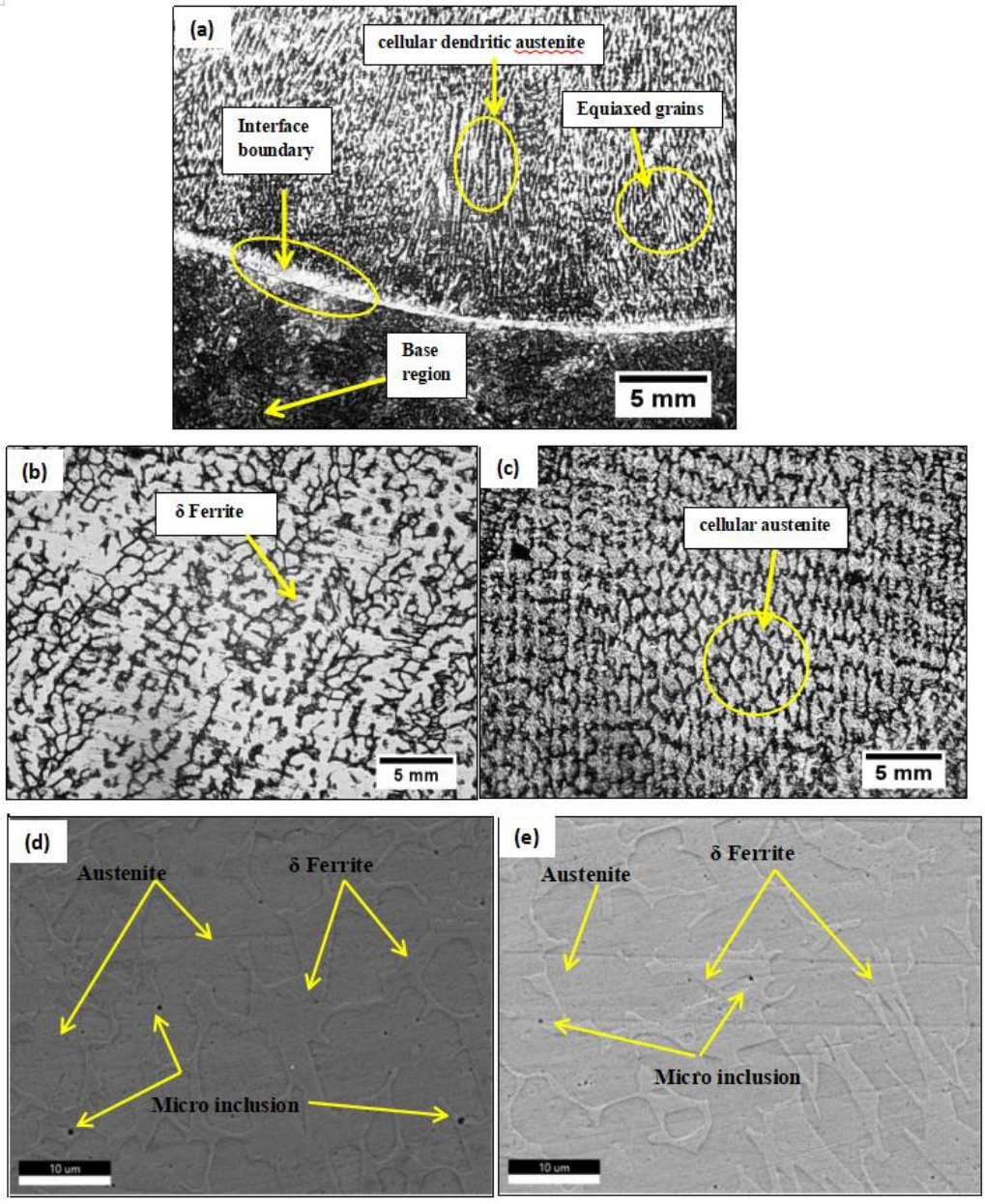

Fig. 4.19 Microstructure of austenitic SS (308L) (a) clad sample (b) Fusion region of the clad sample (c) cellular austenite in the clad region (d) FESEM image of the clad surface at 3mm/sec welding speed (e) FESEM image of clad surface at 6 mm/sec welding speed

4.2.2 MICROHARDNESS

The average microhardness value taken at the fusion region of different clad surface samples is exhibited in Table 4.5. It was found that the heat input decreases, and microhardness increases with increasing welding speed. This increase in microhardness with an increase in welding speed is due to a decrease in heat input which facilitates fast cooling of the weld metal containing finer grains and reduces the delta ferrite in the austenite matrix of weld metals [Chuaiphan & Srijaroenpramong, (2014)].

Table 4.5: Microhardness and wear test results

S.NO	Welding speeds (mm/sec)	Heat Input (J/mm)	Microhardness ($HV_{0.5}$)	Wear rate (mm^3/m)	Coefficient of Friction
1.	3	630	233±15	30.36	0.7
2.	4	472.5	249.85±15	26.56	0.6
3.	5	378	272± 15	23.5	0.5
4.	6	315	363.24± 15	21.66	0.4
5.	Base Plate	-	175± 15	53.24	0.8

Fig. 4.20 displays the micro-hardness of clad specimen's cross-section taken at various regions. The cladding region was harder than the base material due to the presence of Cr and Ni elements transmitted from the filler material. Compared to the fusion border zone, a little reduction in hardness was seen in the fusion region because of the existence of partially unmelted grains in the fusion border zone, which the new precipitating phase of the weld metal partially adopts as nuclei during the solidification stage [Chuaiphan &

Srijaroenpramong, (2014)], also due to the work-hardening effect, the weld material loses some of its original strength in the fusion zone during solidification. The hard phases found in the 308L SS clad bead operate as a protective barrier during wear testing, which increases the low carbon steel (base plate's) wear resistance.

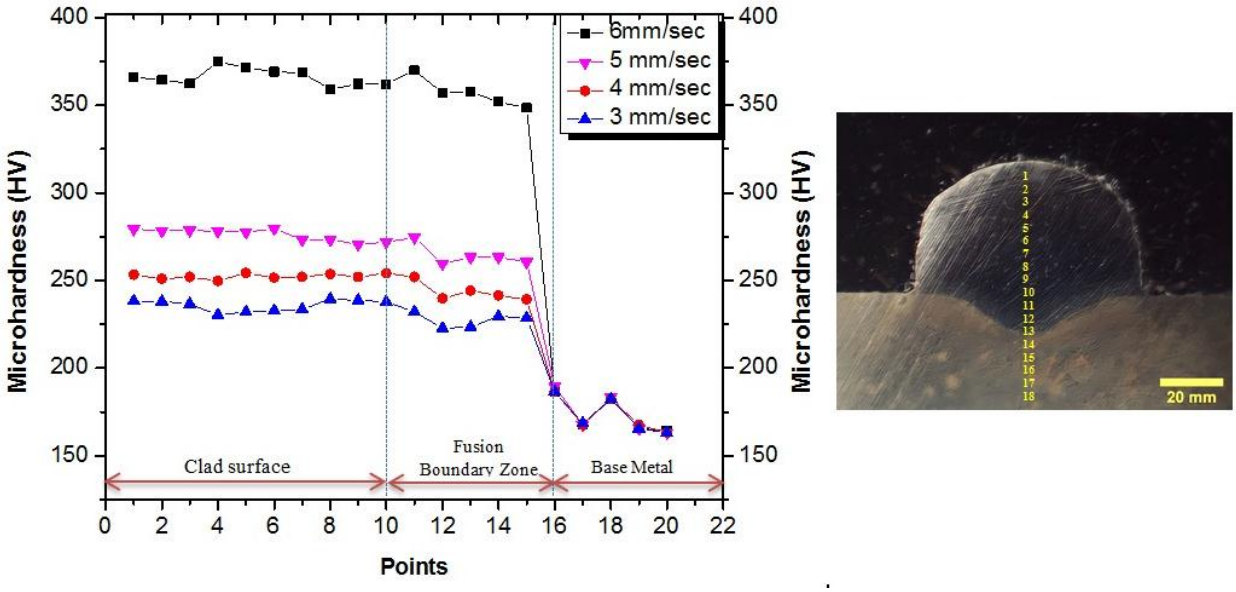

Fig. 4.20 Microhardness value of 308L SS clad specimen taken at different regions at different welding speeds

4.2.3 WEAR ANALYSIS OF CLAD SURFACE

The schematic diagram of reciprocating sliding wear is shown in Fig. 4.21 The wear particles in the tribo-pair (Tungsten/308L SS clad surface) might react differently. The various wear mechanisms such as oxidation, adhesive, abrasive and fatigue wear took place during the wear test. The worn-out particles can stick to the counter surface through adhesive contact and react with the nearby medium, forming oxidation wear. The worn-out particles may be snagged on the surfaces and roll like a third body between two sliding

surfaces, creating abrasive wear. The hard particles moving over the softer surface will form grooves on the clad surfaces. Pitting on the surface might emerge when the speed is increased considerably, i.e., Fatigue wear [Selçuk et al., (2001)].

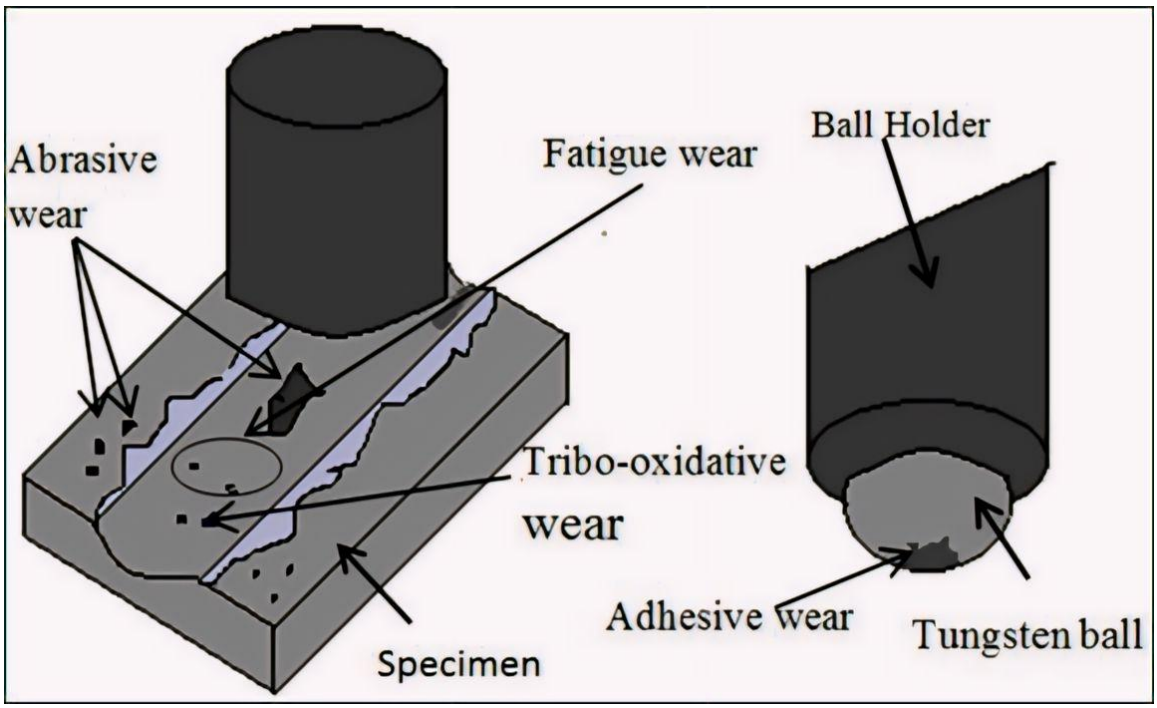

Fig. 4.21 Wear on the clad surface during the wear test.

The base material and clad material wear track are shown in Fig. 4.22 (a) and Fig. 4.22 (c), respectively. The base material has a broader wear track than the cladding surface. The base material worn surface comprises pits, micro-cracks, spallation, and ploughing, as seen in Fig. 4.22 (b). Abrasion and delamination have developed during wear on low-carbon steel surfaces because normal and tangential loads are transferred through the inescapably present asperities on a surface when two surfaces are in sliding contact. The subsurface deteriorates or wears away during this sliding process, with the highest plastic strain occurring beneath the contact zone. Cracks form and spread (delamination fractures) when

the plastic strain increases and surpasses the critical strain for fracture (delamination), eventually losing the surface material.

On the other hand, the surface with the cladding layer has lesser spallation, which indicates smoother abrasion wear. The flake removal from the clad surface is primarily responsible for the emergence of fracture particles on the worn surface, as shown in Fig. 4.22 (d). Detachable abrasive particles visible while wearing provide the impression of ploughs. The primary mechanism of wearing is abrasive. Also, it alters the morphology of the worn surface and deepens the oxidized wear. This may be because the contact surface for the 308L cladding sample is a lower wear rate than the base material due to having a higher hardness value. From Table 6.1, it has been noticed that the wear rate of low carbon steel is reduced considerably to 30.63 (mm^3/m) from 53.24 (mm^3/m) after cladding of 308L (at 6mm/sec welding speed). Cladding improves the COF because a steady force on a hard surface produces less contact area, resulting in low COF and less wear rate. The COF of the clad material decreased for increased welding speeds for constant loads and frequencies due to a reduction in heat input, which enables rapid cooling of the weld metal that contains finer grains and also reduces the delta ferrite in the austenite matrix of weld metals on increasing welding speeds. The COF and wear rate shows a decreasing trend with increasing welding speed. Also, it was found that the micro-hardness profiles near the wear tracks were higher than the initial micro-hardness value, indicating that underlying layers underwent a martensitic transformation during sliding, which is confirmed in the XRD plot shown in Fig. 4.23.

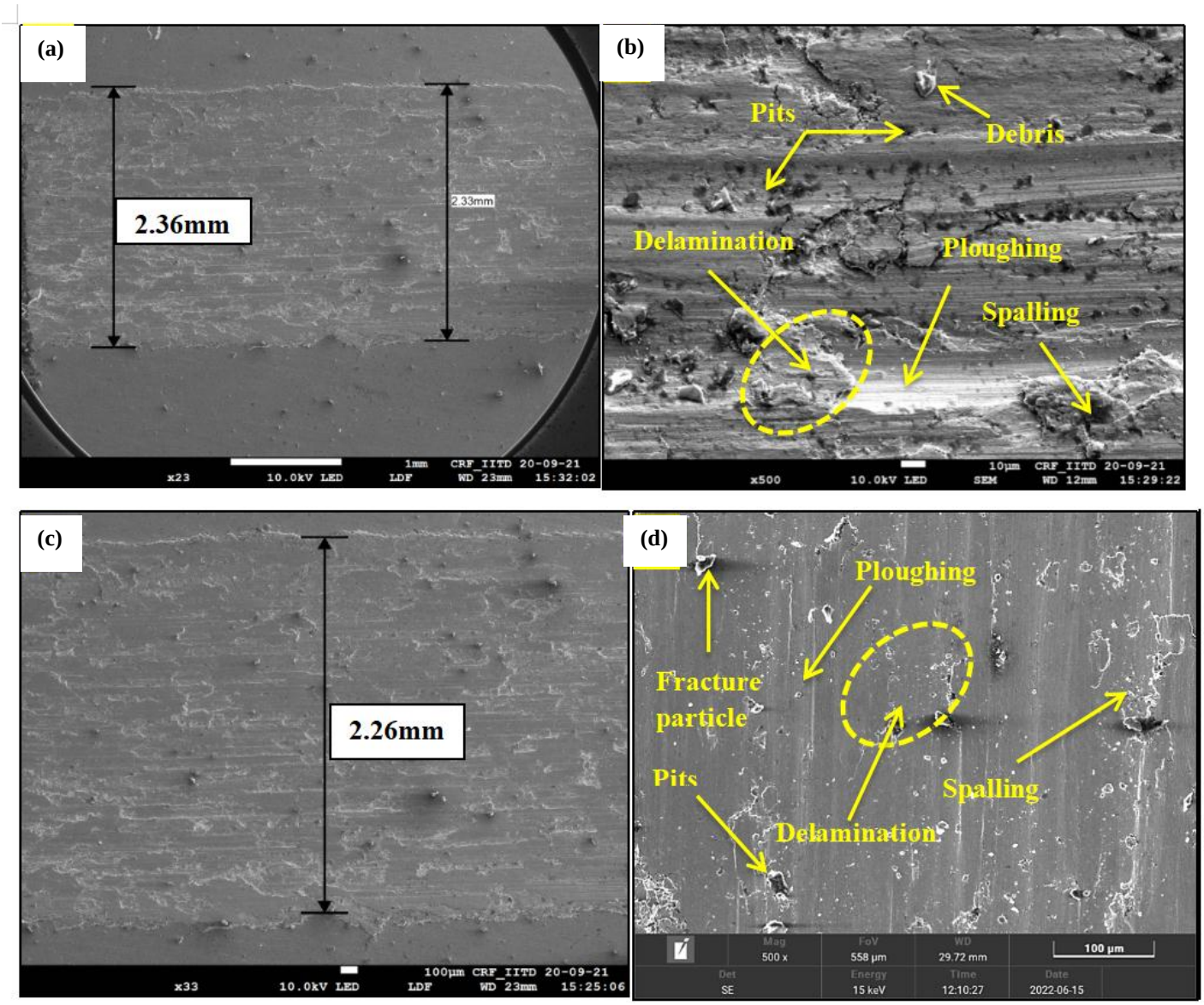

Fig. 4.22 FESEM micrograph of worn surface (a & b) Base material (c & d) Clad surface

The martensite peak is absent before the wear test. However, martensite was found in the XRD patterns of the worn-out surface because austenitic stainless steel is metastable due to a strain-induced transformation rather than a diffusion transformation, and plastic deformation converts austenite to martensite. The austenitic stainless steel martensitic transition is very prone to deformation. In austenitic stainless steel, lower sliding velocities

encourage sliding wear dominated by plasticity [38]. Material transference, plastic deformation, adhesion, and mechanical mixing comprise the wear mechanism dominated by plasticity and adhesive wear, which can compete with metallic particle oxidation at extremely low sliding speeds.

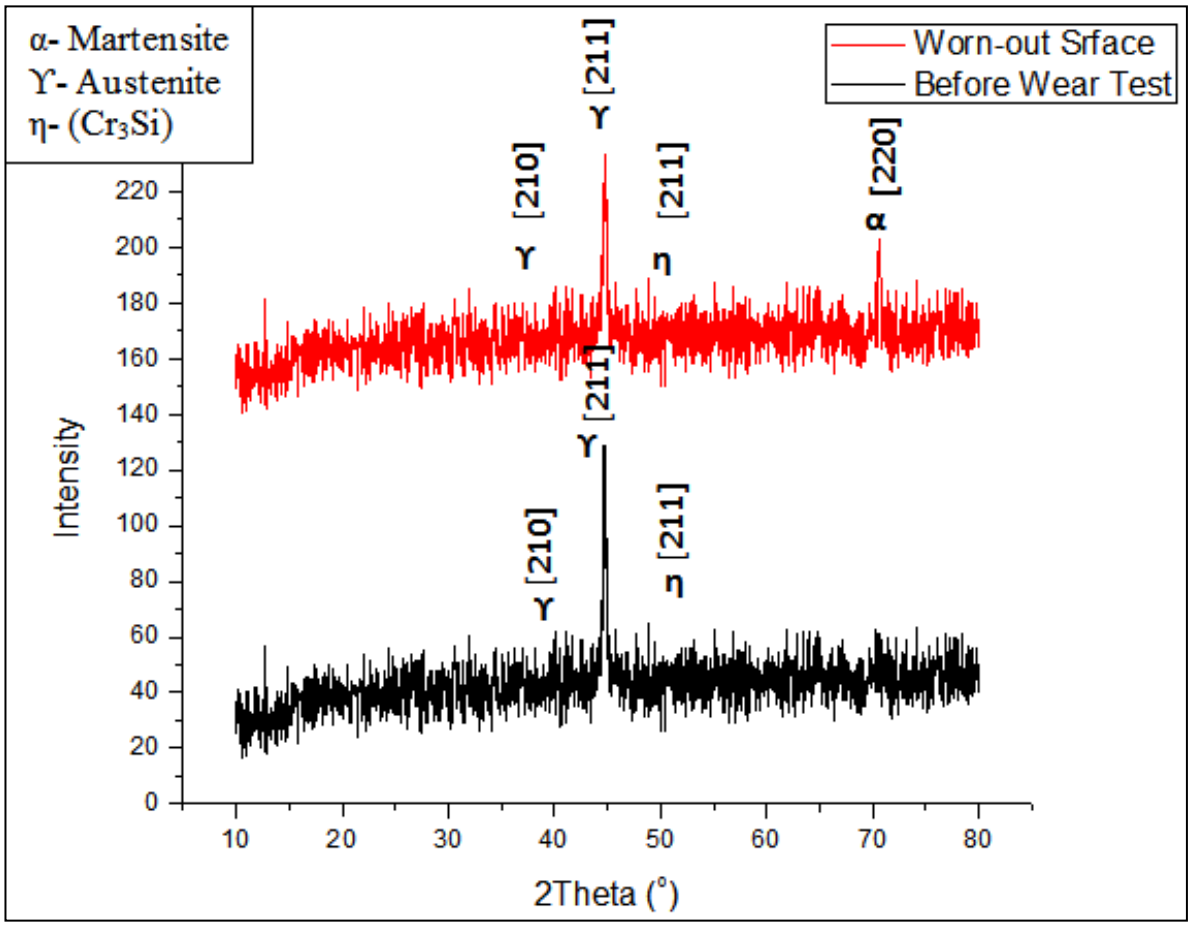

Fig. 4.23 XRD plot of wear track before and after wear test

(a) Effect of Load on COF and Wear rate

Fig. 4.24 shows the typical plot of COF as a time function at different loads, and Fig 4.25 shows the wear rate variations applied at different loads of clad surface. The COF trend suddenly increases as all loads' sliding time is raised from 0 to 60 sec. The COF gradually

gets stable as the sliding time is increased. The increase in wear rate decrease in the contact area between friction pairs compared to the counterpart [Rajkumar et al., (2020)]. As the applied load increases, an increase in wear rate is observed. Also, COF increases when the normal load increases, as seen in Fig. 4.24. It is stated that an increase in surface roughness and the introduction of significant amounts of wear debris account for the rise in friction with an increase in normal load [Bhushan & Kulkarni, (1996), Godse et al., (2016)]. Similar results are obtained for the SS 420, which is compatible with the findings of [M. K. Gupta et al., (2023)], in that the COF increases on increasing normal load. Fig. 4.25 shows that the wear rate increases with increasing the load.

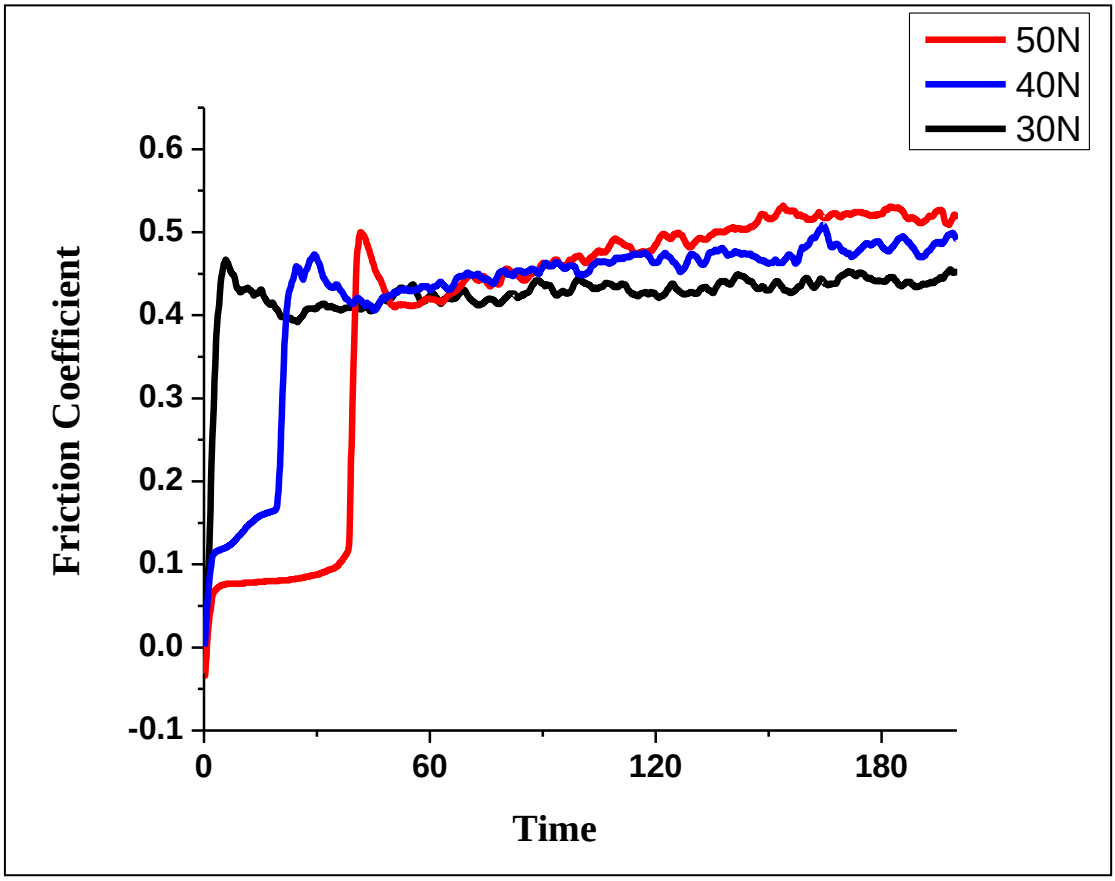

Fig. 4.24 COF as a time function at different loads (5 Hz frequency)

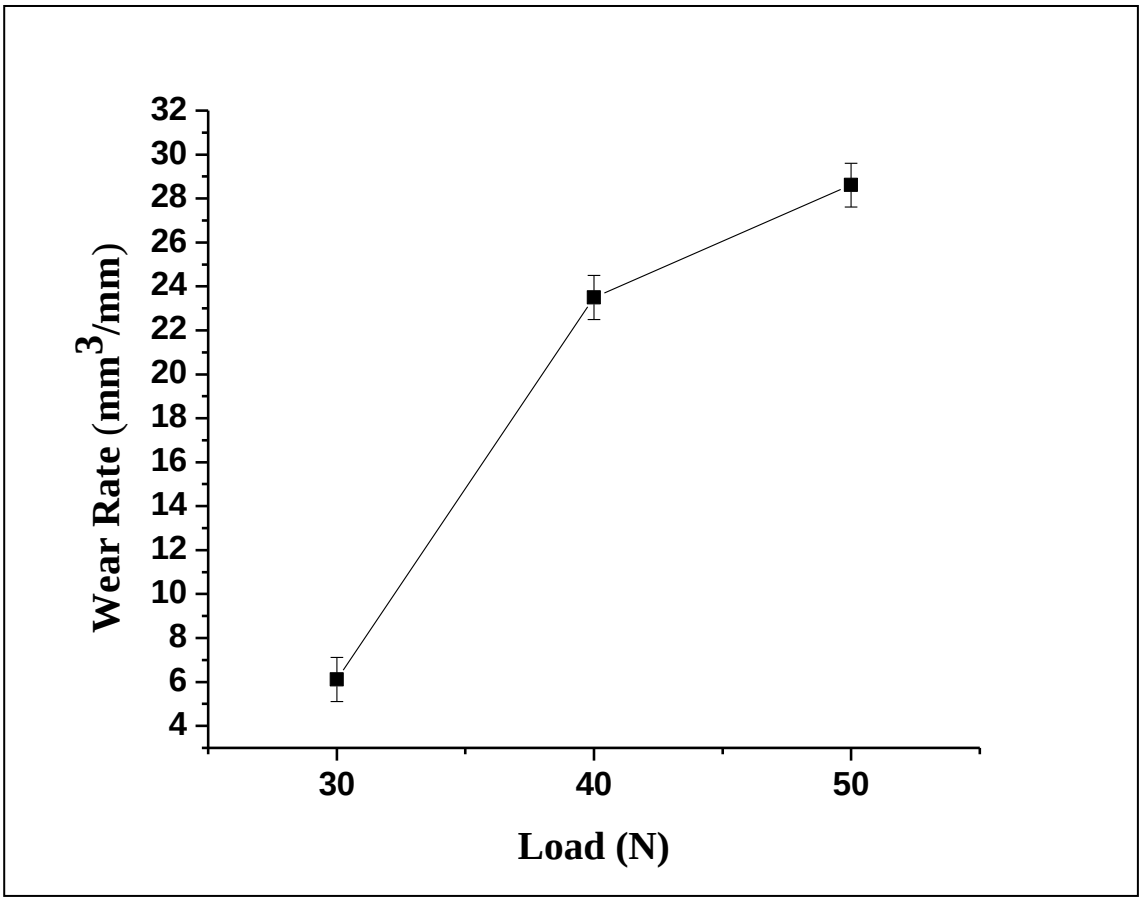

Fig. 4.25 Wear rate variation with the different loads (5 Hz frequency)

The wear rate increases to 28.61 (mm^3/m) from 6.114 (mm^3/m) on increasing load from 30N to 50N. As the load increases, the actual contact area approaches the nominal contact area, increasing the frictional force between the two surfaces. The increasing surface causes higher wear in contact and frictional force. This shows that when the applied load increases, the shear force and frictional thrust rise, increasing the wear rate. [Chowdhury & Helali, (2007a)] noted similar traits of variation for low carbon steel couples, i.e., wear rate rises with a rise in normal load. Fig. 4.26 (a) shows the FESEM micrographs of the wear track obtained at 40N and 5Hz. The occurrence of tiny oxide particle agglomerates at the lowest

frequency indicates that metallic particles have oxidized [Stott, 1998)]. Due to the large exposed surface, the metallic pieces remaining at the contact can break up to very tiny size and oxidizes quickly. The heat deformation speeds up oxidation, and the energy increase brought on by the surface energy and defect density increases. The surface oxidation resulting from the particles' agglomeration may shield them from further wear loss [Stott, (1998)]. Various works have reported that austenitic stainless steels experience oxide development during sliding wear [Smith, (1986)]. At 40 N load the debris was created by bigger metallic particles with various morphologies, including uneven multilayered structures plates and spherical or cylindrical forms, which is seen in Fig. 4.26 (b & c). This implies that initially separated irregular plate-shaped particles were plastically distorted and rolled to produce spherical or cylindrical debris when held within the contact. Uneven plates may crack into smaller pieces that are distorted, rolled up, or shattered [Farias et al., (2007)]. Fig. 4.26 shows the FESEM micrographs and EDS Plot of the sample's wear track obtained at 50N and 5Hz. Fewer oxides are formed at higher loads, and adhesive and abrasive wear processes were observed. Many wear particles are detached from the surface when the load and frequency increase. Due to the increased resistance of the debris to being caught, disintegrated, and oxidized to create the protective layer, the wear rate may be increased.

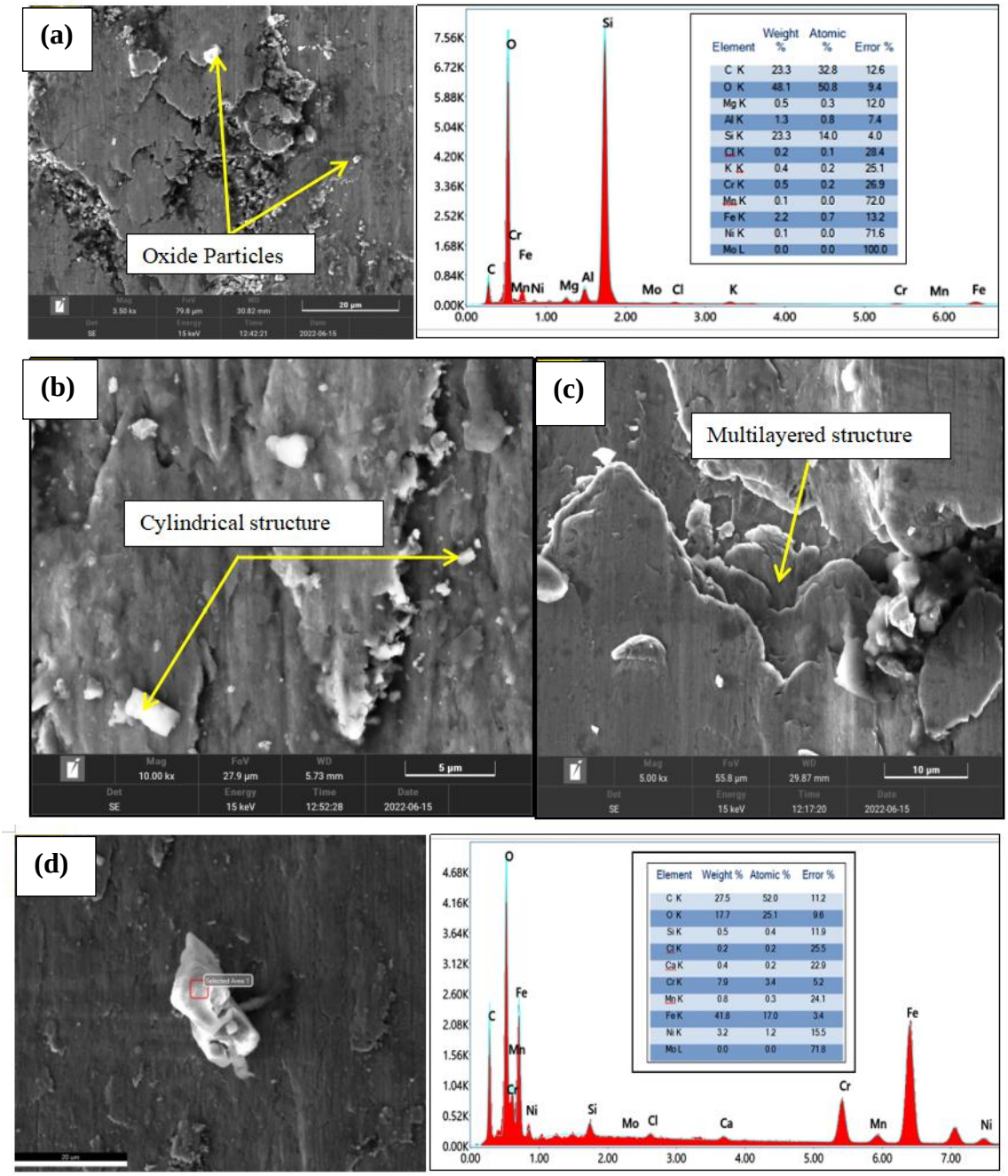

Fig. 4.26 (a) FESEM and EDS Plot of sample wear track obtained at 40N and 5Hz. (b) Wear Particles of clad surface exhibiting cylindrical forms (40 N load and 15 Hz frequency) (c) Clad Surface revealing a multilayered structure (50N Load 15Hz frequency) (d) FESEM and EDS Plot of wear surface at 50N and 5 Hz

(b) Effect of Frequency on COF and Wear rate

Fig. 4.27 shows the COF graph as a time function at a different frequency, and Fig. 4.28 shows the wear rate variation with the various applied frequency. It is observed from Fig. 4.27 that the COF trend suddenly increases for all frequencies as the sliding time is raised from 0 to 60 sec and further gradually gets stable as the sliding time increases.

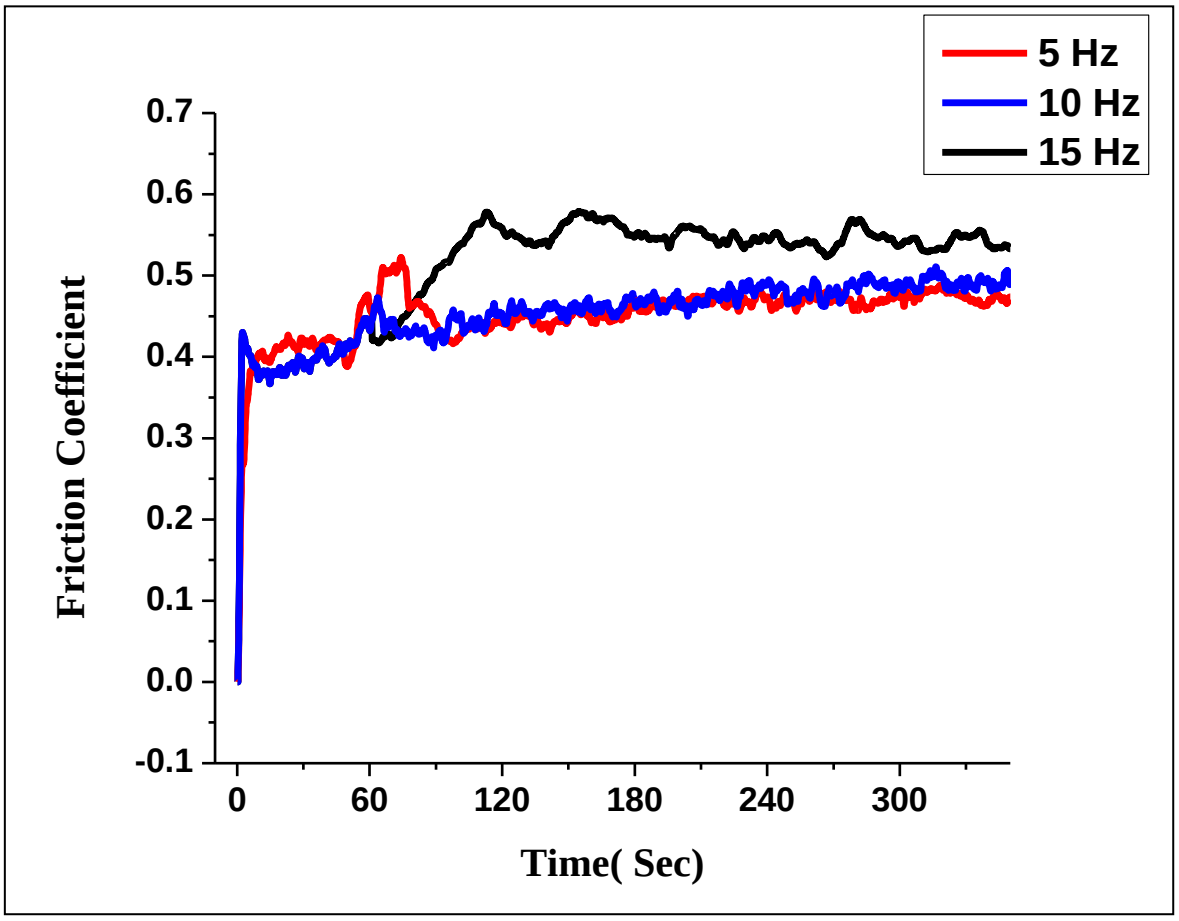

Fig. 4.27 COF as a function of time at different frequencies (40 N load)

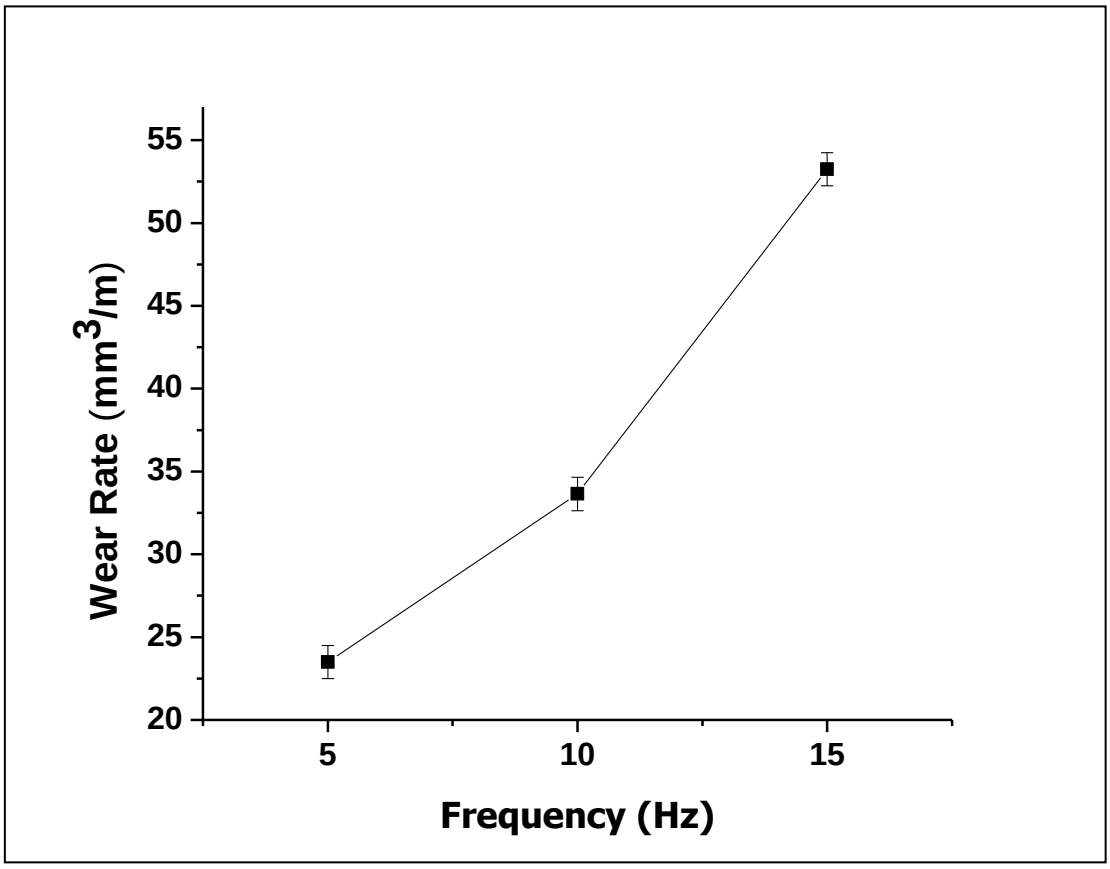

Fig. 4.28 wear rate variation with the variation of frequency (40 N load)

The COF increases with an increase in frequency (5Hz to 15 Hz) because sliding contact between two materials, causing heat to be generated at the asperities, which raises the temperature [Bartolomeu et al., (2017)]. The adherence of the detachable clad surface material to the ball increases the COF with increasing frequency. The variations in wear rate with frequency are shown in Fig. 4.28. Wear rates increase from 23.50 mm^3/m to 53.24 mm^3/m when the frequency increases between 5Hz and 15Hz. When the frequency increases, many wear particles become detached from the surface. The wear rate increased because of the greater resistance of the particles to being captured, disintegrated, and oxidized to form the protective layer. Even if the rubbing duration is constant for all sliding

speeds, the rubbing length increases with increasing frequency. The increased wear rate at high frequency is due to the larger contact area between contacting surfaces and the material's lower shear strength [Bartolomeu et al., (2017)].

4.3 SUMMARY

This chapter provide details about the bead-on-plate experimentation. Low carbon steel is a base plate on which the 2507 super duplex stainless-steel bead-on-plate experiment is performed. Influence of process parameters on dilution and bead geometry (i.e., bead width, bead height, depth of penetration) is discussed in detail. This chapter also covers the optimization of bead-on-plate experiments utilizing CCFCD in RSM and microstructural changes with regard to the process parameters. The best parameters i.e. 200 A of welding current, 4.64 mm/s of welding speed, and 14 mm of NTD are determined, and a validation test is also conducted. Further, CMT cladding process of austenitic stainless steel over mild steel plate and wear analysis of clad 308L stainless at different welding speeds is discussed. A ball-on-disc reciprocating tribometer was used to examine the wear characteristics of the cladding surface by varying the normal loads and frequencies. Results show that the wear rate varies with applied Load and Frequency due to the metastability of austenitic stainless steel during plastic deformation; the austenite change into martensite, and the wear resistance of the cladding surface is enhanced by 30- 40% compared to a base material.

CHAPTER 5

RESULTS AND DISCUSSIONS ON COMPARATIVE STUDY OF CMT AND PULSE MIG WELD CLADDING PROCESS

5.1 INTRODUCTION

Weld Cladding technique is a convenient and economical route for altering the characteristics of the surface layer of the material. In the weld cladding process, minimum dilution with good metallurgical bonding takes place with the base material [Gupta & Sharma, (2014)]. The MIG process is an economical and convenient method for cladding stainless steel on low-carbon steel due to its superior quality, higher deposition rate, high efficiency, high reliability, and absence of fluxes. When the MIG process is used for the cladding of thin plates, the heat input is quite high, resulting in high dilution levels. As the substrate thickness decreases, the degree of dilution of the clad layer increases and then burns through the entire substrate, and as a result, it proved challenging to generate a good cladding layer with minimal dilution on a thin substrate [Chen et al., (2019)]. To solve this problem, a fusion welding procedure with minimal heat input and higher efficiency is desired. The CMT is a modified form of the MIG welding process with explicit low heat input and process control for the parent metal without compromising the quality of the metallurgical bond between the substrate and the coating [Lee et al., (2005)].

[Evangeline & Sathiya, (2019a)] studied the cladding of Inconel 625 over 316L SS using the CMT process method and reported that the clad region near the substrate and interface region shows better corrosion resistance and higher hardness owing to the emergence of equiaxed dendrites and the presence of more Cr and Ni particles. Similarly, [Lorenzin & Rutili, (2009)] reported that CMT cladding of Inconel 625 over 316L SS has a higher deposition rate in comparison with the MIG process. Benoit et al., (2015) compared MIG, Pulsed MIG, CMT, and TIG for the cladding of ER5356 over the Al6061 plate and reported that Pulsed MIG and CMT mix produces a better-quality clad bead than TIG and MIG processes. [Liang et al., (2017)] investigated the cladding of ER4043 over Al6061 plates using TIG-CMT hybrid welding. The TIG current influences the dilution rate and contact angle, which enhance the wettability of the molten metal and result in higher hardness.

5.2 STUDY OF WELD BEAD GEOMETRY AND MECHANICAL CHARACTERIZATION

A Schematic diagram of weld bead dimensions is shown in Fig. 5.1. The estimation of dilution is given in equation 5.1.

$$\text{Dilution} = \frac{\text{Ap}}{(\text{Ap} + \text{Ar})} \tag{5.1}$$

Whereas, Ap = Area of Penetration, Ar = Area of Reinforcement [Koli et al., (2019)]

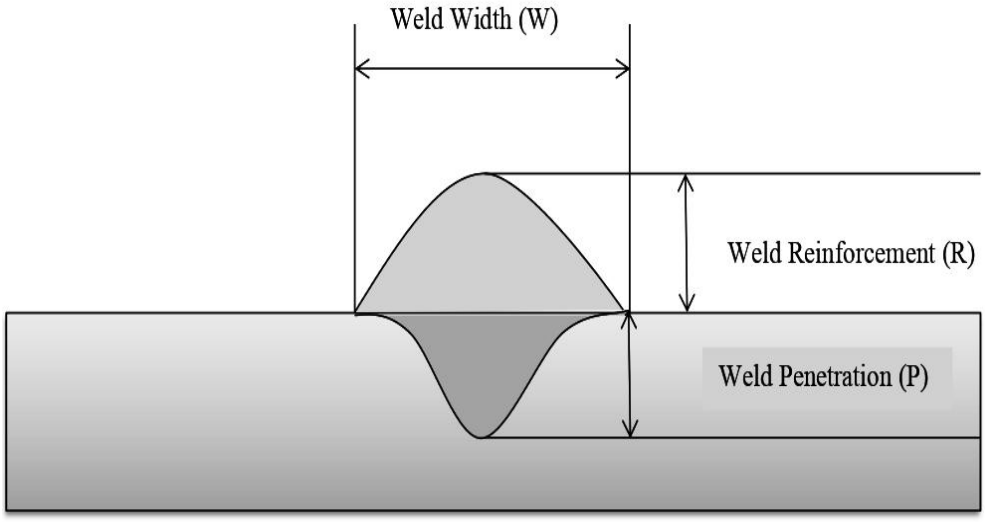

Fig. 5.1 Schematic diagram of weld bead

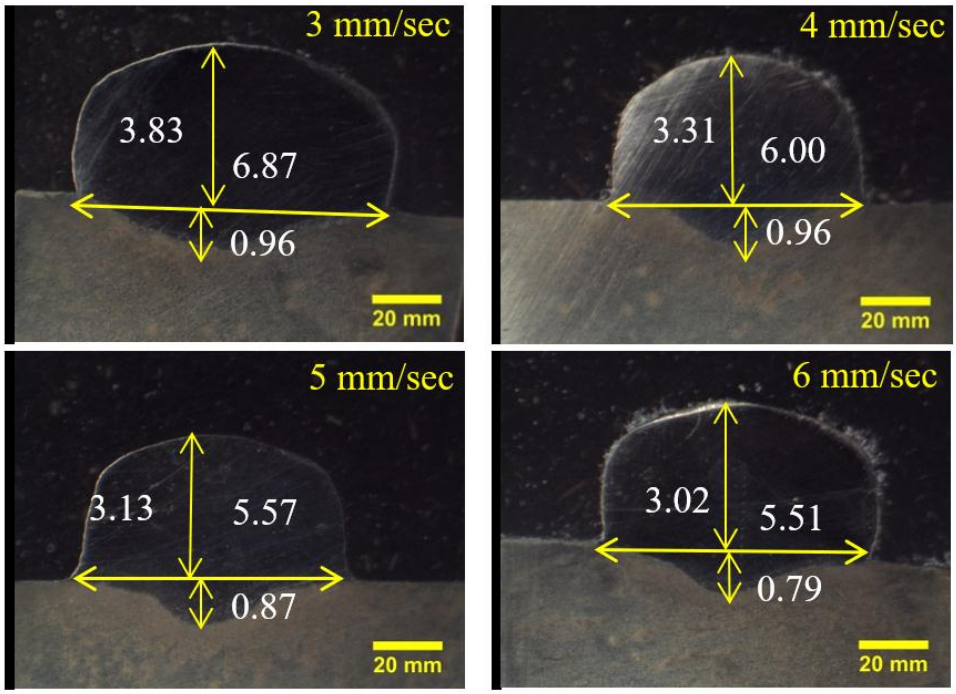

Fig. 5.2 CMT weld on bead samples macro-images

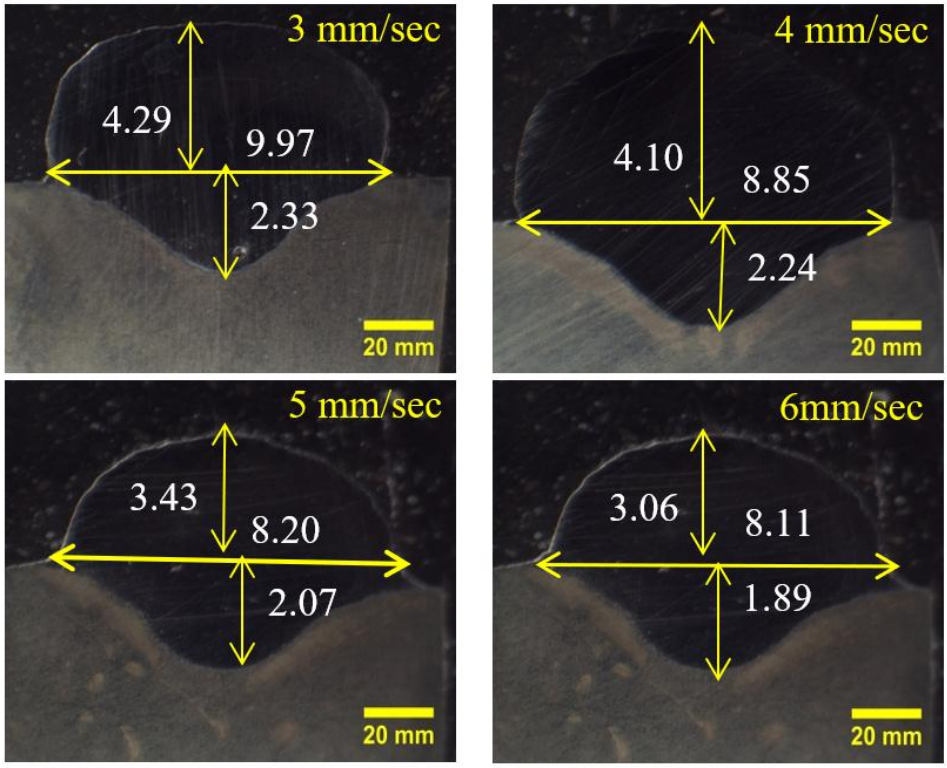

Fig. 5.3 Pulse MIG weld on bead samples macro-images

Heat input of the CMT and Pulse MIG samples are calculated using equation (5.2).

$$Q = \eta \frac{VI}{S} \tag{5.2}$$

Where Q = heat input (J/mm), I = current (A), V = voltage, S = welding speed (mm/sec), and η = efficiency (%). Welding has an average thermal efficiency of about 80% [Devendranath Ramkumar et al., (2015)]. The Pulse MIG and CMT weld bead samples were performed at different welding parameters, and their results are exhibited in Table 5.1. CMT and Pulse MIG weld bead sample macro images are shown in Fig. 5.2 and 5.3, respectively. At lower welding speeds, larger-size weld beads with flatter and smoother surfaces are produced. When welding speed increases, a lower heat input occurs as a result

of the decrease in depth of penetration, bead width, and reinforcement. The CMT weld bead size is 30-35% smaller, and the depth of penetration is 50-58% lower than Pulse MIG welding. The quantity of deposited metal per unit length reduces as the welding speed increases over a long distance. Further, the amount of heat input per unit length is also reduced, and the beads become thinner and narrower.

Table 5.1: Welding parameters and their results of Pulse MIG and CMT weld bead samples

S.No.	Wire feed Rate (m/min)	Welding Speed (mm/sec)	Heat Input (J/mm)	Bead Width (mm)	Bead Height (mm)	Depth of penetration (mm)	% Dilution
Pulse MIG							
1.	6	3	1003.3	9.97	4.29	2.33	24.6
2.	6	4	752.5	8.85	4.10	2.24	23.6
3.	6	5	602	8.20	3.43	2.07	23.5
4.	6	6	501.6	8.11	3.06	1.89	22.4
CMT							
1.	6.5	3	630	6.87	3.83	1.96	10.6
2.	6.5	4	472.5	6.00	3.31	0.96	9.7
3.	6.5	5	378	5.57	3.13	0.87	8.6
4.	6.5	6	315	5.51	3.02	0.79	7.09

5.3 EFFECT OF WELDING SPEED ON HEAT INPUT AND DILUTION (%)

For fabricating a sound joint with high strength and limiting the size of HAZ, less dilution and less heat input are required [Om & Pandey, (2013)]. Heat input and dilution are directly proportional to the formation of the weld beads. When the heat input increases, more substrate metal melts, resulting in an increase in dilution. The effect of welding speed on percentage of dilution and heat input is shown in Fig. 5.4 and 5.5. With an increase in welding speed, a decrease in dilution percentage was observed in both the CMT and Pulse MIG processes. At lower welding speeds, a higher amount of heat input generates on the substrate material, causing to more melting and deeper encroachment occurs. [Saha et al., (2019)] reported that higher heat input results in a broader weld bead without change in reinforcing or penetration of stainless-steel cladding over low-carbon steel by the MIG process. In the CMT process, approximately 60% lesser dilution takes place than in pulse MIG due to the wire moving in an oscillatory motion, which aids in dilution control by keeping the arc length constant. It is the more stable method in terms of heat input and dilution, as it did not show any considerable variation in the output [Koli et al., (2019)].

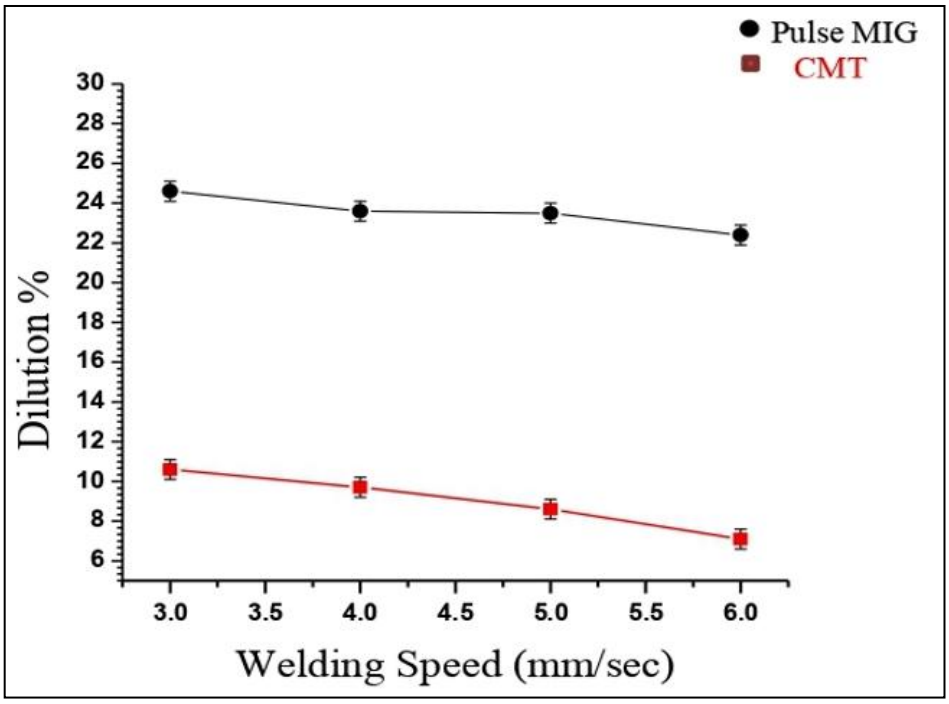

Fig. 5.4 Effect of welding speed of Pulse MIG and CMT welding process on dilution (%)

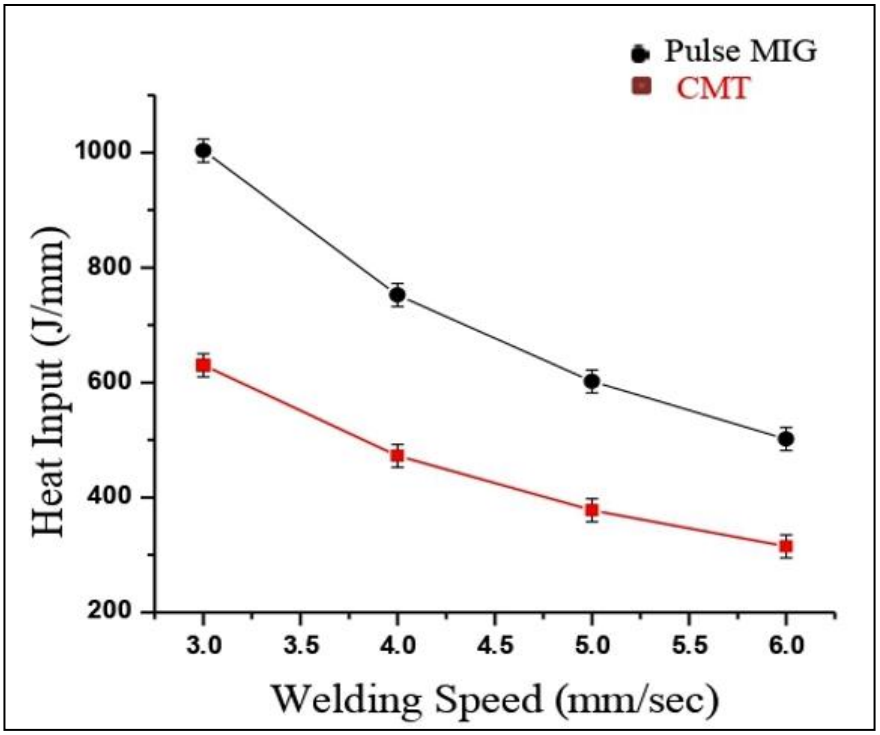

Fig. 5.5 Effect of welding speed of Pulse MIG and CMT welding process on heat input

5.4 MICROSTRUCTURAL ANALYSIS

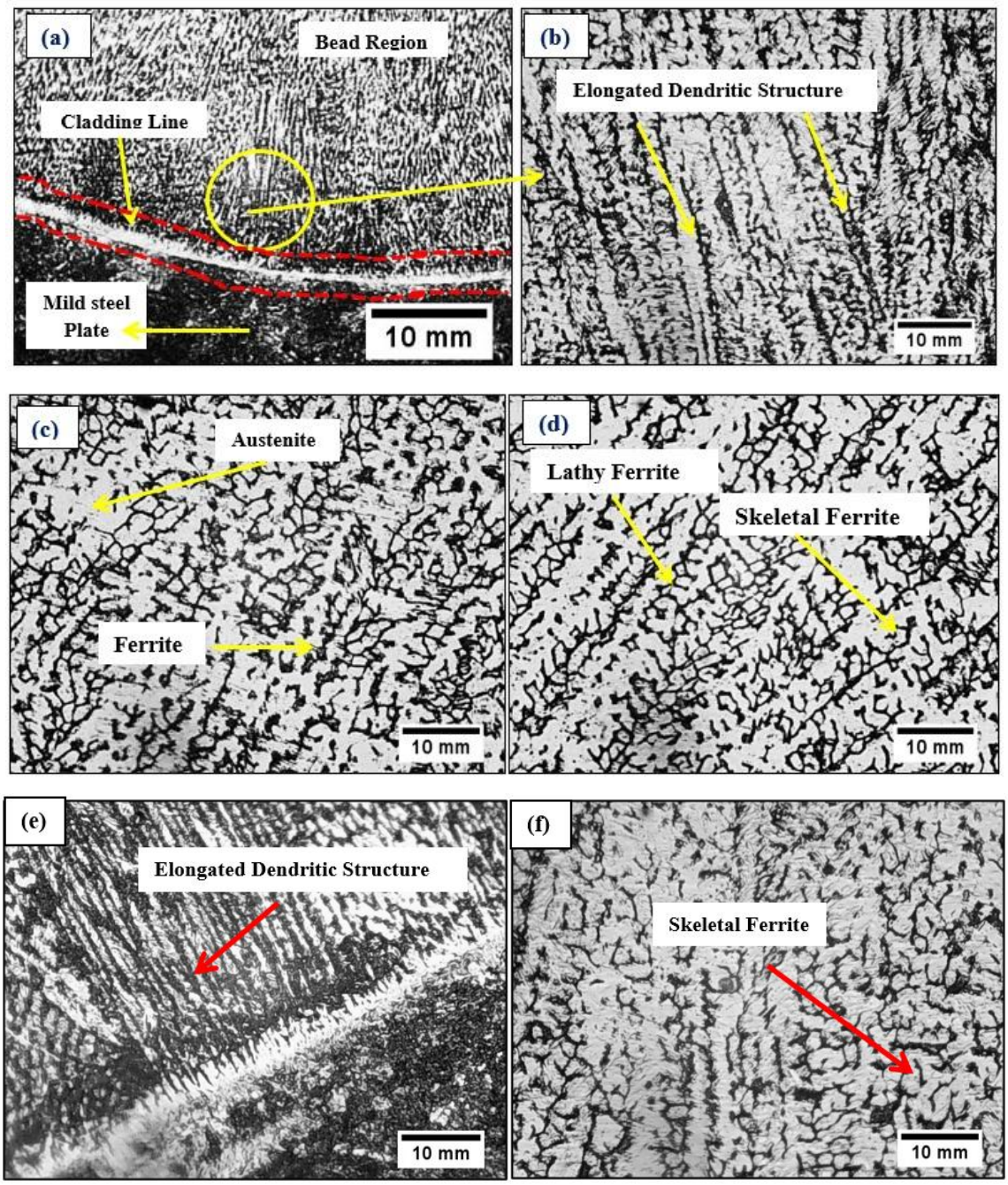

Fig. 5.6 (a) Stainless-steel clad bead on low carbon steel (b) HAZ of CMT (c) & (d) CMT clad bead region (e) HAZ of Pulse MIG (f) Pulse MIG clad bead region

In Fig. 5.6 (a), the base material and weld bead region are separated by a narrow width band called a cladding line. Fig. 5.6 (b) shows the HAZ, and Fig. (c) and (d) shows the clad bead region of the CMT sample. The ferritic phase in the base metal region and the deformed austenitic layers are formed in the clad region. At the clad interface, substitutional diffusion of atoms occurs, which is seen in microstructural images. Near the HAZ, as illustrated in Fig. 5.6 (b), there is no shifting of austenitic structure towards the base metal region due to the sharp diffusion of Ni particles. At the boundary region, the carbide precipitation takes place rapidly due to the lower content of Cr and Ni particles. Fig. 5.7 displays FESEM images with EDX plots in the dilution region and clad bead region. In the clad region, δ-ferrite has 8–13% of volume, γ-austenite is having 85–90% of volume, while micro-inclusions are < 1% nearer to the fusion boundary. The ferritic phase in the base metal region and the deformed austenitic layers are formed in the clad region [Koli et al., (2022)]. At the clad interface, substitutional diffusion of atoms occurs, which is seen in microstructural images. Near the HAZ, as illustrated in Fig. 5.6 (b), there is no shifting of austenitic structure towards the base metal region due to the sharp diffusion of Ni particles. At the boundary region, the carbide precipitation takes place rapidly due to the lower content of Cr and Ni particles. When the Cr content is high, the concentration of δ-ferrite is high, and when the Ni content is high, the concentration γ-austenite is high. The intensity of γ-austenite is greater at low heat input than a high heat input. As a result of the ferrite-austenite method of solidification, the γ -austenite content % decreases as the heat input increases. Heat input is critical for phase distribution in δ-ferrite morphologies. In the boundary region and HAZ of CMT samples exhibited in Fig. 5.7 (a), the carbide

precipitation occurs due to less content of Cr and Ni particles, as shown in Fig. 5.7 (b). The cladding region consists of austenite without carbide precipitation. During the solidification of clad material, there will be the development of dendrites in the dilution region, which can be seen in Fig. 5.7 (c). Fig. 5.7 (d) shows more liquated cracks in a clad bead region of the Pulse MIG sample due to high heat input. As the gradient of temperature rises, the columnar dendrites grow perpendicular to the clad center. The larger inter-dendrite spacing and increase in dendrite length arise in the weld bead. [Wang et al., (2018)] observed the formation of dendrite phases in HAZ of 309L steel cladding on low alloy steel. The austenite matrix formed two distinct types of lathy ferrite and skeletal ferrite structure. In all weld bead samples, similar types of ferrite morphologies are observed in the dilution region. The different cooling rates and thermal cycles in the dilution region are responsible for this phenomenon. Different cooling rates have resulted in different types of ferrite transformation, changing the ferrite morphology within the weld bead. Skeletal ferrite morphology has formed where cooling rates were moderate, as illustrated in Fig. 5.6 (d). The austenite consumes the ferrite until it is sufficiently depleted in austenite-promoting elements, like nickel, and enriched in ferrite-promoting elements, like chromium, to be stable at low temperatures with limited diffusion. However, lathy ferrite morphology formed where cooling rates were high due to limited diffusion during the austenite-ferrite transformation. While cooling of weld material in the clad region, the lathy ferrite structure was formed owing to the morphological instability of the interphase boundary during the diffusion-controlled transition of ferrite to austenite. A similar type of result was observed in the cladding of stainless steel with high strength low alloy steel through the arc welding

process by various researchers [Wang et al., (2018), Ul-Hamid et al., (2005), Mvola et al., (2016)]. [Inoue et al., (2000)] investigated the formation mechanism of lathy ferrite in austenitic stainless steel of weld metals and observed that total ferrite (i.e., lathy and skeletal ferrite) content rises when Cr and Ni ratios rise, but the percentage of lathy ferrite to total ferrite does not change considerably. The formation of dendritic structure near HAZ was increased in Pulse MIG samples. The skeletal ferrite was formed and the lathy ferrite was reduced in the clad bead region of Pulse MIG samples due to increased heat input, which can be seen from fig. 5.6 (e) and 5.6 (f). Fig. 5.7 (e), (f), (g), and (h) illustrate the EDX plot near the clad bead region and dilution region of CMT and Pulse MIG samples, respectively. The XRD pattern of CMT and MIG pulse samples taken at the clad region is shown in Fig. 5.7 (i). The XRD spectrum peak of 308L SS wire consists of Fe_7C_3, Cr_3Si and Cr_2Si peaks. The lower intensity of austenite peaks was observed in the Pulse MIG samples. The filler material solidifies faster into the base material, and the ferrite phase is transformed into the austenite phase in the clad region (V. Kumar & Singh, 2012). Some of the ferrite phases are retained in the dilution region, which is seen in the XRD pattern. In the clad region, a higher number of Cr-enriched peaks was observed, which is confirmed by the EDX plot.

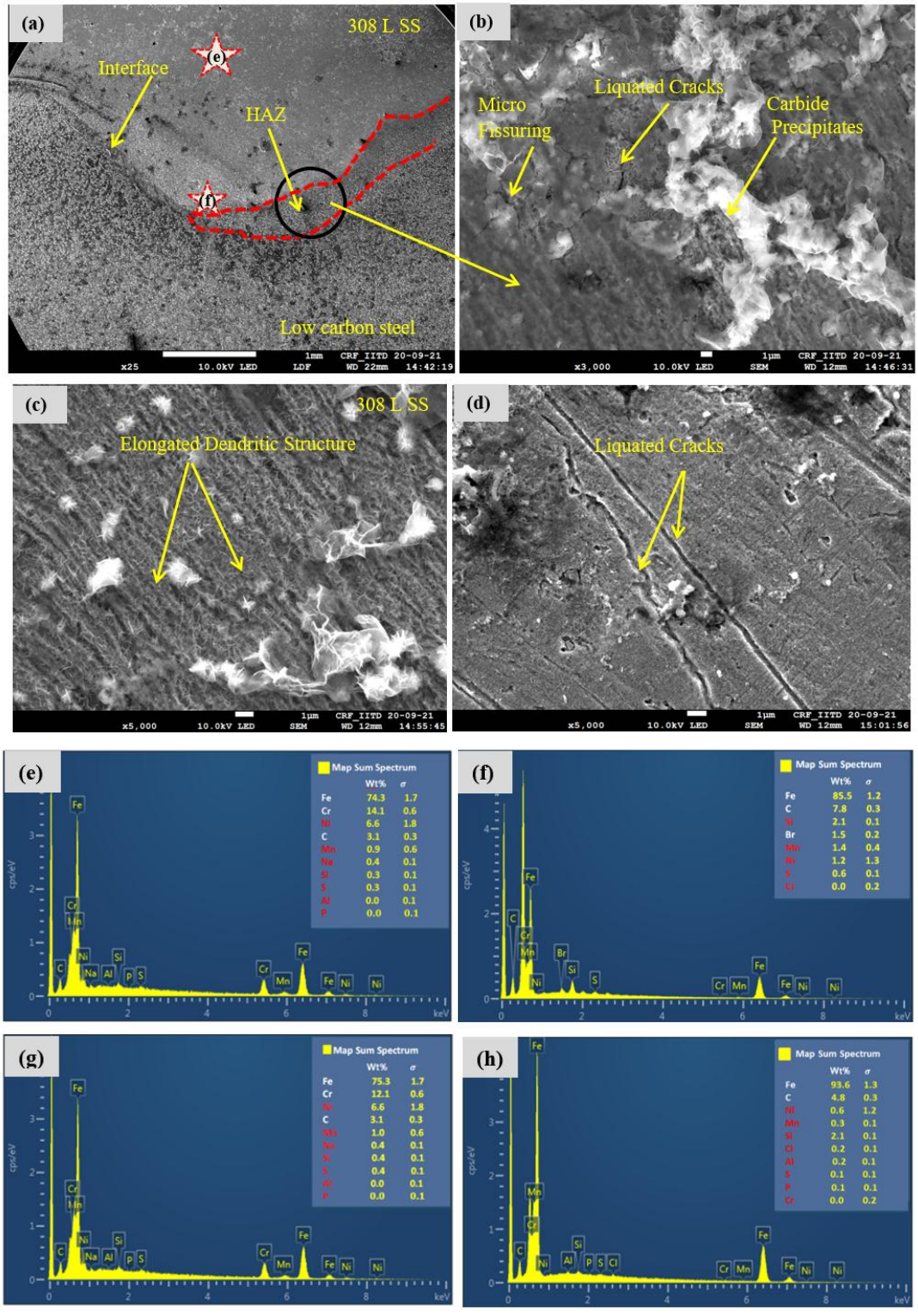
(a)
308 L SS
Interface
HAZ
Low carbon steel
(b)
Micro Fissuring
Liquated Cracks
Carbide Precipitates
(c)
308 L SS
Elongated Dendritic Structure
(d)
Liquated Cracks
(e)
Map Sum Spectrum
Wt% σ
Fe 74.3 1.7
Cr 14.1 0.6
Ni 6.6 1.8
C 3.1 0.3
Mn 0.9 0.6
Na 0.4 0.1
Si 0.3 0.1
S 0.3 0.1
Al 0.0 0.1
P 0.0 0.1
(f)
Map Sum Spectrum
Wt% σ
Fe 85.5 1.2
C 7.8 0.3
Si 2.1 0.1
Br 1.5 0.2
Mn 1.4 0.4
Ni 1.2 1.3
S 0.6 0.1
Cl 0.0 0.2
(g)
Map Sum Spectrum
Wt% σ
Fe 75.3 1.7
Cr 12.1 0.6
Ni 6.6 1.8
C 3.1 0.3
Mn 1.0 0.6
Na 0.4 0.1
Si 0.4 0.1
S 0.4 0.1
Al 0.0 0.1
P 0.0 0.1
(h)
Map Sum Spectrum
Wt% σ
Fe 93.6 1.3
C 4.8 0.3
Ni 0.6 1.2
Mn 0.3 0.1
Si 2.1 0.1
Cl 0.2 0.1
Al 0.2 0.1
S 0.1 0.1
P 0.1 0.1
Cr 0.0 0.2

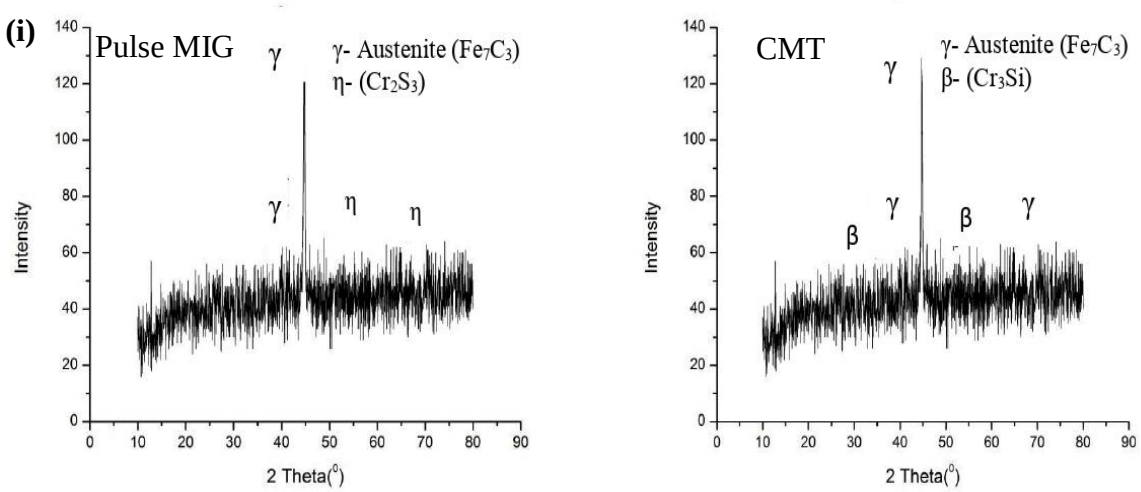

Fig. 5.7 FESEM images (a) Stainless-steel CMT clad on low carbon steel plate (b) HAZ (c) CMT sample clad bead region (d) Pulse MIG sample clad bead region (e) EDX plot near clad bead region of CMT sample (f) EDX plot near dilution region of CMT sample (g) EDX plot near clad bead region of Pulse MIG sample (h) EDX plot near dilution region of Pulse MIG sample (i) XRD images of Clad region

5.5 MICRO-HARDNESS

The micro-hardness of weld-clad samples measured transversely is shown in Fig. 5.8 (a). A higher microhardness was observed on the top surface of the clad bead and gradually decreased as the indenter approached the centre of the dilution region, which is owing to a higher cooling rate on the clad bead surface. The high hardness of the dilution boundary region in the clad beads is caused by the presence of partially unmelted grains, which are partly introduced as nuclei by the clad bead's new precipitating phase during the solidification stage. The HAZ shows a decreasing trend in microhardness. The area adjacent to the dilution region experiences relatively slow cooling rates, resulting in coarse-

grained microstructure, while the area adjacent to the base metal experiences higher thermal gradients [S. Kumar & Shahi, (2011)]. These microhardness studies show that hardness increases in the order of unaffected base metal, heat-affected region, and clad bead region due to the variability of microstructure, as shown in Fig.5.6. The FWHM (full width half maximum) of clad samples is measured using the X-ray diffraction method. The FWHM alpha angle profiles and graphs are shown in Fig. 5.8 (b) and (c). FWHM is the distance between the points on the y-axis that correspond to half of the maximum amplitude in a spectral curve. The FWHM values vs. CMT and Pulse MIG samples produced at various welding speeds are exhibited in Fig. 5.8 (d). At higher welding speeds, produced clad samples have thicker residual peaks and higher FWHM values, which result in improved micro-hardness. FWHM values and micro-hardness have a linear relationship with each other. [Fu et al., (2018)] reported that there is a direct relationship between FWHM and the microhardness of GCr15 steel processed by the triple shot peening method.

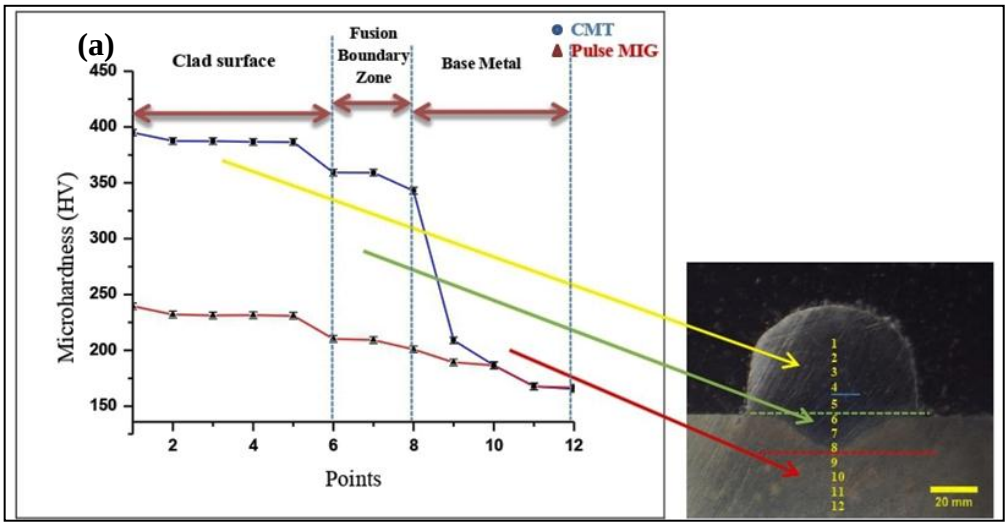

Fig.5.8 (a) Micro-hardness of Pulse MIG and CMT weld clad samples (current of 175A & 6 mm/sec welding speed)

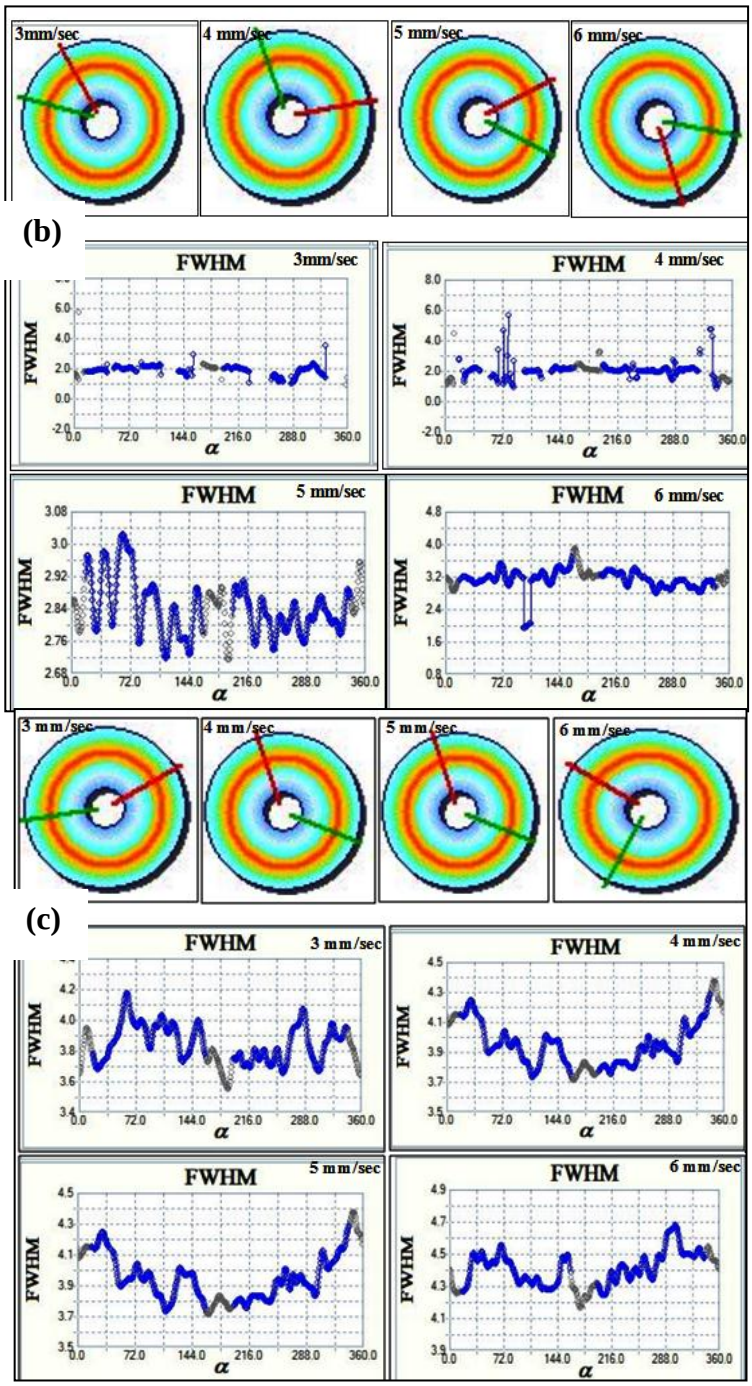

Fig.5.8 (b) FWHM alpha angle and FWHM graph at Different welding speed of Pulse MIG (c) CMT

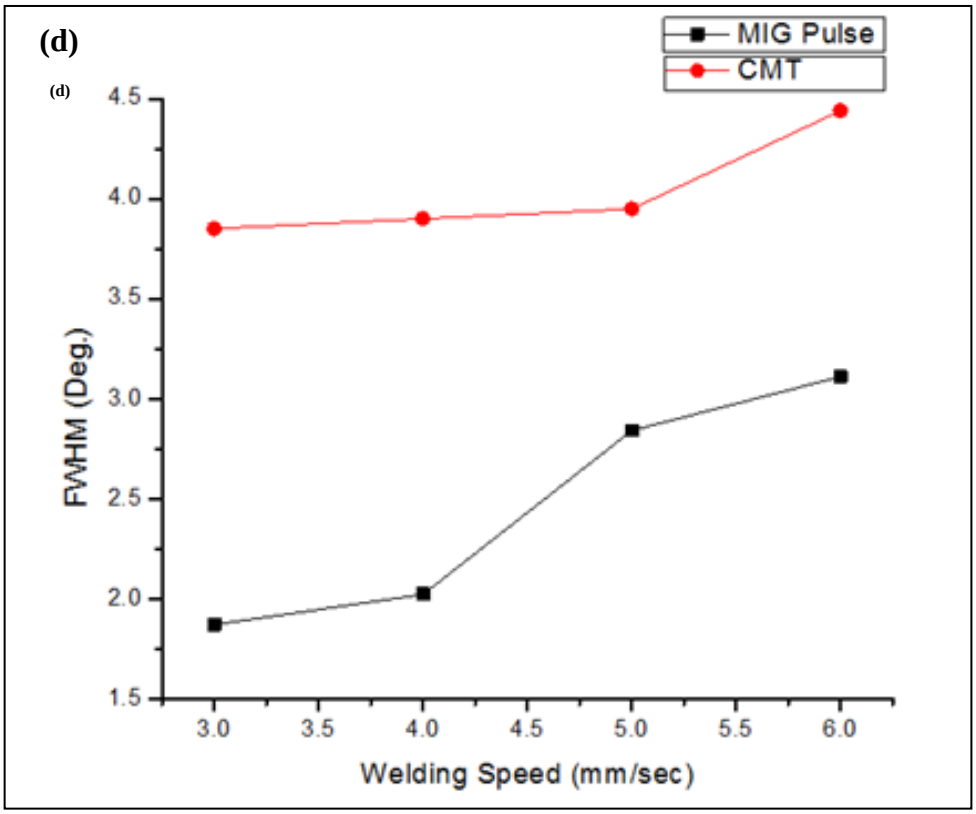

Fig.5.8 (d) FWHM values vs. CMT and Pulse MIG samples produced at different welding speed

5.6 RESIDUAL STRESS

Residual stresses persist within a material after manufacturing and processing in the absence of external pressures or heat gradients. [Fu et al., (2018)] Residual stress profiles were taken at three different regions, i.e., clad region, the dilution region, and the base plate of clad samples, as shown in Fig. 5.9. It has been observed that clad material produces different compressive residual stress values at different welding speeds. The residual stress is of the compressive type, which aids in reducing surface cracks and prevents mechanical failure. The compressive stresses are increased to enhance the fatigue behavior of the

mechanical components. Higher compressive stresses are also not recommended since they degrade the grain structure of the material [Koli et al., (2019)].

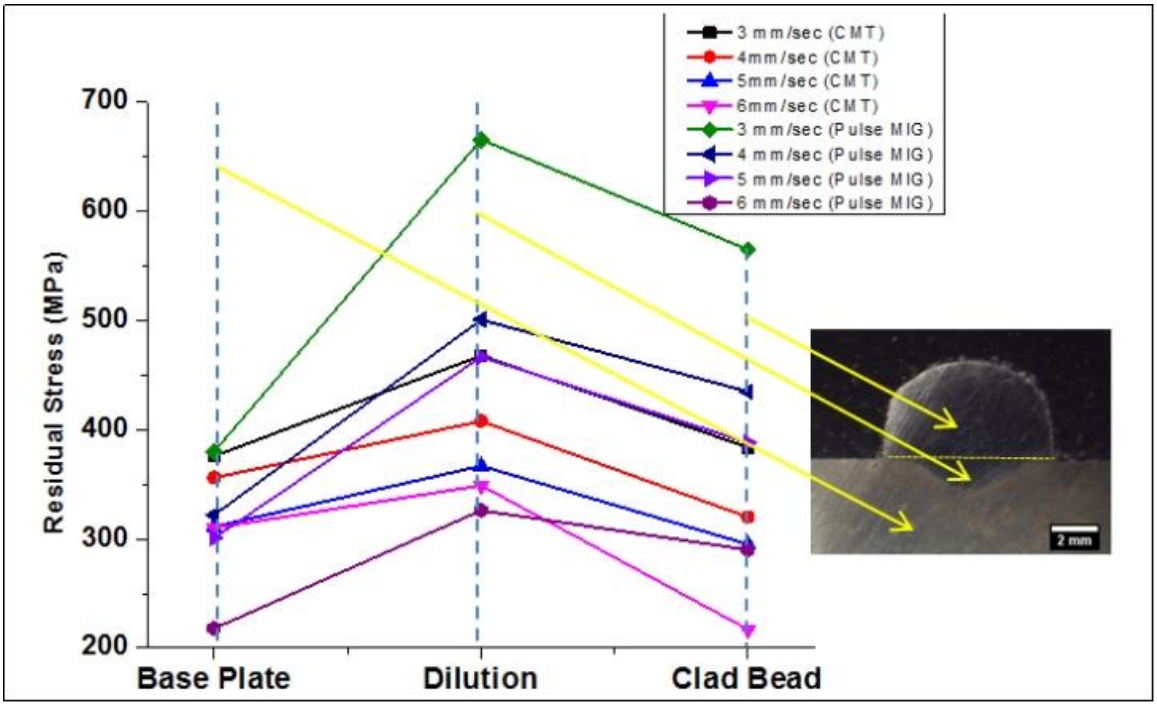

Fig. 5.9 Residual stress at different region at various welding speeds

The clad sample prepared at 6mm/sec has lower residual stresses due to higher hardness and enhanced microstructural properties. CMT samples have 30-50% lower residual stresses than Pulse MIG samples. Fig. 5.10 shows the 3D Debye ring, distortion, and profile curve taken in the dilution region of clad samples of Pulse MIG and CMT welded at 175A current and 6 mm/sec welding speed.

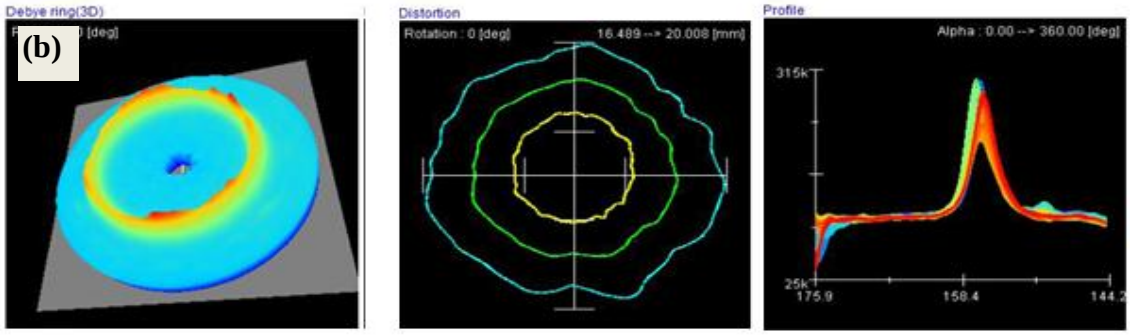

Pulse MIG

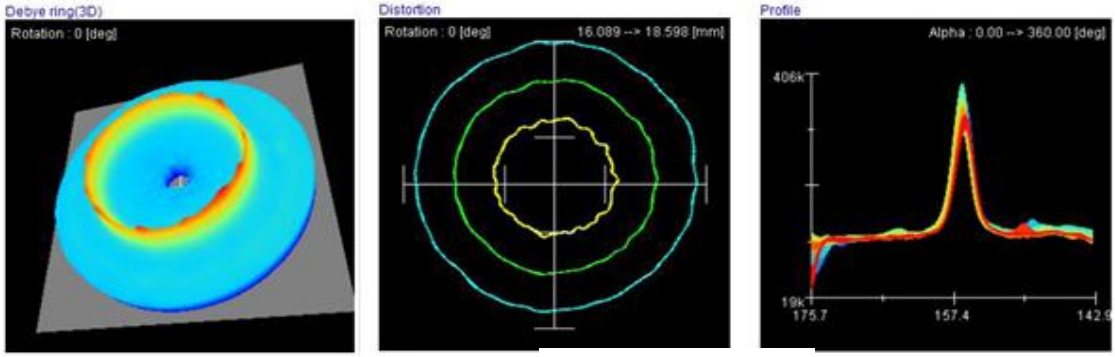

CMT

Fig. 5.10 Debye ring, residual stress profile and distortion curve at dilution region of Pulse MIG and CMT

5.7 WEAR PROPERTIES

Wear test disk sizes of 20mm x20mm were take-out from the middle of the CMT and Pulse MIG cladded surface by wire EDM, as shown in Fig. 5.11. After performing the wear test, it was observed that the wear rate (30.63 mm^3/m) of the 308 L SS cladded surface using CMT is lower than the base material wear rate (53.24 mm^3/m) due to the higher hardness of the surface, which is seen in the hardness profile. Several researchers reported that the steel powder coating surface has higher wear resistance than the base material due to its higher hardness [Zhou et al., (2020), (Ermakova et al., (2022)].

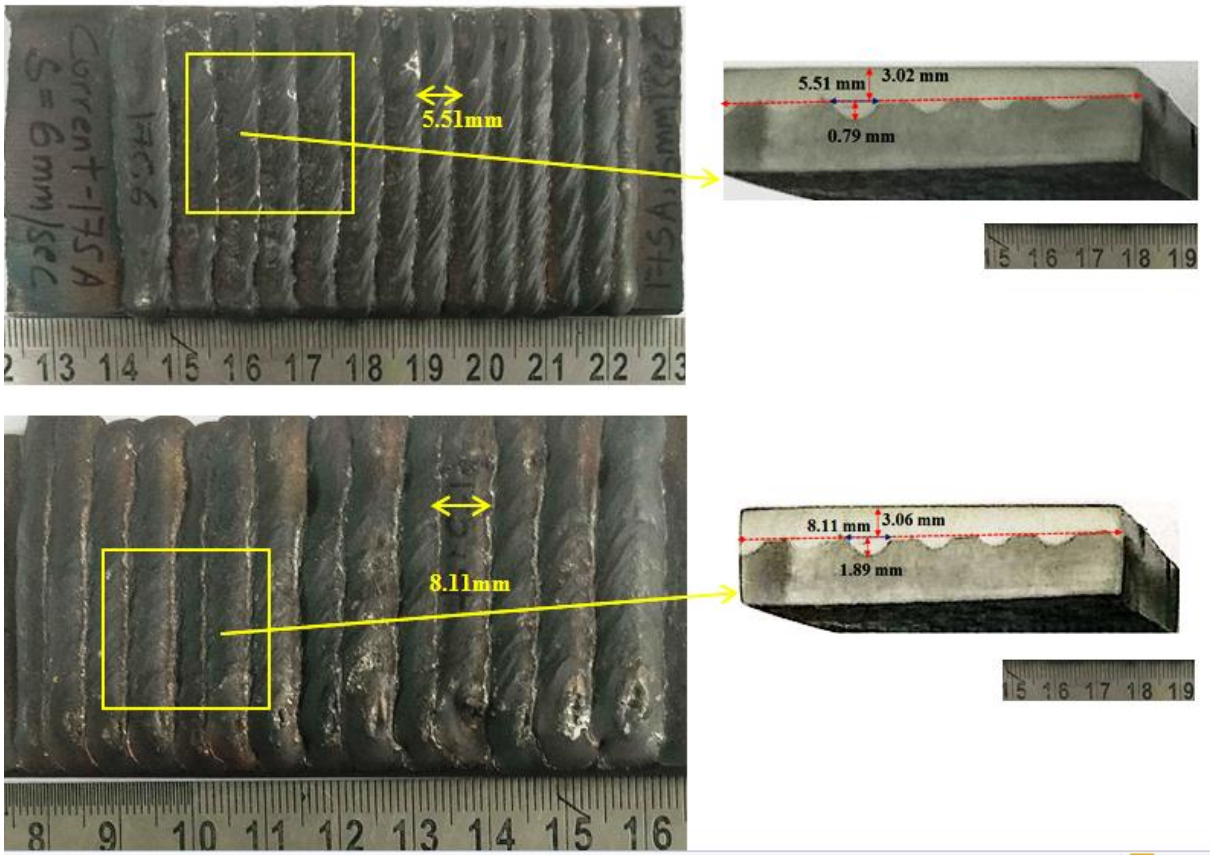

Fig. 5.11 CMT and Pulse MIG cladded sample's cross section extracted for wear test

The variation of coefficient of friction with sliding time for CMT and Pulse MIG processed wear test samples is shown in Fig. 5.12. An increase in wear rate is observed at the start of the experiment with a load of 40 N and a frequency of 10 Hz at all welding speeds. The decrease in the actual area of contact of the friction pair in comparison to its nominal counterpart is the cause of the increase in abrasives on the worn surface. Asperities flake off the surface during wear testing, and the wear rate increases. After a 60 seconds start, the wear rate decreases gradually as the sliding time increases [Sun et al., (2008)]. The hard phases in the 308L clad bead act as a protective layer during wear tests, which improves

low-carbon steel wear resistance. The friction coefficient of the CMT cladding surface is less than that of the base material. A hard surface often has a lower coefficient of friction, because it creates less contact area when a constant force is applied [Chowdhury & Helali, (2007)]. The wear rate of the clad sample prepared by CMT is lower than the Pulse MIG clad sample wear rate (43.23 mm3/m) due to lesser dilution and low heat input. In addition, CMT samples clad surface has a higher microhardness which results in improved wear resistance [Koli et al., (2019)]. As per Archard's wear relationship, higher hardness surface has higher wear resistance.

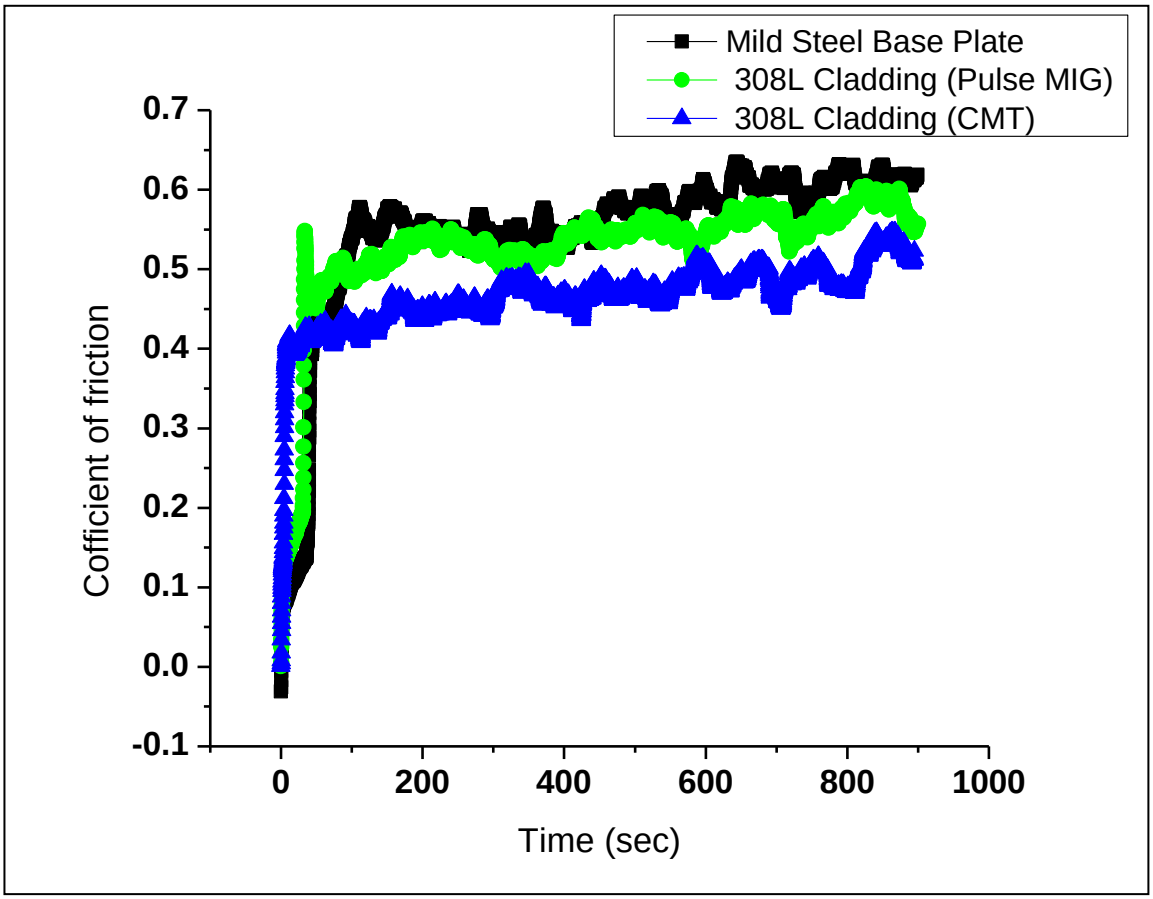

Fig. 5.12. Coefficient of friction behaviour of cladded surface and base material

The wear behaviour of the wear samples is examined through FESEM and EDS analysis. Fig. 5.13 shows the EDS spectrum and FESEM micrograph of the base material, CMT and Pulse MIG cladded surface. From Fig. 5.13, it is observed that the wear track width of the base material is larger than the cladded surface produced by both the processes i.e., CMT and Pulse MIG, and wear debris is observed on the wear surface along the sliding direction. It may be the contact surface area with a hard counter ball is lesser than the base material due to the higher hardness of the surface. The primary mechanism responsible for the wearing action is of an abrasive nature. Wearing time increases the depth of oxidative wear and changes the worn surface morphology. The worn surface of the base alloy comprised micro-pits, micro-cracks, ploughing, and spallation of the surfaces. Ploughs appear as a result of abrasive particles that become detached while wearing. In the base material, oxidation, abrasive severe plastic deformation, and delamination wear mechanisms are observed. The Pulse MIG cladded surface has mild oxidation and abrasive wear with a lesser amount of spallation in comparison to the base material but more than the CMT cladded surface, which is seen in the Fig. 5.14.

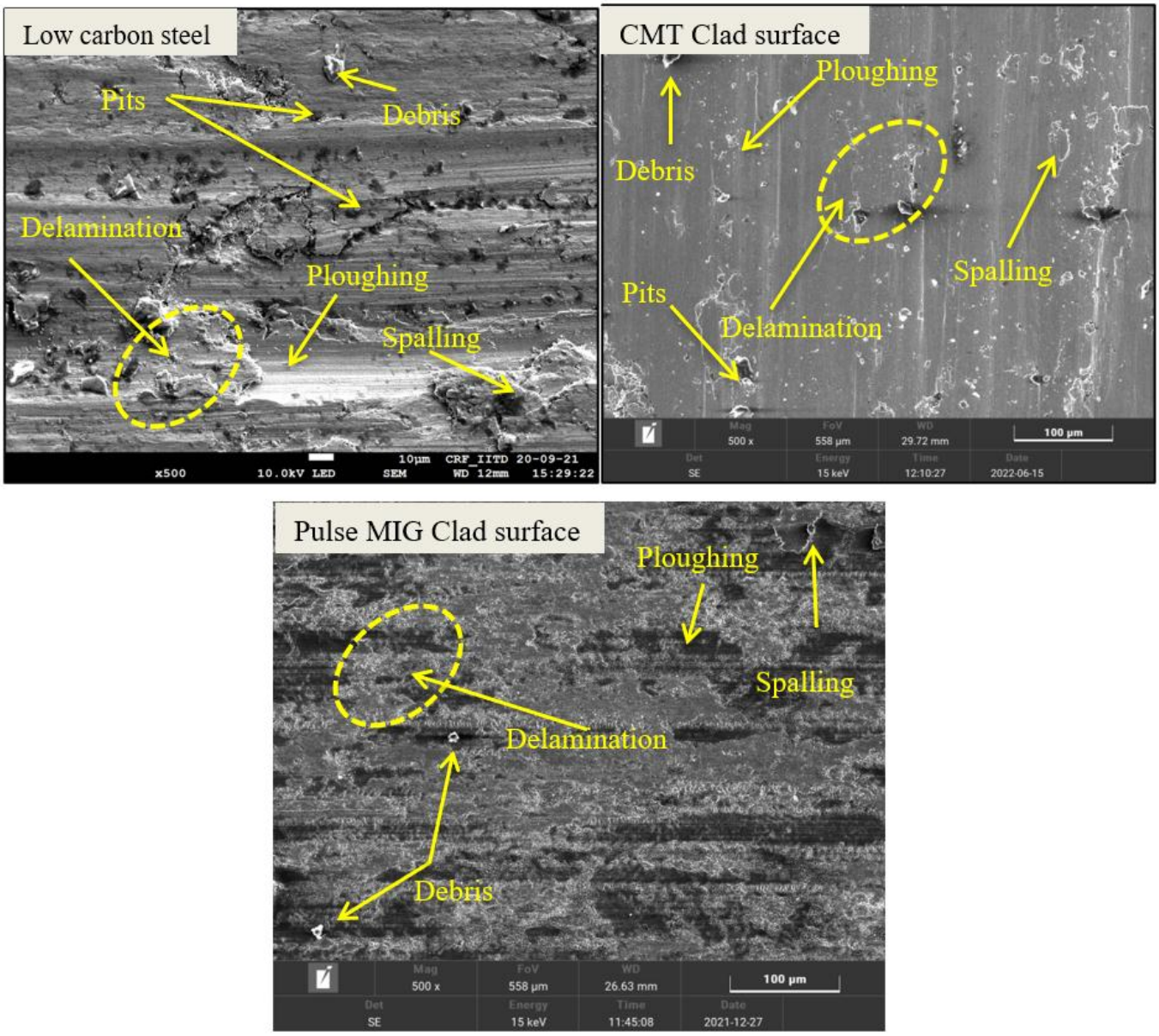

Fig. 5.13. FESEM micrograph of Low carbon steel, CMT Cladded surface and Pulse MIG cladded surface

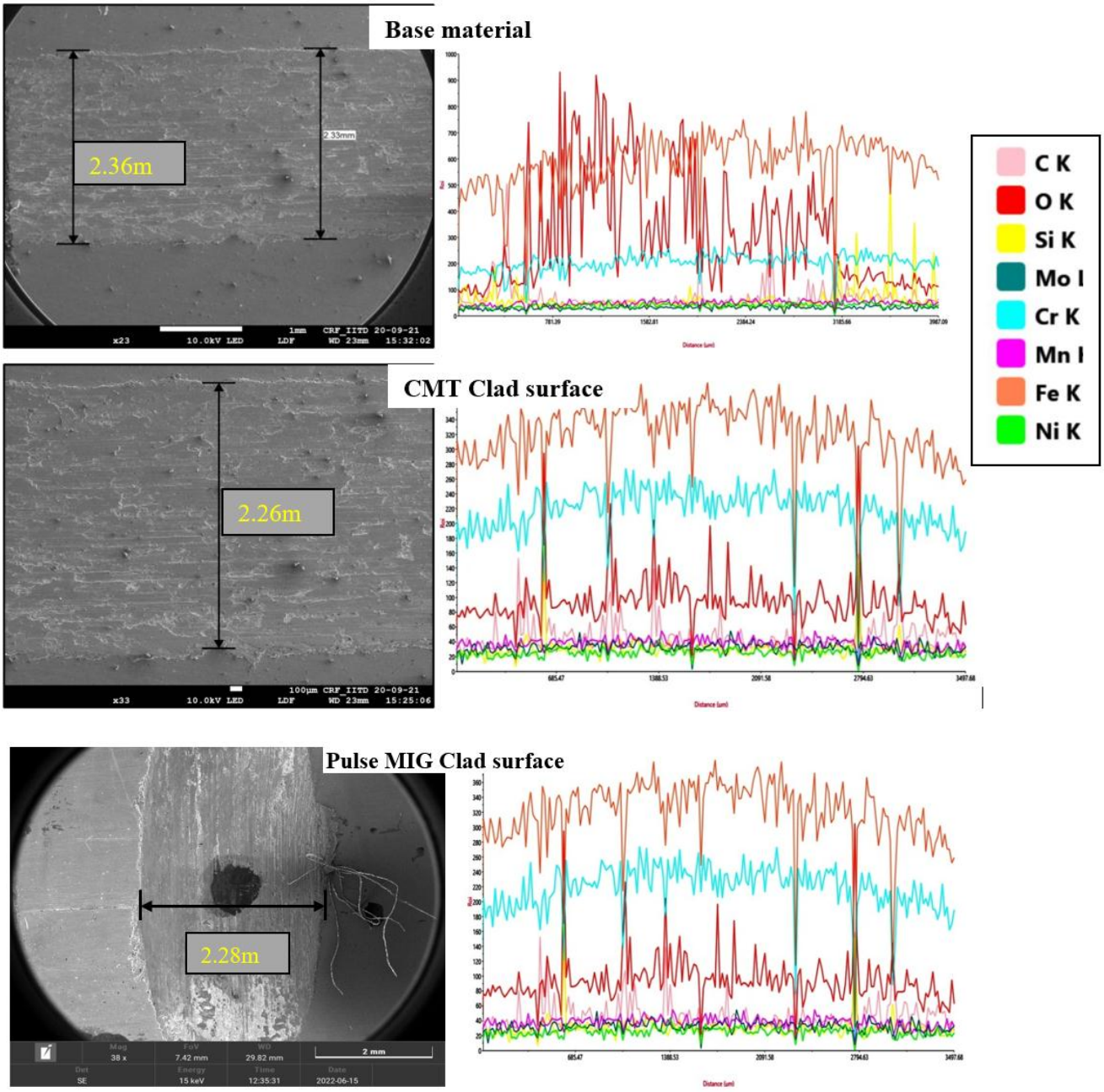

Fig. 5.14. EDS analysis of wear track of low carbon steel, CMT cladded surface and Pulse MIG cladded surface

5.8 SUMMARY

In this chapter the comparative analysis between Cold Metal Transfer (CMT) welding and Pulse MIG welding process is done. The clad bead of 308L SS over low-carbon steel is analyzed using CMT and Pulse MIG techniques. In order to analyse the mechanical and wear properties of CMT clad samples, the welding speed was selected as the input process parameter, while the NTD and shielding gas flow rate were maintained at a constant level. Comparison is based on weld bead dimensions, microstructures, microhardness, and wear behaviour. Results showed that the mechanical and wear properties of the CMT clad surface were significantly enhanced, while the residual stresses were reduced, owing to the low-dilution and decreased heat input.

CHAPTER 6

CONCLUSIONS, SCOPE FOR FUTURE WORK AND SOCIAL IMPACT

6.1 CONCLUSIONS

The key conclusions from the findings and discussions in previous chapters are presented in this chapter.

6.1.1 Optimization of CMT cladding process of super duplex stainless steel on Low carbon steel

1. The weld bead geometry and dilution % are significantly impacted by all three process parameters: welding current, welding speed, and NTD.
2. For Depth of penetration and bead width, welding speed is more dominant parameter (50% and 65.17%) whereas for bead height current is more dominant (88.97%), and for dilution, welding speed is the major influencing parameter, with more than 66.18% contribution.
3. The quadratic model was sufficient to describe and predict the bead geometry and dilution % responses, with the change of independent variables (Current, Welding Speed and NTD). The optimal current, welding speeds and NTD values are 200 A, 4.64 mm/sec, and 14 mm, respectively, with 60% desirability.
4. The re-melting of the adjacent base region produced a greater fraction of ferrite in the dilution region compared to the clad bead region. As the solid-state ferrite phase solidified through the molten metal, it gave rise to several forms of austenite, including GBA, WA, IGA, and PTA.

5. The sample with the optimal parameters has a microhardness of 253.52 ± 5 HV0.5. The hardness increases in the order of unaffected base metal, heat-affected region, and clad bead region due to microstructure variability.
6. The hard phases in the super duplex 2507 clad bead act as a protective layer during wear tests, which improves low-carbon steel wear resistance.

6.1.2 CMT cladding process of austenitic stainless steel on low carbon steel

This research used the CMT technique to examine the wear behaviour of a 308L austenitic stainless steel-clad surface. The following conclusions are drawn by evaluating the results:

1. The CMT technique is a stable process for producing defect-free clad overlay.
2. Welding speed significantly affects wear behaviour and metallurgical and mechanical properties. The low welding speed and high heat input induce low hardness, which causes more plastic deformation than the high welding speed. With an increase in welding speed from 3 mm/sec to 6 mm/sec, the wear rate decreases to 21.66 (mm^3/m) from 30.63 (mm^3/m).
3. COF values within the reported range increase as normal load and frequency increase. In the case of welding speed, COF decreases with increasing welding speed.
4. The wear rate increases from 6.114 (mm^3/m) to 28.61 (mm^3/m), increasing load from 30N to 50N. The wear rate shows a positive trend; as frequency increases, the wear rate increases.

6.1.3 Comparative study of CMT and Pulse MIG weld cladding process

This work addressed the effect of welding parameters on weld-clad bead geometry by CMT and Pulse MIG processes of 308L SS over low-carbon steel. The microhardness and wear

properties of the CMT clad surface were evaluated. The following conclusions were drawn from the experimental results:

1. The CMT weld bead size is 30-35% smaller, and the depth of penetration is 50-58% lower than Pulse MIG welding due to lower heat input and lesser dilution.
2. The CMT welding process is used to produce a 3 mm thick cladding layer in a single pass. This technique is a stable process for producing defect-free clad overlay with 50%-60% lesser dilution than the Pulse MIG process.
3. Clad region microstructure has a deformed austenite structure, and in the HAZ region, carbide precipitation takes place due to the less content of Cr and Ni particles.
4. Welding speeds have a significant effect on mechanical, and wear properties. Clad sample prepared at a welding speed of 6 mm/sec has a higher hardness value of 390 ($HV_{0.5}$) and lower residual stress (compressive) than other clad samples prepared at lower welding speeds. (i.e., 3, 4, and 5 mm/sec.)
5. The wear rate (30.63 mm^3/m) of the clad sample prepared by CMT is lower than the Pulse MIG clad sample wear rate (43.23 mm^3/m). The mechanism of wear observed in abrasive in nature with a lesser amount of spallation.
6. Different combinations of CMT process parameters, i.e., welding speed, the workpiece to nozzle distance, shielding gas flow rate, and arc correction factor on weld-clad bead geometry, need to be explored. In the future scope, ultrasonic assisted CMT processes, magnetic field assisted CMT processes, and nano-ceramic metals added filler wire clad surface might enhance the weld clad properties.

6.2 SCOPE FOR FUTURE WORK

- Various other properties like corrosion, abrasive resistance, cold toughness etc can be studied of the cladded specimen.
- By achieving the correct microstructure of the clad part, both the mechanical qualities and anti-corrosion capabilities can be greatly enhanced in various reactive environments.
- The effect of different combination of process parameters at different levels i.e., gas flow rate, combinations of shielding gases on bead geometry and dilution can be studied.
- Some new developments regarding welding techniques such as Spin arc welding, hybrid techniques, parametric optimization techniques (i.e., genetic algorithm with artificial neural network (ANN)) can be studied.
- Cladding of different grade of stainless steel and its application can be explored.

6.3 SOCIAL IMPACT

CMT cladding provides fast tracked wear protection solutions in the most challenging environment and industries. With growing energy demand and a emphasis on renewable, stainless steel cladding solve the complex industrial corrosion resistant and wear protection challenges by leveraging the latest and leading CMT welding technique. Stainless steel CMT cladding is used in every aspect of our lives; in cars and constructions products, electric appliances, cargo ships and surgical scalpels, by providing improvement of existing ones.

REFERENCES

- Abioye, T. E., McCartney, D. G., & Clare, A. T. (2015). Laser cladding of Inconel 625 wire for corrosion protection. *Journal of Materials Processing Technology*, *217*, 232–240. https://doi.org/10.1016/J.JMATPROTEC.2014.10.024
- Alvarães, C. P., Jorge, J. C. F., Souza, L. F. G. de, Araújo, L. S., Mendes, M. C., & Farneze, H. N. (2020). Microstructure and corrosion properties of single layer Inconel 625 weld cladding obtained by the electroslag welding process. *Journal of Materials Research and Technology*, *9*(6), 16146–16158. https://doi.org/10.1016/J.JMRT.2020.11.048
- Baidridge, T., Poling, G., Foroozmehr, E., Kovacevic, R., Metz, T., Kadekar, V., & Gupta, M. C. (2013). Laser cladding of Inconel 690 on Inconel 600 superalloy for corrosion protection in nuclear applications. *Optics and Lasers in Engineering*, *51*(2), 180–184. https://doi.org/10.1016/j.optlaseng.2012.08.006
- Bartolomeu, F., Buciumeanu, M., Pinto, E., Alves, N., Carvalho, O., Silva, F. S., & Miranda, G. (2017). 316L stainless steel mechanical and tribological behavior—A comparison between selective laser melting, hot pressing and conventional casting. *Additive Manufacturing*, *16*, 81–89. https://doi.org/10.1016/j.addma.2017.05.007
- Benoit, A., Paillard, P., Baudin, T., Klosek, V., & Mottin, J. B. (2015). Comparison of four arc welding processes used for aluminium alloy cladding. *Science and Technology of Welding and Joining*, *20*(1), 75–81. https://doi.org/10.1179/1362171814Y.0000000257
- Bhushan, B., & Kulkarni, A. V. (1996). Effect of normal load on microscale friction measurements. In *Thin Solid Films* (Vol. 278).

- Bloyce, A. (1998). Surface engineering of titanium alloys for wear protection. *Proceedings of the Institution of Mechanical Engineers, Part J: Journal of Engineering Tribology*, *212*(6), 467–476. https://doi.org/10.1243/1350650981542263
- Cao, X., Xiao, M., Jahazi, M., Fournier, J., & Alain, M. (2008). Optimization of processing parameters during laser cladding of ZE41A-T5 magnesium alloy castings using Taguchi method. *Materials and Manufacturing Processes*, *23*(4), 413–418. https://doi.org/10.1080/10426910801940391
- Chakrabarti, B., Das, H., Das, S., & Pal, T. K. (2013). Effect of process parameters on clad quality of duplex stainless steel using GMAW process. *Transactions of the Indian Institute of Metals*, *66*(3), 221–230. https://doi.org/10.1007/s12666-013-0246-x
- Chatterjee, S., & Pal, T. K. (2003). Wear behaviour of hardfacing deposits on cast iron. *Wear*, *255*(1–6), 417–425. https://doi.org/10.1016/S0043-1648(03)00101-7
- Chen, C., Xu, Q., Sun, K., Zhao, J., Zhou, J., & Xue, F. (2019a). Tin-bronze cladding on thin steel sheet by cold metal transfer arc deposition. *Materials Science and Technology (United Kingdom)*, *35*(12), 1526–1529. https://doi.org/10.1080/02670836.2019.1630090
- Chen, C., Xu, Q., Sun, K., Zhao, J., Zhou, J., & Xue, F. (2019b). Tin-bronze cladding on thin steel sheet by cold metal transfer arc deposition. *Materials Science and Technology (United Kingdom)*, *35*(12), 1526–1529. https://doi.org/10.1080/02670836.2019.1630090
- Chen, J. H., Hsieh, C. C., Hua, P. S., Chang, C. M., Lin, C. M., Wu, P. T. Y., & Wu, W. (2013). Microstructure and abrasive wear properties of Fe-Cr-C hardfacing alloy cladding manufactured by Gas Tungsten Arc Welding (GTAW). *Metals and Materials International*, *19*(1), 93–98. https://doi.org/10.1007/s12540-013-1015-4
- Chowdhury, M. A., & Helali, M. M. (2007a). The effect of frequency of vibration and humidity on the wear rate. *Wear*, *262*(1–2), 198–203. https://doi.org/10.1016/J.WEAR.2006.05.007

- Chowdhury, M. A., & Helali, M. M. (2007b). The effect of frequency of vibration and humidity on the wear rate. *Wear*, *262*(1–2), 198–203. https://doi.org/10.1016/j.wear.2006.05.007
- Chuaiphan, W., & Srijaroenpramong, L. (2014). Effect of welding speed on microstructures, mechanical properties and corrosion behavior of GTA-welded AISI 201 stainless steel sheets. *Journal of Materials Processing Technology*, *214*(2), 402–408. https://doi.org/10.1016/j.jmatprotec.2013.09.025
- Davanageri, M., Narendranath, S., & Kadoli, R. (n.d.). A R C H I V E S of F O U N D R Y E N G I N E E R I N G Dry Sliding Wear Behavior of Super Duplex Stainless Steel AISI 2507: A Statistical Approach.
- Devendranath Ramkumar, K., Mishra, D., Ganesh Raj, B., Vignesh, M. K., Thiruvengatam, G., Sudharshan, S. P., Arivazhagan, N., Sivashanmugam, N., & Rabel, A. M. (2015). Effect of optimal weld parameters in the microstructure and mechanical properties of autogeneous gas tungsten arc weldments of super-duplex stainless steel UNS S32750. *Materials and Design*, *66*(PA), 356–365. https://doi.org/10.1016/j.matdes.2014.10.084
- Eghlimi, A., Shamanian, M., & Raeissi, K. (2013). Dilution and ferrite number prediction in pulsed current cladding of super-duplex stainless steel using RSM. *Journal of Materials Engineering and Performance*, *22*(12), 3657–3664. https://doi.org/10.1007/s11665-013-0661-5
- Elemary, B. R. (2019). Evaluation and improvement of promising rubber recycling OT machine using fractional factorial and response surface design. *Communications in Statistics Case Studies Data Analysis and Applications*, *5*(3), 168–188. https://doi.org/10.1080/23737484.2019.1603091
- Ermakova, A., Mehmanparast, A., Ganguly, S., Razavi, J., & Berto, F. (2022). Fatigue crack growth behaviour of wire and arc additively manufactured ER70S-6 low carbon steel components. *International Journal of Fracture*, *235*(1), 47–59. https://doi.org/10.1007/s10704-021-00545-8

- Evangeline, A., & Sathiya, P. (2019a). Cold metal arc transfer (CMT) metal deposition of Inconel 625 superalloy on 316L austenitic stainless steel: Microstructural evaluation, corrosion and wear resistance properties. *Materials Research Express*, *6*(6). https://doi.org/10.1088/2053-1591/ab0a10
- Evangeline, A., & Sathiya, P. (2019b). Dissimilar Cladding of Ni–Cr–Mo Superalloy over 316L Austenitic Stainless Steel: Morphologies and Mechanical Properties. *Metals and Materials International*, *0123456789*. https://doi.org/10.1007/s12540-019-00440-x
- Farias, M. C. M., Souza, R. M., Sinatora, A., & Tanaka, D. K. (2007). The influence of applied load, sliding velocity and martensitic transformation on the unlubricated sliding wear of austenitic stainless steels. *Wear*, *263*(1-6 SPEC. ISS.), 773–781. https://doi.org/10.1016/j.wear.2006.12.017
- Feng, J., Zhang, H., & He, P. (2009). The CMT short-circuiting metal transfer process and its use in thin aluminium sheets welding. *Materials and Design*, *30*(5), 1850–1852. https://doi.org/10.1016/j.matdes.2008.07.015
- Fu, P., Chu, R., Xu, Z., Ding, G., & Jiang, C. (2018). Relation of hardness with FWHM and residual stress of GCr15 steel after shot peening. *Applied Surface Science*, *431*, 165–169. https://doi.org/10.1016/j.apsusc.2017.09.136
- García-León, R. A., Martínez-Trinidad, J., Campos-Silva, I., Figueroa-López, U., & Guevara-Morales, A. (2021). Wear maps of borided AISI 316L steel under ball-on-flat dry sliding conditions. *Materials Letters*, *282*. https://doi.org/10.1016/j.matlet.2020.128842
- Godse, R. S., Gawande, S. H., & Keste, A. A. (2016). Tribological Behavior of High Fraction Carbon Steel Alloys. *Journal of Bio- and Tribo-Corrosion*, *2*(1). https://doi.org/10.1007/s40735-016-0034-3
- Gomes, J. H. F., Costa, S. C., Paiva, A. P., & Balestrassi, P. P. (2012). Mathematical modeling of weld bead geometry, quality, and productivity for stainless steel claddings deposited by FCAW.

Journal of Materials Engineering and Performance, *21*(9), 1862–1872. https://doi.org/10.1007/s11665-011-0103-1

- G.P., R., M, K., & Bakshi, S. R. (2019). Comparison of microstructure, dilution and wear behavior of Stellite 21 hardfacing on H13 steel using cold metal transfer and plasma transferred arc welding processes. *Surface and Coatings Technology*, *375*(June), 383–394. https://doi.org/10.1016/j.surfcoat.2019.07.019
- Gualco, A., Svoboda, H. G., Surian, E. S., & Vedia, L. A. de. (2010). Effect of welding procedure on wear behaviour of a modified martensitic tool steel hardfacing deposit. *Materials and Design*, *31*(9), 4165–4173. https://doi.org/10.1016/j.matdes.2010.04.026
- Gunaraj, V., & Murugan, N. (1999). Application of response surface methodology for predicting weld bead quality in submerged arc welding of pipes. *Journal of Materials Processing Technology*, *88*(1–3), 266–275. https://doi.org/10.1016/S0924-0136(98)00405-1
- Guo, C., Chen, J., Zhou, J., Zhao, J., Wang, L., Yu, Y., & Zhou, H. (2012). Effects of WC-Ni content on microstructure and wear resistance of laser cladding Ni-based alloys coating. *Surface and Coatings Technology*, *206*(8–9), 2064–2071. https://doi.org/10.1016/j.surfcoat.2011.06.005
- Gupta, D., & Sharma, A. K. (2014). Microwave cladding: A new approach in surface engineering. *Journal of Manufacturing Processes*, *16*(2), 176–182. https://doi.org/10.1016/j.jmapro.2014.01.001
- Gupta, M. K., Demirsöz, R., Korkmaz, M. E., & Ross, N. S. (2023). Wear and Friction Mechanism of Stainless Steel 420 Under Various Lubrication Conditions: A Tribological Assessment With Ball on Flat Test. *Journal of Tribology*, *145*(4). https://doi.org/10.1115/1.4056423
- Inoue, H., Koseki, T., Ohkita, S., & Fuji, M. (n.d.). Formation mechanism of vermicular and lacy ferrite in austenitic stainless steel weld metals.

- Jiang, J., & Arneu, R. D. (1998). On the running-in behaviour of diamond-like carbon coatings under the ball-on-disk contact geometry.
- Kannan, A. R., Shanmugam, N. S., Ramkumar, K. D., & Rajkumar, V. (2021). Studies on Super Duplex Stainless Steel Manufactured by Wire Arc Additive Manufacturing. *Transactions of the Indian Institute of Metals*, *74*(7), 1673–1681. https://doi.org/10.1007/s12666-021-02257-y
- Kannan, T., & Murugan, N. (2006). Effect of flux cored arc welding process parameters on duplex stainless steel clad quality. *journal of materials processing technology*, *176*(1–3), 230–239. https://doi.org/10.1016/j.jmatprotec.2006.03.157
- Kannan, T., & Yoganandh, J. (2010). Effect of process parameters on clad bead geometry and its shape relationships of stainless steel claddings deposited by GMAW. *International Journal of Advanced Manufacturing Technology*, *47*(9–12), 1083–1095. https://doi.org/10.1007/s00170-009-2226-1
- Kirchgaßner, M., Badisch, E., & Franek, F. (2008). Behaviour of iron-based hardfacing alloys under abrasion and impact. *Wear*, *265*(5–6), 772–779. https://doi.org/10.1016/j.wear.2008.01.004
- Koli, Y., Aravindan, S., & Rao, P. V. (2022). Influence of heat input on the evolution of δ-ferrite grain morphology of SS308L fabricated using WAAM-CMT. *Materials Characterization*, *194*. https://doi.org/10.1016/j.matchar.2022.112363
- Koli, Y., Aravindan, S., & Rao, P. V. (2023). Wear Characteristics of Wire-Arc Additive Manufactured SS308L. *Journal of Tribology*, *145*(3). https://doi.org/10.1115/1.4056191
- Koli, Y., Yuvaraj, N., Vipin, & Aravindan, S. (2019). Investigations on weld bead geometry and microstructure in CMT, MIG pulse synergic and MIG welding of AA6061-T6. *Materials Research Express*, *6*(12). https://doi.org/10.1088/2053-1591/ab61b6

- Kumar, M., Vaishya, R. O., Oza, A. D., & Suri, N. M. (2020). Experimental Investigation of Wire-Electrochemical Discharge Machining (WECDM) Performance Characteristics for Quartz Material. *Silicon*, *12*(9), 2211–2220. https://doi.org/10.1007/s12633-019-00309-z
- Kumar, S., & Shahi, A. S. (2011). Effect of heat input on the microstructure and mechanical properties of gas tungsten arc welded AISI 304 stainless steel joints. *Materials and Design*, *32*(6), 3617–3623. https://doi.org/10.1016/j.matdes.2011.02.017
- Kumar, V., & Singh, G. (2012). Effects of Process Parameters of Gas Metal Arc Welding on Dilution in Cladding of Stainless Steel on Mild Steel. 2(2), 127–131.
- LAKSHMINARAYANAN, A. K., & BALASUBRAMANIAN, V. (2009). Comparison of RSM with ANN in predicting tensile strength of friction stir welded AA7039 aluminium alloy joints. *Transactions of Nonferrous Metals Society of China (English Edition)*, *19*(1), 9–18. https://doi.org/10.1016/S1003-6326(08)60221-6
- Lee, J. W. (2005). The performance of a wear resistance cladding layer on a mild steel plate by electric resistance welding.
- Lee, J. W., Nishio, K., Katoh, M., Yamaguchi, T., & Mishima, K. (2005). The performance of a wear resistance cladding layer on a mild steel plate by electric resistance welding. *Welding in the World*, *49*(9–10), 94–101. https://doi.org/10.1007/BF03266493
- Lervåg, M., Sørensen, C., Robertstad, A., Brønstad, B. M., Nyhus, B., Eriksson, M., Aune, R., Ren, X., Akselsen, O. M., & Bunaziv, I. (2020). Additive manufacturing with superduplex stainless steel wire by cmt process. *Metals*, *10*(2). https://doi.org/10.3390/met10020272
- Liang, Y., Hu, S., Shen, J., Zhang, H., & Wang, P. (2017). Geometrical and microstructural characteristics of the TIG-CMT hybrid welding in 6061 aluminum alloy cladding. *Journal of Materials Processing Technology*, *239*, 18–30. https://doi.org/10.1016/j.jmatprotec.2016.08.005

- Lorenzin, G., & Rutili, G. (2009). The innovative use of low heat input in welding: Experiences on “cladding” and brazing using the CMT process. *Welding International*, *23*(8), 622–632. https://doi.org/10.1080/09507110802543252
- Lotfi, B., Rostami, M., & Sadeghian, Z. (2014). Effect of silicon content on microstructure of Al-Si/SiCp composite layer cladded on A380 Al alloy by TIG welding process. *Transactions of Nonferrous Metals Society of China (English Edition)*, *24*(9), 2824–2830. https://doi.org/10.1016/S1003-6326(14)63414-2
- Luchtenberg, P., de Campos, P. T., Soares, P., Laurindo, C. A. H., Maranho, O., & Torres, R. D. (2019). Effect of welding energy on the corrosion and tribological properties of duplex stainless steel weld overlay deposited by GMAW/CMT process. *Surface and Coatings Technology*, *375*, 688–693. https://doi.org/10.1016/j.surfcoat.2019.07.072
- Mendez, P. F., Barnes, N., Bell, K., Borle, S. D., Gajapathi, S. S., Guest, S. D., Izadi, H., Gol, A. K., & Wood, G. (2014). Welding processes for wear resistant overlays. *Journal of Manufacturing Processes*, *16*(1), 4–25. https://doi.org/10.1016/j.jmapro.2013.06.011
- Mishra, V., Yuvaraj, N., & Vipin, V. (2023). A comparative study on weld-bead geometry of austenitic stainless-steel produced by cold metal transfer welding and pulse metal inert gas welding process. *Proceedings of the Institution of Mechanical Engineers, Part E: Journal of Process Mechanical Engineering*. https://doi.org/10.1177/09544089231208549
- Montgomery, D. C. (n.d.). Design and analysis of experiments.
- Murugan, N., & Parmar, R. S. (1997). Stainless steel cladding deposited by automatic gas metal arc welding. *Welding Journal (Miami, Fla)*, *76*(12), 391-s.
- Mvola, B., Kah, P., Martikainen, J., & Suoranta, R. (2016). Dissimilar welded joints operating in sub-zero temperature environment. *International Journal of Advanced Manufacturing Technology*, *87*(9–12), 3619–3635. https://doi.org/10.1007/s00170-016-8711-4

- Nouri, M., Abdollah-Zadeh, A., & Malek, F. (2007). Effect of welding parameters on dilution and weld bead geometry in cladding. *Journal of Materials Science and Technology*, *23*(6), 817–822.
- Nuruzzaman, D. M., & Chowdhury, M. A. (2013). Friction Coefficient and Wear Rate of Different Materials Sliding Against Stainless Steel. *International Journal of Surface Engineering and Interdisciplinary Materials Science*, *1*(1), 33–45. https://doi.org/10.4018/ijseims.2013010103
- Ola, O. T., & Doern, F. E. (2014). A study of cold metal transfer clads in nickel-base INCONEL 718 superalloy. *Materials and Design*, *57*, 51–59. https://doi.org/10.1016/j.matdes.2013.12.060
- Om, H., & Pandey, S. (2013). Effect of heat input on dilution and heat affected zone in submerged arc welding process (Vol. 38).
- Oza, A. D., Kumar, A., & Badheka, V. (2020). Improving quartz micro-machining performance by magnetohydrodynamic and zinc-coated assisted traveling wire-electrochemical discharge machining process. *Materials Today: Proceedings*, *28*, 970–976. https://doi.org/10.1016/j.matpr.2019.12.334
- Oza, A. D., Kumar, A., Badheka, V., & Arora, A. (2019). Traveling Wire Electrochemical Discharge Machining (TW-ECDM) of Quartz Using Zinc Coated Brass Wire: Investigations on Material Removal Rate and Kerf Width Characteristics. *Silicon*, *11*(6), 2873–2884. https://doi.org/10.1007/s12633-019-0070-y
- Palani, P. K., & Murugan, N. (2006). Development of mathematical models for prediction of weld bead geometry in cladding by flux cored arc welding. *International Journal of Advanced Manufacturing Technology*, *30*(7–8), 669–676. https://doi.org/10.1007/s00170-005-0101-2
- Palani, P. K., & Murugan, N. (2007). Optimization of weld bead geometry for stainless steel claddings deposited by FCAW. *Journal of Materials Processing Technology*, *190*(1–3), 291–299. https://doi.org/10.1016/j.jmatprotec.2007.02.035

- Pant, P., Chatterjee, D., Nandi, T., Samanta, S. K., Lohar, A. K., & Changdar, A. (2019). Statistical modelling and optimization of clad characteristics in laser metal deposition of austenitic stainless steel. *Journal of the Brazilian Society of Mechanical Sciences and Engineering*, *41*(7). https://doi.org/10.1007/s40430-019-1784-x
- Pereira, J., Zambrano, J., Licausi, M., Tobar, M., & Amigó, V. (2015). Tribology and high temperature friction wear behavior of MCrAlY laser cladding coatings on stainless steel. *Wear*, *330–331*, 280–287. https://doi.org/10.1016/j.wear.2015.01.048
- Peruzzo, M., Serafini, F. L., Ordoñez, M. F. C., Souza, R. M., & Farias, M. C. M. (2019). Reciprocating sliding wear of the sintered 316L stainless steel with boron additions. *Wear*, *422–423*, 108–118. https://doi.org/10.1016/j.wear.2019.01.027
- Physical Principles of Electron Microscopy. (2005).
- Pickin, C. G., Williams, S. W., & Lunt, M. (2011). Characterisation of the cold metal transfer (CMT) process and its application for low dilution cladding. *Journal of Materials Processing Technology*, *211*(3), 496–502. https://doi.org/10.1016/j.jmatprotec.2010.11.005
- Rajeev, G. P., Kamaraj, M., & Bakshi, S. R. (2014). Al-Si-Mn alloy coating on aluminum substrate using cold metal transfer (CMT) welding technique. *Jom*, *66*(6), 1061–1067. https://doi.org/10.1007/s11837-014-0970-7
- Rajeev, V. R., Dwivedi, D. K., & Jain, S. C. (2010). Dry reciprocating wear of Al-Si-SiCp composites: A statistical analysis. *Tribology International*, *43*(8), 1532–1541. https://doi.org/10.1016/j.triboint.2010.02.014
- Rajkumar, V., Arjunan, T. V., & Rajesh Kannan, A. (2020). Investigations on hard-facing and wear characteristics of nickel-based Inconel 625 overlaid welds over AISI 347 pipe. *Journal of the Brazilian Society of Mechanical Sciences and Engineering*, *42*(1). https://doi.org/10.1007/s40430-019-2092-1

- Roy, J. G., Yuvaraj, N., & Vipin. (2021). Effect of Welding Parameters on Mechanical Properties of Cold Metal Transfer Welded Thin AISI 304 Stainless-Steel Sheets. *Transactions of the Indian Institute of Metals*, *74*(9), 2397–2408. https://doi.org/10.1007/s12666-021-02326-2
- Saha, M. K., Hazra, R., Mondal, A., & Das, S. (2019). Effect of Heat Input on Geometry of Austenitic Stainless Steel Weld Bead on Low Carbon Steel. *Journal of The Institution of Engineers (India): Series C*, *100*(4), 607–615. https://doi.org/10.1007/s40032-018-0461-7
- Samandi, M., Shedden, B. A., Smith, D. I., Collins, G. A., Hutchings, R., & Tendys, J. (1993). Microstructure, corrosion and tribological behaviour of plasma immersion ion-implanted austenitic stainless steel. In *Surface and Coatings Technology* (Vol. 59).
- Sathirachinda, N., Pettersson, R., & Pan, J. (2009). Depletion effects at phase boundaries in 2205 duplex stainless steel characterized with SKPFM and TEM/EDS. *Corrosion Science*, *51*(8), 1850–1860. https://doi.org/10.1016/J.CORSCI.2009.05.012
- Selçuk, B., Karamiş, M. B., Selçuk, B., Ipek, R., & Karamışçkaramısç, M. B. (2001). Study of friction and wear of carburized, carbonitrided, and borided steels AISI1020 and AISI5115 A study on friction and wear behaviour of carburized, carbonitrided and borided AISI 1020 and 5115 steels. https://www.researchgate.net/publication/293563946
- Senthilkumar, B., & Kannan, T. (2015a). Effect of flux cored arc welding process parameters on bead geometry in super duplex stainless steel claddings. *Measurement: Journal of the International Measurement Confederation*, *62*, 127–136. https://doi.org/10.1016/j.measurement.2014.11.007
- Senthilkumar, B., & Kannan, T. (2015b). Effect of flux cored arc welding process parameters on bead geometry in super duplex stainless steel claddings. *Measurement: Journal of the International Measurement Confederation*, *62*, 127–136. https://doi.org/10.1016/j.measurement.2014.11.007

- Shahi, A. S., & Pandey, S. (2008a). Modelling of the effects of welding conditions on dilution of stainless steel claddings produced by gas metal arc welding procedures. *Journal of Materials Processing Technology*, *196*(1–3), 339–344. https://doi.org/10.1016/j.jmatprotec.2007.05.060
- Shahi, A. S., & Pandey, S. (2008b). Modelling of the effects of welding conditions on dilution of stainless-steel claddings produced by gas metal arc welding procedures. *Journal of Materials Processing Technology*, *196*(1–3), 339–344. https://doi.org/10.1016/j.jmatprotec.2007.05.060
- Shayanfar, P., Daneshmanesh, H., & Janghorban, K. (2020). Parameters Optimization for Laser Cladding of Inconel 625 on ASTM A592 Steel. *Journal of Materials Research and Technology*, *9*(4), 8258–8265. https://doi.org/10.1016/J.JMRT.2020.05.094
- Singh, J., Thakur, L., & Angra, S. (2020). An investigation on the parameter optimization and abrasive wear behaviour of nanostructured WC-10Co-4Cr TIG weld cladding. *Surface and Coatings Technology*, *386*, 125474. https://doi.org/10.1016/J.SURFCOAT.2020.125474
- Smith, A. F. (1986). THE FRICTION AND SLIDING WEAR OF UNLUBRICATED 316 STAINLESS STEEL IN AIR AT ROOM'TEMPERATURE IN THE LOAD RANGE 0.5-90 N. In *Wear* (Vol. 110).
- Solecka, M., Kopia, A., Radziszewska, A., & Rutkowski, B. (2018). Microstructure, microsegregation and nanohardness of CMT clad layers of Ni-base alloy on 16Mo3 steel. *Journal of Alloys and Compounds*, *751*(April), 86–95. https://doi.org/10.1016/j.jallcom.2018.04.102
- Song, R. B., Xiang, J. Y., & Hou, D. P. (2011). Characteristics of mechanical properties and microstructure for 316L austenitic stainless steel. *Journal of Iron and Steel Research International*, *18*(11), 53–59. https://doi.org/10.1016/S1006-706X(11)60117-9
- Sreeraj, P., & Kannan, T. (2012). Modelling and prediction of stainless steel clad bead geometry deposited by GMAW using regression and artificial neural network models. *Advances in Mechanical Engineering*, *2012*. https://doi.org/10.1155/2012/237379

- Stott, F. H. (1998). The role of oxidation in the wear of alloys. In *Tribology* (Vol. 31).
- Sun, H. Q., Shi, Y. N., & Zhang, M. X. (2008). Wear behaviour of AZ91D magnesium alloy with a nanocrystalline surface layer. *Surface and Coatings Technology*, *202*(13), 2859–2864. https://doi.org/10.1016/j.surfcoat.2007.10.025
- Sun, Z., Lv, Y., Xu, B., Liu, Y., Lin, J., & Wang, K. (2015). Investigation of droplet transfer behaviours in cold metal transfer (CMT) process on welding Ti-6Al-4V alloy. *International Journal of Advanced Manufacturing Technology*, *80*(9–12), 2007–2014. https://doi.org/10.1007/s00170-015-7197-9
- Tan, H., Jiang, Y., Deng, B., Sun, T., Xu, J., & Li, J. (2009). Effect of annealing temperature on the pitting corrosion resistance of super duplex stainless steel UNS S32750. *Materials Characterization*, *60*(9), 1049–1054. https://doi.org/10.1016/J.MATCHAR.2009.04.009
- Ul-Hamid, A., Tawancy, H. M., & Abbas, N. M. (2005). Failure of weld joints between carbon steel pipe and 304 stainless steel elbows. *Engineering Failure Analysis*, *12*(2), 181–191. https://doi.org/10.1016/j.engfailanal.2004.07.003
- Varghese, P., Vetrivendan, E., Dash, M. K., Ningshen, S., Kamaraj, M., & Kamachi Mudali, U. (2019). Weld overlay coating of Inconel 617 M on type 316 L stainless steel by cold metal transfer process. *Surface and Coatings Technology*, *357*, 1004–1013. https://doi.org/10.1016/j.surfcoat.2018.10.073
- Wang, Y., Yue, W., Kang, J., Zhu, L., Fu, Z., & Wang, C. (2019). Effect of Surface Nanocrystallization Pretreatment on the Tribological Properties of Plasma Nitrided AISI 316 L Stainless Steel under Boundary Lubrication. *Journal of Tribology*, *141*(4). https://doi.org/10.1115/1.4042392

- Wang, Z., Xu, J., Shoji, T., Takeda, Y., Yuya, H., & Ooyama, M. (2018). Microstructure and pitting behavior of the dissimilar metal weld of 309L cladding and low alloy steel A533B. *Journal of Nuclear Materials*, *508*, 1–11. https://doi.org/10.1016/j.jnucmat.2018.05.011
- Xie, F., He, X., Cao, S., & Qu, X. (2013). Structural and mechanical characteristics of porous 316L stainless steel fabricated by indirect selective laser sintering. *Journal of Materials Processing Technology*, *213*(6), 838–843. https://doi.org/10.1016/j.jmatprotec.2012.12.014
- Zhou, J., Ma, K., Li, C. X., Yasir, M., Luo, X. T., & Li, C. J. (2020). Microstructures of aluminum surfaces reinforced with 316L stainless steel particles via high-speed particle injection and the resulting double-strengthening mechanism. *Surface and Coatings Technology*, *385*. https://doi.org/10.1016/j.surfcoat.2020.125380
- Zhu, M., He, F., Yuan, Y. F., Yin, S. M., Guo, S. Y., & Pan, J. (2021). Effect of Aging Timeon the Microstructure and Corrosion Behavior of 2507 Super Duplex Stainless Steel in Simulated Marine Environment. *Journal of Materials Engineering and Performance*, *30*(8), 5652–5666. https://doi.org/10.1007/s11665-021-05812-2

LIST OF PUBLICATIONS

- **List of papers published in SCI/SCIE journals**

- **Mishra V,** Yuvaraj N, Vipin. Tribological Behavior of Austenitic Stainless Steel-Clad Surface Over Low Carbon Steel Produced by Cold Metal Transfer Welding Process. Transactions of the Indian Institute of Metals. 2024:1-2. **(Impact factor: 1.391).**
- **Mishra V,** Yuvaraj N, Vipin V. A comparative study on weld-bead geometry of austenitic stainless-steel produced by cold metal transfer welding and pulse metal inert gas welding process. Proceedings of the Institution of Mechanical Engineers, Part E: Journal of Process Mechanical Engineering. 2023,25:09544089231208549. **(Impact factor: 2.4).**
- **Mishra V,** Yuvaraj N, Vipin V. A study on performance of super duplex stainless-steel cladding over mild steel using a CMT welding, Journal of Adhesion Science and Technology. (**Impact factor: 2.7).**

- **List of papers published in International Conferences**

- V. Mishra, N. Yuvraj, Vipin "Effect of welding speed on cladding of mild steel plate using CMT process". AMPT international conference 2023 held at NIT Jamshedpur.
- V. Mishra, N. Yuvraj, Vipin "Cladding of mild steel plate using CMT process". ICMech REC 2023 international conference held at NIT Warangal, Telangana.
- V. Mishra, N. Yuvraj, Vipin "Cladding of mild steel plate using CMT process-A Review". ICARI international conference held at MIET Meerut.

CURRICULUM VITAE

Mrs. Varsha Mishra has obtained her Bachelor's degree (B.Tech) in Mechanical engineering (2009-2013) from BBDNIIT, Lucknow and Master's Degree (M.Tech) in Manufacturing Technology (2015-2019) From NITTTR Chandigarh, India. Her main area of research includes Gas Metal Arc Welding (GMAW), Cold Metal Transfer Welding (CMT), Cladding and optimization techniques. She has published 3 SCI/SCIE and 3 conference papers at an international level.